

Mobile spectroscopic measurements of atmospheric carbon dioxide and methane

Zur Erlangung des akademischen Grades eines
DOKTORS DER NATURWISSENSCHAFTEN
von der Fakultät für Physik des
Karlsruher Instituts für Technologie (KIT)

genehmigte

DISSERTATION

von

Dipl. Phys. Friedrich Wilhelm Klappenbach
geboren am 09.05.1983
in Potsdam

Tag der mündlichen Prüfung:

15.07.2016

Referent:

Prof. Dr. Johannes Orphal

Korreferent:

Priv.-Doz.Dr.Michael Höpfner

Zusammenfassung

Atmosphärisches Kohlenstoffdioxid und Methan sind die wichtigsten anthropogenen Treibhausgase. Die Quellen und Senken dieser Gase lassen sich durch hochgenaue und repräsentative Messungen mithilfe des sogenannten „Top Down“ Ansatzes bestimmen. Bodengestützte, fernerkundliche Messungen in solarer Direktlicht-Spektroskopie nutzen molekulare Rotations-Vibrations-Absorptionsbanden im nahen Infrarot um die Spurengaskonzentration entlang des Lichtweges durch die Atmosphäre zu bestimmen. Derzeit gibt es Netzwerke einigen dutzend Stationen, die weltweit regelmäßige, bodengebundene, fernerkundliche Messungen von CO₂ und CH₄ durchführen. Durch diese geringe Anzahl ist die Bestimmung von Quellen und Senken dieser Gase jedoch mit erheblichen Unsicherheiten behaftet. Ziel dieser Arbeit ist es, die globale Abdeckung von bodengebundenen, fernerkundlichen Messungen der Klimagase CO₂ und CH₄ durch mobile und portable Spektrometer zu erweitern, sodass kampagnengebundene Messungen möglich werden.

Direktlicht-Spektroskopie erfordert hochgenaues Einkoppeln der solaren Intensität in die Eintrittsblende des Spektrometers. Dies stellt eine Herausforderung für mobile Anwendungen z.B. auf einem Schiff dar. Ein Sonnenfolger, der für den stationären Betrieb konzipiert war, wurde für bewegte Plattformen so erweitert, dass die benötigte Genauigkeit von 0.05° für Winkelgeschwindigkeiten von bis zu 6.3 °s⁻² gewährleistet werden kann. Während einer Messkampagne konnte dieser Sonnenfolger erfolgreich auf einem Schiff getestet werden.

Im Rahmen dieser Arbeit wurden zwei Spektrometer mit einem Auflösungsvermögen von mindestens 12.000 für die spektralen Absorptionsbanden von CO₂ (≈ 1600 nm), CH₄ (≈ 1650 nm) und O₂ (≈ 1260 nm, als Referenz) getestet. Eines der Instrumente ist eine Gitterbasierte Eigenentwicklung. In Voruntersuchungen wurde unter anderem ein sogenanntes „Immersionsgitter“ aus monokristallinem Silizium getestet. Trotz der sehr guten spektralen Eigenschaften, wurde ein Kampagnen-Instrument mit einem konventionellem Gitter implementiert. Ein Teil der Arbeit umfasst die Charakterisierung des 2D-InGaAs-Detektors, welcher Nicht-Linearitäten und unerwünschte Interferenzmuster zeigte. Das implementierte Instrument hat ein Auflösungsvermögen von 29.000 und kann die atmosphärische CO₂-Konzentration mit einer Präzision von etwa 0.4% messen.

Das zweite getestete Instrument ist das EM27/SUN Fourier-Transform-Spektrometer. Es wurde in Zusammenarbeit mit Bruker Optics und dem KIT entwickelt und konnte bereits hervorragende Eignung im stationären Betrieb unter Beweis stellen. Diese Arbeit konnte zeigen, dass auch im schiff-gestützten Betrieb während einer Fahrt von Kapstadt nach Bremerhaven eine hoch genaue Messung mit einer Präzision von 0.03% bei XCO₂ und 0.04% bei XCH₄ mit diesem Instrument möglich ist (Klappenbach et al., 2015). Dieser

veröffentlichte Nord-Süd-Transekt reproduziert den inter-hemisphärischen Gradienten der Konzentrationen beider Spurengase, mit erhöhten Messwerten in der nördlichen Hemisphäre. Nach Kalibration ist die Messung akkurat genug um Satelliten Daten zu validieren und ermöglicht es in einer Folgestudie Modelldefizite eines Vorhersagemodells für atmosphärisches CO₂ und CH₄ zu quantifizieren.

Abstract

Carbon dioxide and methane are the most important anthropogenic greenhouse gases. The sources and sinks of these gases can be inferred with the “top-down” approach from accurate and representative measurements. Ground based remote sensing uses rotational-vibrational absorption features in the Near-Infra-Red (NIR) spectral region, to retrieve the trace gas concentration along the solar light path through the atmosphere. However, only a few tens of sites worldwide deliver ground based remote sensing measurements of CO₂ and CH₄ on a regular basis which hinders a robust evaluation of sources and sinks of these two greenhouse gases. This approach is not flexible enough to conduct campaign based measurements.

This work aims at increasing the spatial representation of ground based remote sensing measurements with robust and portable packing-case sized instruments. Direct sunlight spectroscopy on a mobile platform, such as a ship, requires an accurate solar tracking device that couples solar intensity into the spectrometer’s entrance aperture regardless the instrument’s orientation. This work documents the development of the tracker and reveals in a performance analysis a tracking accuracy of 0.05 ° up to angular accelerations of 6.3 °s⁻² which suits excellent for deployment on a ship.

Two spectrometers with a resolving power of at least 12,000 within the spectral region of CO₂ (≈ 1600 nm), CH₄ (≈ 1650 nm) and O₂ (≈ 1260 nm, as reference) were tested for ship based measurements. One of the instruments is a self-developed grating spectrometer. Initial tests investigate a setup with an “immersed grating”, made of crystalline silicon. Despite the excellent properties, a conventional grating setup was finally implemented in the campaign instrument. In addition extensive detector-characterization of the used 2D InGaAs detector with respect to non-linearity as well as etalon-interference is part of this work. The finally implemented grating spectrometer has a resolving power of approximately 29,000 and can measure CO₂ concentrations with 0.4 % precision.

The second instrument used within this work is the IR-Fourier-Transform-Spectrometer EM27/SUN previously developed in cooperation with Bruker Optics and KIT. The instrument showed excellent results even under campaign conditions. The atmospheric concentrations during a ship based campaign from Cape Town to Bremerhaven were measured with precisions better than 0.03 % for XCO₂ and 0.04 % for XCH₄, respectively (Klappenbach et al., 2015). This work demonstrates that the instrument is accurate enough to validate satellite data, proper coincidence given. The measured inter-hemispheric gradient of both gases was used in a follow up study, to investigate model-deficiencies in forecasting global concentrations of CO₂ and CH₄.

Contents

Zusammenfassung	i
Abstract	iii
Introduction	1
1 Measurement techniques for atmospheric CO₂ and CH₄	5
1.1 In-situ methods	6
1.2 Remote sensing	7
1.2.1 Molecular absorption	7
1.2.2 Satellite remote sensing	12
1.2.3 Ground based remote sensing	15
2 Solar tracking device	17
2.1 Setup of the solar tracker	17
2.2 Performance of solar tracking device	21
3 The miniature Fourier Transform spectrometer EM27 / SUN	27
3.1 Fourier transform spectrometry	27
3.2 Optical setup of the EM27	30
3.3 DC-fluctuations	32
3.4 Quality filters	34
3.5 Spectral calibration - CALPY-mobile	35
4 Grating spectrometer for mobile applications	39
4.1 Optical setup of grating spectrometers	40
4.2 Diffracting elements	40
4.3 Design concepts for a NIR-grating spectrometer	42
4.3.1 Immersed grating concept	44
4.3.2 Inter-comparison of three grating setups	46
4.4 Ground based grating NIR spectrometer	49
4.5 Data acquisition and processing	55
4.5.1 Data acquisition	55
4.5.2 Data processing	58
4.6 Photonic detectors	59

4.6.1	Detector dark current	60
4.6.2	Detector non linearity	61
4.6.3	Etaloning - unwanted interference patterns	65
4.7	Spectral calibration and up sampling	72
4.8	Instrumental line shape (ILS)	74
4.9	Performance and future improvements of the GRC	79
5	Retrieval - from spectrum to total column	83
5.1	Retrieval theory	83
5.2	Instrumental Line Shape - ILS	85
5.3	Trace gas retrievals from the EM27 and GRC	87
5.4	Post processing	90
5.4.1	Referencing to the oxygen total column	91
5.4.2	Dependency on solar zenith angle	91
5.4.3	Detection of ships exhaust plume	95
5.4.4	Calibration to WMO reference	99
6	Interhemispheric transect of carbon dioxide and methane	103
6.1	Campaign description	103
6.2	XCO ₂ and XCH ₄ - inter hemispheric transect	105
6.3	Hemispheric source strength - use of a simple box model	111
6.4	Model improvements with the measured north-south transect.	112
6.5	FTS versus Grating Spectrometer	113
7	Conclusion and outlook	115
	Acknowledgment	117
8	Bibliography	119

Introduction

Carbon dioxide (CO₂) and methane (CH₄) are the most important anthropogenic greenhouse gases (Stocker et al., 2013, Figure SPM.5). Since pre-industrial times 1750AD the atmospheric concentration of CO₂ rose by approximately 40% from 280 ppm (parts per million) to approximately 400 ppm (Le Quéré et al., 2013). An even stronger relative rise shows atmospheric CH₄ with an increase of approximately 150% from 720 ppb (parts per billion) to 1800 ppb within the same timespan (Dlugokencky et al., 2016). This increase is the main driver for the anthropogenic greenhouse effect and the increase in global mean temperatures of approximately 1 °C (Hansen et al., 2010).

The scientific understanding of the connection from increased greenhouse gases (GHGs) to increased temperatures is considered very high (Stocker et al., 2013, Figure SPM.5). The atmospheric burden of GHGs is influenced by both anthropogenic and natural sources and sinks such as fossil fuel combustion, landfills, wetlands, photosynthesis, oceanic surfaces and many others (e.g. Schulze, 2006; Le Quéré et al., 2013; Stocker et al., 2013). However, the scientific understanding of these individual source and sink contributions on a continental or regional scale is rather low and subject to large uncertainties (e.g. Stocker et al., 2013, Figure 6.15, Table 6.3, Table 6.6). In order to predict future climate a good scientific understanding of these sources and sinks is indispensable. Not only the underlying mechanisms and drivers that control these sources and sinks, but also the absolute amount of emitted compounds on a continental scale play a key role.

In general two approaches aim to increase the scientific knowledge upon sources and sinks of GHGs. The “bottom up” approach characterizes individual source and sink contributors such as plants, eco-regions or individual animals. Upscaling of these individual contributions is the second step to infer the global budget of GHG emissions (e.g. Schulze, 1986; Dentener et al., 2005; Denman et al., 2007; Hodson et al., 2011). This approach is complemented by the “top down” approach. The presence of a source or sink alters the GHG-concentration of an air-parcel. Measurements of GHGs allow to infer the source or sink strength from gradients in the trace gas concentration. Here, global models with underlying advection schemes interconnect individual measurements to obtain the source strength along the interconnecting trajectory (e.g. Schimel et al., 2001; Baker, 2001; Takahashi et al., 2009; Allen et al., 2012; Peylin et al., 2013).

This work contributes to the “top down” approach. This approach is challenged by the globally sparse and inhomogeneous distribution of measurements (e.g. Masarie et al., 2011; Babenhauserheide et al., 2015). Additionally an individual measurement can contribute with various weights into the model output. This weight is dominated by both the

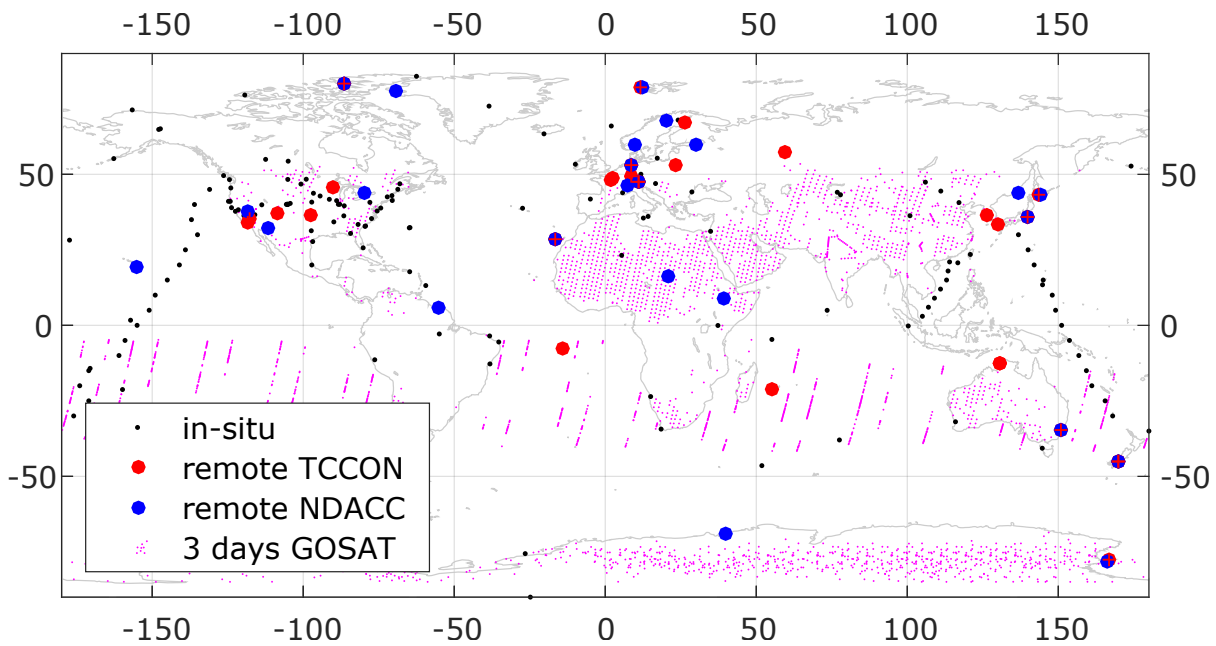


Figure 0.1: Global view of greenhouse gas measurements (mainly CO_2 and CH_4) by several networks. In-situ measurements are highly accurate point-like measurements (small black dots). Ground based remote sensing measurements on a regular basis are organized in two networks (NDACC and TCCON) measure total column average concentration and represent basically the entire atmosphere overhead. With a good global coverage but low accuracy satellite soundings can complement this global picture. Shown are valid soundings of GOSAT measurements within 3 days provided by ACOS. The 3 day time span corresponds to the revisit-time for the satellite to a specific geo-location. Data by (Masarie et al., 2014) (in-situ) (TCCON-Wiki, 2015) (TCCON), (Hannigan, 2011) (NDACC) and (O’Dell et al., 2012) (GOSAT)

accuracy of the measurement as well as on the representativeness of the measurement. This representativeness can be increased by probing multiple parts of the atmosphere rather than a point-like measurement. Remote sensing, in terms of spectroscopy, allows to retrieve a representative cross-section of GHG-concentrations through the atmosphere known as “total column average”. This total column average can be inferred from space based satellite soundings with high global coverage, but low accuracy (Yokota et al., 2004; Butz et al., 2011; Schepers et al., 2012, e.g.). Ground based total column measurements validate coinciding satellite soundings as well as serving as a highly accurate and representative measurement (e.g. Wunch et al., 2010; Feist et al., 2010; Messerschmidt et al., 2011). Table 0.1 presents an overview on the most important CO_2 and CH_4 products.

However, globally there are well below fifty sites, that conduct ground based total column measurements of GHGs on a regular basis. These accurate and representative measurements are still too sparse to infer individual source and sink contributions of GHGs on a continental scale (e.g. McGuire et al., 2012; Gloor et al., 2012; Babenhauserheide et al., 2015). These ground based measurement sites require frequent maintenance and laboratory infrastructure, which does not allow conducting campaign based measurements to increase the sparse sampling.

	CO ₂ %	CH ₄ %	worldwide number	citation
ObsPack (in-situ)	0.025	0.2	≈ 160	(WMO-GAW, 2011)
TCCON (remote)	0.2	0.4	29	(Wunch et al., 2011)
Satellite (remote)	0.5-2	0.5 - 2	≈ 1000 per day	(Schneising et al., 2008)

Table 0.1: Typical accuracies for several greenhouse gas measurement techniques. Referenced to an atmospheric background concentration of 390 ppm CO₂ and 1.7 ppm CH₄.

This work aims to perform highly accurate ground based remote sensing measurements of GHGs with near infrared spectroscopy with a robust instrument, which can be operated campaign based on a mobile platform such as a ship. The approach allows to complement the lack of spatially accurate and representative measurements of greenhouse gases. It can contribute to both satellite validation as well as model improvements. In addition the agility allows to characterize local sources such as volcanic or anthropogenic emissions and can contribute to an enhanced scientific understanding on the sources and sinks of greenhouse gases.

This work is structured as follows. chapter 1 introduces the most important measurement techniques for atmospheric greenhouse gases. After a short introduction on in-situ approaches, the principles of remote sensing will be given starting out with insights into molecular absorption theory. Technical details and principles of satellite remote sensing as well as ground based remote sensing will close this general introduction.

The structure of the following chapters orientates on the processing steps in the chain from initial instrument design considerations to the finally evaluated total column average. Here, each chapter starts with an introduction that presents the theoretical basics. This introduction is followed by technical details found to be important within this work. The chapter closes with an evaluation and discussion of the findings.

The processing chain stars at the solar tracking device in chapter 2. Focus is put upon the challenge for mobile applications to feed the solar intensity into the spectrometers entrance and how to compensate for movements of the platform in real time.

Two infra-red (IR) spectrometers had been used within this work. The IR-Fourier-Transform Spectrometer “EM27/SUN” will be presented in chapter 3. The underlying theoretical basics on Fourier Transform Spectrometry and the optical setup are presented in the first two sections. As part of this work corrections such as DC-correction and additional a post processing quality-filters will be presented. The section closes with a short overview on the implemented Python¹ software “CALPY-mobile”.

The second IR-spectrometer is a self-developed grating spectrometer “Ground based RemoTeC” (GRC) as an alternative approach. chapter 4 starts out with a general introduction on theoretical background. Within this work three optical setups of such a grating instrument had been tested in a breadboard setup. Besides two approaches with conventional gratings the third tested instrument is based on an “immersed grating” with

¹<https://www.python.org/>, last access Jun 12,2016

significantly enhanced dispersion, developed for space based instruments. Despite convincing properties, one of the conventional grating instruments was chosen to be implemented in a campaign instrument. The technical details of this instrument starting at section 4.4. Since the data-acquisition and processing differs from the FTS instrument, the acquisition and processing scheme will be presented before further details on the used two dimensional detector will follow. This two-dimensional detector array poses the key feature of this instrument development and allows to increase both sampling and signal to noise ratio of the final spectrum. In section 4.6 the shortcomings of the detector, mainly non-linearity and etalon-interference will be presented and how to correct for these effects. The section closes with a laser-based characterization of the instrumental line shape as a measure of the spectral quality. The instrumental quality with respect to trace gas measurements will be discussed in the upcoming chapter. The section closes with the discussion how the instrument can be further improved.

Chapter 5 gives insights on the spectral retrieval and how the total column can be obtained from the spectral record. After an introduction on retrieval theory the impact of the instrumental line shape will be discussed in more detail as a key retrieval contribution. The retrievals of a consecutive day will be presented for both the IR-FTS as well as the grating instrument GRC.

Since all the basics are presented in the previous chapters, the final chapter 6 can focus on the campaign description of a ship-based campaign from South Africa to Germany whilst recording the inter hemispheric transect of the greenhouse gases carbon dioxide and methane in direct sunlight spectroscopy. Besides satellite validation this highly accurate data set can be used to characterize model-weaknesses along the inter-hemispheric gradient of carbon dioxide and methane. A final comparison of grating and FTS instrument closes this work.

1 Measurement techniques for atmospheric CO₂ and CH₄

In monitoring the atmospheric concentrations of CO₂ and CH₄ several global networks provide data-sets with various temporal and spatial resolutions. Here a short overview of the most important networks will be given. These networks can be divided into in-situ networks that sample a punctual section of the atmosphere, and remote sensing networks that typically measure an atmospheric cross-section overhead.

Besides sporadic campaign based measurements (e.g. Wofsy, 2011; Machida et al., 2008; Feist et al., 2010; Frey et al., 2015; Hase et al., 2015) networks conduct long term measurements. One of them is the observation package (ObsPack), organized by the Earth System Research Laboratory (ESRL) which acts as a distribution platform of relevant data for carbon cycle modeling (Masarie et al., 2014). Further data sets are available from passenger aircraft flights that are conducted 8-12 times a year (Schuck et al., 2009; Brenninkmeijer et al., 2007). Finally, the Total Carbon Column Observatory Network (TCCON¹) is a network of currently 28 WMO²-validated remote sensing sites that operate IR-FTS instruments in direct sunlight spectroscopy (Wunch et al., 2011). In addition the NDACC (Network for the Detection of Atmospheric Composition Change) with the IRWG (Infra-Red Working Group) for sensing atmospheric trace gases in the Mid Infra-Red (MIR) operates currently 24 sites. Note that some of the sites are both, NDACC and TCCON sites. The last two ground based remote sensing networks are complemented by data from the recently initiated and growing Collaborative Carbon Column Observing Network (COCCON) (Hase et al., 2014, 2015), that uses smaller, more agile instruments in direct sunlight spectroscopy which is also used within this work.

These ground based or aircraft supported measurements are complemented by satellite remote sensing approaches from space. Current remote sensing satellites are passive instruments such as Thermal Infra-Red (TIR) sounders like IASI³ (Phulpin et al., 2007; Blumstein et al., 2007). Currently operating SWIR⁴-sounders are the TANSO-FTS-instrument on board the Greenhouse Gas Observing Satellite (GOSAT) (Yokota et al., 2004; Kobayashi et al., 2010) and the OCO-2 (Orbiting Carbon Observatory 2) that focuses on CO₂ (Crisp

¹Website: <https://tccon-wiki.caltech.edu/> (last access May 31,2016)

²World Meteorological Organization

³Infrared Atmospheric Sounding Interferometer, European Organization for the Exploration of Meteorological Satellites (EUMETSAT) operated by European Space Agency (ESA)

⁴Short Wave Infra-Red approximately 1.4-3 μm

et al., 2004). Active instruments using light detecting and ranging (LIDAR) as for example MERLIN⁵ are scheduled to be launched in December 2019 (Stephan et al., 2011).

Table 0.1 reflects typical accuracies of in-situ, ground based and satellite remote approaches. The accuracy for in-situ instruments is derived from the WMO comparison requirement. Two instruments are comparable, if they measure the same state within a 0.1 ppm margin in the northern hemisphere and 0.05 ppm in the southern hemisphere. For methane measurements, two instruments are allowed to deviate not more than 2 ppb from each other (WMO-GAW, 2011). Wunch et al. (2010, Table 5) presents the TCCON accuracy derived from in-situ aircraft profiles. The estimate of the accuracy of satellite soundings is a challenging task and typically limited to the availability of independent reference measurements. The accuracy also differs among individual satellite missions. This results into a larger spread in accuracy quantification of satellite remote sensing.(e.g Butz et al., 2011; Schneising et al., 2008).

1.1 In-situ methods

The in-situ technique can be performed as continuous measurements (e.g. van der Laan et al., 2009; Flowers et al., 2012) that sample local air source through an inlet and analyze it in-situ. The high chemical stability of CO₂ and CH₄ allows for an alternate approach as well. Air samples can be collected in flasks and analyzed in the lab later on with a great variety of available methods. Instruments used for in-situ measurements are gas-chromatographic approaches (e.g. Turnbull et al., 2012), laser cavity ring down (e.g. Crosson, 2008) or mass-spectroscopic and chemical approaches. Network structures such as Observation Package (ObsPack) (Masarie et al., 2014; Zhao and Tans, 2006) or The World Data Centre for Greenhouse Gases (WDCGG)⁶ provide standardized data access. These point-like measurement samples can be advanced by mobile platforms such as aircraft (e.g. Wofsy, 2011; Brenninkmeijer et al., 2007) or balloon soundings (e.g. Karion et al., 2010) to vertical atmospheric profiles. In-situ approaches typically come along with a high precision. Calibration with a reference gas and yields then into a high accuracy (Masarie et al., 2001).

However limitations of in-situ records are the lack of data in remote regions such as tropical or Eurasian mid-latitude regions since lab-infrastructure has to be present at the measurement site as Figure 0.1 depicts. Despite the quite large number of global sites, Law et al. (2008) could show, that it is still insufficient to infer the source strength of specific regions (here, southern oceanic sink). She could show, that the variation in source-strength in 1981-2002 strongly depends on the choice of network and cannot considered to be significant in this particular case.

⁵Methane Remote Lidar Mission by DLR (Deutsches Zentrum für Luft- und Raumfahrt) and CNES (Centre National d'Etudes Spatiales)

⁶<http://ds.data.jma.go.jp/gmd/wdcgg/introduction.html>, (last access May,24 2016)

In addition the localized sampling method of in-situ approaches might deviate significantly from the mean averaged signal of a larger region such as a model grid in the order of a few ten to hundred kilometers.

1.2 Remote sensing

Contrary to in-situ methods, remote sensing approaches allow to obtain the trace gas concentrations from a distance. The key idea here is to make use of absorption or emission features of individual trace gases. This approach is widely used in astronomy to obtain the information on the composition of extraterrestrial atmospheres stars or nebulae. But also the earth can be observed from space via satellite remote sensing. In addition, ground based remote sensing can be conducted from the earth's surface and measures the average trace gas concentration of the atmosphere overhead. In the following section the basic concepts of remote sensing techniques will be presented, starting out with the basics of molecular absorption. In a next step satellite remote applications will be elaborated followed by the description of ground based remote sensing approaches.

1.2.1 Molecular absorption

In the following subsection, the molecular interaction with electro-magnetic (EM) waves (such as infra-red radiation) will be described. Electronic transitions with higher energies are not predominant in the IR-region but become more relevant in the UV-VIS spectral region. The section focuses on sketching, how the spectral position and intensities of spectral absorption or emission of IR spectral absorbing gases can be explained and why each molecule has a very characteristic and molecule specific interaction with EM-waves. Despite conceptually most of the content applies for other molecules as well, main focus lies on the CO₂ molecule in order to decrease the complexity of the topic. More details can be found in Petty (2007); Atkins and De Paula (2013); Demtröder (2010).

A molecule, as a bonded state of two or more atoms, can be in different quantum mechanical states that correspond to different energy levels. The CO₂ molecule consists of three atoms O=C=O, which are in a linear arrangement. The molecular quantum mechanical state of this molecule can be approximated deriving it from classical considerations. In case of the CO₂ molecule the most important IR-energy states at room temperature are rotational and vibrational ones, which can be subject to changes. Without further deduction, the rotational quantum mechanical energy of a linear rotator (such as CO₂) is given by

$$E_{rot}(J, M_J) = hc \underbrace{BJ(J+1)}_{\text{rigid rotator}} - \underbrace{DJ^2(J+1)^2}_{\text{centrifugal distortion}} \quad (1.1)$$

Here, h denotes the Planck constant and c the speed of light. B and D are constants that depend on the molecule i.e. the atomic masses and average bonding distance. The quantum number $J = 0, 1, \dots$ corresponds to the rotational states, whereas $M_J = -J, -J+1, \dots, J$

represents the degeneracy of the linear rotor. This means to a given rotational state J there are $g_J = 2J + 1$ states with identical energy. The first part of the Equation 1.1 corresponds to a rigid rotator. This approximation is refined by the second part, which represents centrifugal deviations in atomic distances from R_0 with increasing rotational energies. This approach assumes that the rotating masses are coupled by a spring with the spring constant k .

Now, this molecule is in the state $\langle J', M'_J |$ and interacts with an electro-magnetic wave and changes its state to $|J, M_J\rangle$. The quantum mechanical coupling operator is given by the dipole moment μ of the molecule.

$$I_{J',M'_J \rightarrow J,M_J} = \langle J', M'_J | \mu | J, M_J \rangle \quad (1.2)$$

A vanishing dipole moment leads to no coupling from an EM-wave with the molecular state and thus, no transition and in turn no molecular absorption or emission⁷. Note that the Equation 1.2 already includes some approximations such as the Born-Oppenheimer approximation, which separates the pure electronic transitions. Additionally, vibrational transitions are separated from this approach. It can be shown, that certain selection rules apply for the rotating, *linear* molecule when it interacts with electro-magnetic waves:

$$\Delta J = 0, \pm 1 \text{ and } \Delta M_J = 0, \pm 1 \quad (1.3)$$

This implies, that the possible energy transitions are proportional to multiples of $2J$. With respect to the spectral perspective, this leads to equi-distant absorption/emission lines in a wave-number calibrated spectrum (see Figure 1.1).

The transition intensities, which refer to the probability to change from one state into another, depend on both the coupling strength given by the dipole momentum μ as well as the population density of the states. The transition probability to change from state l into state u , follows the Boltzmann-distribution to a given temperature T :

$$\frac{N_l}{N_u} = \frac{g_l}{g_u} e^{\frac{-(E_l - E_u)}{k_b T}} = \frac{(2J_l + 1)}{(2J_u + 1)} e^{\frac{-(E_l - E_u)}{k_b T}} \quad (1.4)$$

The transition intensity increases for low J transitions. They are dominated by J until the Boltzmann-factor decreases the population for higher J , referring to higher energies. This forms a characteristic envelope of transition intensities (see Figure 1.1).

The second relevant energetic state of a CO₂ molecule is the molecular vibration. Considering a bi-atomic molecule, the potential can be pictured as displacement of the relative

⁷Homonuclear molecules such as N₂ or O₂ are spectroscopically very in-active. However other processes such as quadrupole momenta or magnetic dipoles might allow transitions despite a vanishing electric dipole moment.

distance x from the equilibrium distance R_0 . This can be approximated by the Morse-potential $V(x)$:

$$V(x) = hcD_e(1 - e^{-ax})^2 \quad (1.5)$$

$$\text{with } a = \sqrt{\frac{k}{2hcD_e}}. \quad (1.6)$$

Here, k corresponds to the spring constant and is in good approximation proportional to the bonding strength and D_e represents the dissociation energy. Solving the Schrödinger-equation for the Morse potential, the corresponding energy states to a given quantum number v are:

$$E_v = (v + \frac{1}{2})\hbar\omega - (v + \frac{1}{2})^2\hbar\omega x_e \quad (1.7)$$

$$\text{with } \omega x_e = \frac{a^2\hbar}{2\mu} \quad (1.8)$$

$$\text{and } \omega = \sqrt{\frac{k}{\mu}} \quad (1.9)$$

The first term of Equation 1.7 is a pure harmonic oscillator and represents a good approximation for low rotational energies. This implies, only small displacements from the equilibrium state R_0 are allowed with this approximation. A refinement poses the inclusion of the harmonic constant x_e .

For EM-transitions from one vibrational stage v to v' , again a selection rule applies. Without exact proof holds (Atkins and De Paula, 2013):

$$\Delta v = \pm 1 \quad (1.10)$$

Analogue to the rotational considerations, this selection rule represents distinct energy differences by the EM-induced transition of a vibrating molecule. For a pure harmonic oscillator, the energy differences for a single photonic transition process would be $\Delta E = \hbar\omega$. In an absorption/emission spectrum, this would lead to only a single transition line. However, anharmonicities in the Morse-Potential result into a linear decrease of the transition energies with higher molecular states v up to the dissociation energy of the molecule.

So the selection rules for rotational and vibrational states offer the general possibility to observe energetic transitions from one state into another. For spectroscopy, the probability of a specific transition is of great interest. The absorption and emission strengths, which are typically observed in a spectrum, are proportional to the transition probabilities. Besides the molecular dipole moment μ , this transition intensity depends on the population density of the corresponding energy level, which follows in good approximation the Boltzmann-distribution to a given temperature T (see Equation 1.4).

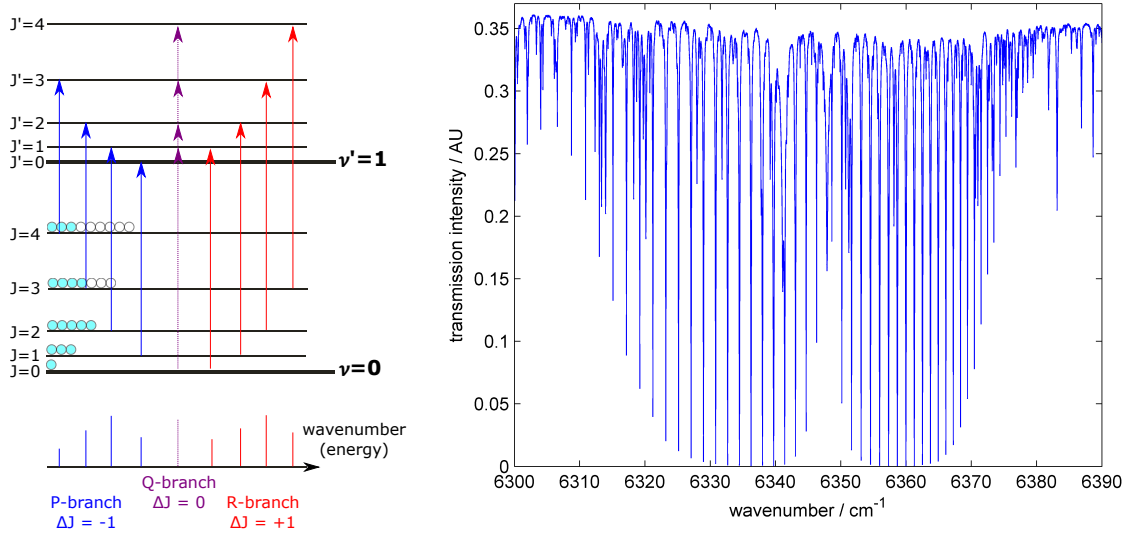


Figure 1.1: Illustration of the rotational-vibrational energy transitions of a molecule (left). The corresponding transition lines in are shown below. The intensity of a particular transition is proportional to the population density of a certain energy level (light blue balls). A high population density results into a high intensity if the transition is allowed by the selection rules. A real atmospheric transmission spectrum of CO₂ is shown right. The P and R branch are clearly visible as absorption lines of CO₂. Note that additional gases -mainly water vapor- are present in this spectrum.

Figure 1.1 summarizes this section. The presence⁸ of a dipole moment μ in a molecule provides the main factor whether an electro-magnetic transition takes place or not. From considerations of the interaction between this dipole moment and the molecular quantum mechanical state of the molecule, the selection rules $\Delta v = \pm 1$ and $\Delta J = 0, \pm 1$ can be derived. With respect to a molecular transition spectrum this results into a subset of permitted transitions forming the P ($\Delta J = -1$), Q ($\Delta J = 0$) and R ($\Delta J = +1$) branch. This P, Q and R-branch repeats as an “overtone” corresponding to $\Delta v = \pm 1$. Besides the selection rule that gives the principle possibility to observe a specific transition, the population density is proportional to the observable transition intensity. If the molecular energetic states are in the order of $k_b T$, the intensities are proportional to the Boltzmann-distribution and form the characteristic envelope of the P or R branch. It is worth to notice, that each molecule, even different isotopologies of the contributing atoms, has a very specific interaction characteristic with electro-magnetic waves, which can be used to identify this particular molecule exactly.

Until now, only the spectral positions and intensities have been discussed, assuming an infinitesimal narrow (δ -like) transition to a discrete energy E . In fact, this discrete energy is broadened by several broadening effects. To begin with the weakest effect, the natural line width broadening: The transition line is broadened by $\Delta\nu \propto \Delta E \propto \hbar/(2\tau)$ with τ

⁸Note that this dipole moment might be non-permanent, such it is the case for CO₂. Further, higher multipole-momenta might lead to allowed transitions, but typically with low intensities as well as other effects.

species	absorption window / cm^{-1}	absorption window / nm
CO ₂	6170 – 6400	1560 – 1620
CH ₄	5890 – 6150	1625 – 1695
O ₂	7760 – 8010 12,820 – 13,330	1250 – 1285 750 – 780
H ₂ O	8353 – 8463	1180 – 1200

Table 1.1: A selection of spectral windows that can be used to retrieve trace gases. These gases (i.e. H₂O) might absorb in other spectral ranges as well.

as the lifetime of the transition due to the Heisenberg-uncertainty relation. Within this work, the natural line broadening is entirely negligible, which might not be the case for higher resolution spectra. Contrary to natural line broadening, two further effects are not negligible for atmospheric absorption spectroscopy: First is the temperature dependent Doppler-broadening effect. Thermic movement of a molecular gas causes a slight wavelength shift in both short and long wavelength range due to the Doppler effect. Typical values of the Doppler broadening width are $\Delta\nu_{doppler} \mathcal{O} \cdot 10^{-3} \text{ cm}^{-1}$ (Hase, 2000). In addition pressure-broadening effects take place, that can be pictured as collision induced deformations of the molecular potential and an influence on transition energies⁹. The pressure-broadening ranges $\Delta\nu_{pressure} \mathcal{O} \cdot 10^{-2} \text{ cm}^{-1}$ at 1000 mbar Kramer (2007). Table 1.1 shows the key absorption windows for the used trace gas retrievals in this work.

As shown before, a molecule has a specific energetic transition characteristic which allows to identify the type of molecule and allows even to distinguish different isotopologies. Besides this qualitative identification, quantitative information can be obtained as well. Assuming a medium with the optical thickness τ , the spectral intensity I_0 is attenuated according to the Beer-Lambert's law:

$$I(\tau, \nu) = I_0(\nu) \exp(-\tau) \quad (1.11)$$

The optical thickness τ might have several dependencies on the optical path $0 - l$ and of the gas specific absorption cross section σ_i and number density n_i for gas i . For N absorbing gases follows:

$$\tau = \sum_{i=1}^N \int_0^l \sigma_i(z, \nu) \cdot n(z) dz \quad (1.12)$$

Starting out with this equation the trace gas concentration $C = n_i/n_{ges}$ can be derived from a spectroscopic measurement as described in chapter 5.

In summary, a qualitative measurement of gases is possible as long as EM-transitions are present in the specific spectral range. If a spectral intensity passes through the absorbing

⁹This can even introduce additional transition pathways. This collision induced absorption/emission features become more relevant, the higher the pressure and temperature of a gas, with respect to the transition energy.

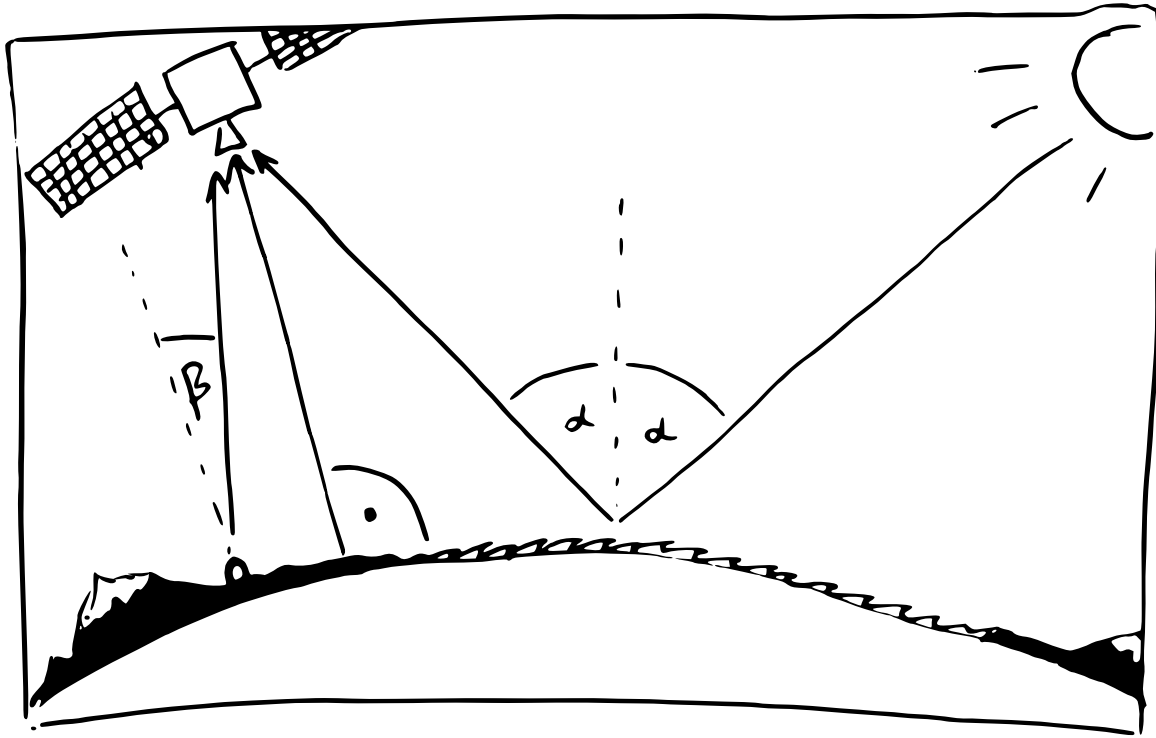


Figure 1.2: NIR-Satellite measurement geometries: **ocean glint** uses the reflection on the oceanic surface with the angle α , **nadir** orthogonal to the earth's surface and **target** with an arbitrary angle β .

gas a known distance, a retrieval of the concentration is possible from the absorption strength (optical thickness τ). The procedure of retrieving the atmospheric concentrations of a trace gases such as CO₂ or CH₄ will be described in chapter 5 in more detail.

The application of remote sensing techniques in monitoring atmospheric concentrations will be introduced in the following.

1.2.2 Satellite remote sensing

Contrary to in-situ approaches, remote sensing enables measurements from space. This comes along with vast global data coverage, even in inaccessible regions such as tropic or boreal parts of the world. Several satellite missions deliver space based data sets of CO₂ and/or CH₄ already. Namely the SCanning Imaging Absorption spectroMeter for Atmospheric CartographY (SCIAMACHY) (Burrows et al., 1995; Bovensmann et al., 1999), Greenhouse gases Observing SATellite (GOSAT) (Yokota et al., 2004) and the recently launched Orbiting Carbon Observatory-2 (OCO-2) (Crisp et al., 2004).

For Short Wave Infra-Red (SWIR) spectroscopy three viewing geometries are common. Figure 1.2 shows these geometries of Near Infra-Red satellite instruments. In the “ocean glint geometry” the satellite points towards the specular ocean surface reflex. Obviously this can only be performed on oceanic regions and under distinct angles with the benefit of a high photon flux and a precise knowledge of the light path. On the other hand both nadir

and target-mode geometry is using the solar illuminated continental surface as light source. In the “nadir” geometry the satellite points perpendicular to the earth’s surface. Here, the surface albedo mainly influences the spectral intensity. In addition some instruments can operate in “target-mode”, where the instrument observes a specific target within visible range. Towards longer wavelengths the self-emission of the atmosphere enables additionally “limb-scanning” geometries where the line of sight is tangent to the earth’s surface such as the Michelson Interferometer for Passive Atmospheric Sounding (MIPAS) instrument (Fischer et al., 2008).

The knowledge of the light path through the atmosphere is essential for the retrieval accuracy. This poses the major challenge in retrieving total column abundances from space based spectra and is the dominant systematic error source (Oshchepkov et al., 2013): Obviously the light passes the atmosphere twice in all geometries with an effective length. Besides that, additional intensity can be scattered into the satellite spectrometer, taking another way through the atmosphere. Butz et al. (2011) could show, that these scattering effects can have both, shortening and enlarging effects on the light path. Unaccounted this leads to higher/lower retrieved trace gas concentrations. Satellite instruments additionally have to cope with low light conditions which results into small signal-to-noise-ratio (SNR). This is the main reason why the standard deviation of satellite soundings towards ground based remote sensing reference sites for a single measurement is in the range of 2.6 ppm for XCO₂ (Oshchepkov et al., 2013) and 14 ppb for XCH₄ (Parker et al., 2011). Here, “XGAS” stands for the measurement of the target gas (GAS) referenced to a simultaneous measurement of a reference gas (oxygen). See subsection 5.4.1 for more details. However, satellite remote sensing provides global coverage of measurements even in remote regions such as the tropics or Siberian tundra. This enables studies on large scale effects like the seasonal cycle for the individual hemispheres or the studies of year-to-year anomalies (e.g. Guerlet et al., 2013a). Satellite data close the gap between the globally sparse distributed, but accurate grounds based measurements and allow science on a global scale.

Several working groups worldwide develop retrieval code that evaluates the satellite spectra and obtains the final XCO₂ and XCH₄ total column per sounding. Within this work basically three retrieval products from GOSAT are used. Two variants of the RemoTeC evaluation code, namely FP-(full physics) and proxy (Butz et al., 2011; Guerlet et al., 2013b; Schepers et al., 2012), as well as the retrieval approach Atmospheric CO₂ Observations from Space (ACOS) ((O’Dell et al., 2012; Crisp et al., 2012)) are used within this work.

The main difference between the RemoTeC-FP and the RemoTeC-Proxy algorithm is the way the light path through the atmosphere is estimated. While RemoTeC-FP retrieves aerosol parameters simultaneously with XCO₂ and XCH₄ and takes multiple scattering effects into account, the RemoTeC-Proxy approach is restricted to XCO₂ only and uses the retrieved CO₂ column together with CarbonTracker-modeled¹⁰ CO₂ as a lightpath proxy. ACOS is, as well as RemoTeC-FP, a full-physics approach i.e. simultaneously retrieving

¹⁰Carbontracker is a data assimilation approach to infer sources and sinks of CO₂ and CH₄ on a regional scale (Peters et al., 2007)

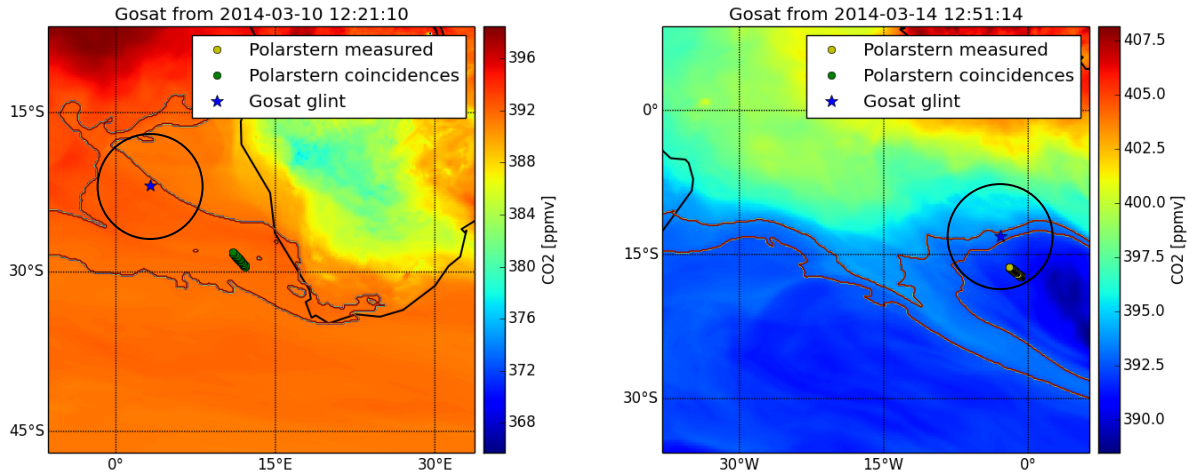


Figure 1.3: Two scenarios that depict the challenges of satellite validation. Both show model-concentration-fields by CAMS of total CO₂ columns along the RV *Polarstern* track. Satellite soundings are indicated by a blue *. Within 4 h temporal coincidence RV *Polarstern* measurements are shown as dots. The black circle represents the 5° spatial coincidence criterion. This criterion gives no coincidence for the left panel. However according to the model-field both agree within ± 0.5 ppm (contour shape). Right panel shows a situation where satellite and ship based measurements are coincident according to the spatial criterion. However, strong gradients in the model field indicate systematic differences here.

XCO₂ and atmospheric scattering properties. Differences between RemoTeC-FP and ACOS relate to details how aerosol and cloud scattering parameters are implemented and how the inverse problem is solved. Most importantly here, ACOS delivers many more data than RemoTeC-FP for ocean-glint soundings since RemoTeC-FP resorts to a conservative cloud and aerosol filtering scheme using the “upper edge” method (Butz et al., 2013). ACOS does not deliver XCH₄.

Comparing satellite remote sensing products with ground based or model products pose a challenging task. Not only the measurement geometries differ (direct sunlight versus scattered sunlight) but also the retrieval procedure including the used a-priori profile (see section 5.1) and different sensitivity with respect to altitude. Rodgers and Connor (2003) suggested a systematic approach to inter compare these products properly. However, for the comparison with all the GOSAT products the smoothing effect of the averaging kernel matrix is neglected within this work. Compared to systematic errors introduced by temporal and spatial distance these effects are assumed to be negligible.

An additional challenge poses the temporal and spatial coincidence. This might be given for comparing model data with measurement data, since model data can be interpolated to the measurement coordinates. However, comparisons from ground based measurements to satellite data can rarely co-inside directly in space and time directly. To overcome this problem the recently launched OCO-2 satellite can be operated in a target-mode, which allows pointing directly to a ground based site. But still, there are residual differences since the satellite integrates a broader column than the remote sensing instrument.

However, ground-based-satellite inter comparisons can be performed on a statistical level if enough measurement data is available (Morino et al., 2011; Parker et al., 2011). Here a spatial (e.g. $2 \times 5^\circ$ latitude/longitude) and temporal (e.g. ± 1 hour) coincidence criterion is defined and the data inter compared. Oshchepkov et al. (2012) suggested a refinement of this approach by inter-connecting the measurements with model-fields if the data set is too sparse for a statistical analysis. Within this approach, two measurements are considered coincident if the corresponding model-fields at the particular geo-location deviate less than a given threshold (e.g. 0.5 ppm) from each other. Figure 1.3 depicts the advantages of this approach compared to the simple radius based approach and compares it to the pure spatial/temporal approach. Left panel shows positive coincidence with the model-field, but flags no coincidence within the spatial/temporal criterion. The opposite case is depicted by the right panel, where model-fields indicate no coincidence despite the spatial/temporal criterion does. However, shortcomings of this approach is that it relies on accurate model fields and depends on the model resolution - high resolution model fields will lead to fewer coincidences since less fields are connected. In addition the spatial distance within this approach is neglected, which would allow co-incidences along a large spatial distance. Within this work the spatial/temporal criterion is used.

1.2.3 Ground based remote sensing

Basically two ground based networks operate worldwide in order to retrieve atmospheric greenhouse gases with remote sensing techniques. The high resolution ($R := \frac{\Delta\nu}{\nu} \approx 3 \cdot 10^5$) Fourier Transform Spectrometers (FTS) operate in direct sunlight spectroscopy. This means, the solar light beam is feed directly into the spectrometers entrance. This allows retrieving the total column of a trace gas along the line of sight trough the atmosphere. Influences on the light path due to the presence of aerosols or other scattering effects that shorten or enlarge the light path in satellite sounding are of minor importance since the direct sunlight is the predominant source of intensity, which makes complex radiative transfer calculations obsolete. This allows to achieve accuracies in the total column product of 0.8 ppmv¹¹ for XCO₂ and 7 ppbv¹² for XCH₄ respectively (Wunch et al., 2010). Shortcomings of remote sensing in direct sunlight spectroscopy in general are that the measurement is only possible under good weather conditions i.e. the sun is not obscured by clouds or other objects. In addition the knowledge of the atmospheric condition (i.e. pressure and temperature) is of utmost importance for an accurate retrieval. Further the high resolution instruments of network instruments from TCCON or NDACC require infrastructure, a large, temperature stabilized container housing and frequent maintenance (refill of cooling liquid, calibration) and do not allow to perform campaign based flexible measurements. Previous attempts to operate these instruments on a mobile platform yield into a sparse data set (Notholt et al., 1995). In order to characterize sources and sinks of greenhouse gases, more flexibility would

¹¹parts per million volume mixing ratio

¹²parts per billion volume mixing ratio

allow for a specific deployment of such instruments nearby large scale sources such as cities, volcanoes or wetlands.

Within this work the ground based remote sensing technique is used. Packing box sized instruments are used to perform ground based remote sensing in direct sunlight spectroscopy on a campaign basis from mobile platforms to retrieve atmospheric CO₂ and CH₄. This allows inferring global effects such as the interhemispheric gradient of trace gases along a ship based campaign. Details on the solar tracking device will be given in chapter 2. The two different instruments are used within this work will be described in more detail in the upcoming sections. A small Fourier Transform Spectrometer (EM27/SUN) that has been developed for ground based remote sensing approaches by Gisi (2012) in cooperation with Bruker Optics (see chapter 3). The second instrument is a self-developed grating spectrometer (GRC) that is presented in chapter 4.

2 Solar tracking device

Measuring atmospheric trace gases by direct sunlight spectroscopy as described in subsection 1.2.3, implies the need for a device that feeds the solar beam into the spectrometer's entrance aperture. Since the air mass is an important retrieval parameter and assumed to be the direct light-path towards the center of the solar disc, deviations here would introduce directly systematic errors in the retrieval. In order to keep the tracking induced relative error below the targeted 0.1 %, (Gisi, 2012) showed, that a tracking accuracy of at least 0.05° is needed.

Rather than pointing the spectrometer with its entrance aperture directly towards the sun, as it is performed by hand held sun-photometers (Volz, 1974; Brooks and Mims, 2001) for example, automated systems are desired especially for larger devices. This automated system can be designed in a way, that it orientates two mirrors such, that the solar beam is constantly fed into the spectrometer's entrance. Since this device is able to track the sun along its movement over the sky hemisphere it is called "solar tracking device" or just "solar tracker".

In the following chapter the working principle of the solar tracker will be described. It has been updated in the framework of a Master's thesis by Bertleff (2014). The initial solar tracker developed by Gisi et al. (2011) was able to follow the relatively slow solar movement under stationary operation with angular speed that did not exceed $4.2 \cdot 10^{-3} \text{ }^\circ\text{s}^{-1}$. To develop the general measurement setup towards more mobile and flexible applications, stronger movement compensations are desirable. It will be described, how the initial stationary solar tracker can cope with faster movements of several degrees per second. Finally the performance of the adapted solar tracker will be analyzed. Basis is the record during a measurement campaign on board the research vessel "Polarstern". Based on this analysis, an estimate of the tracking requirements for car-applications will be given. Part of this chapter are summarized from the publication Klappenbach et al. (2015) and the Master thesis by Bertleff (2014).

2.1 Setup of the solar tracker

Each point on the sky hemisphere can be described by two angles: Azimuth (ϕ) and elevation (θ). So a system that can compensate for two degrees of freedom is desired. Two mirrors mounted on a rotation stage, with the rotating axis arranged perpendicular to each other, can optically connect the spectrometers entrance with each point in the sky

hemisphere. Each point on the sky hemisphere can be described by two angles: Azimuth (ϕ) and elevation (θ). So a system that can compensate for two degrees of freedom is desired. Two mirrors mounted on a rotation stage, with the rotating axis arranged perpendicular to each other, can optically connect the spectrometers entrance with each point in the sky hemisphere. For the use under extremely harsh environments (e.g. volcanic corrosive plume, sea salt or sandblast) these mirrors might need to be protected or replaced periodically (Feist et al., 2015).

The task to achieve automated tracking of the solar disc while it moves across the sky can be performed by calculating the solar position and/or implement an active feedback mechanism.

To begin with a stationary case, where the initial orientation of the instrument is known and left unchanged: At a given geo-location (latitude, longitude, altitude) and a specific time the solar position can be calculated. However, this calculation is not trivial since the earth rotation changes due to tidal friction or unpredictable changes of the earth's moment of inertia. These changes are typically on the order of several $10^{-4} \text{ }^\circ \text{ day}^{-1}$ (Vondrák and Richter, 2004). Additionally atmospheric refraction changes the solar zenith angle by up to 0.7° (Gisi et al., 2012) and is also variable over the day due to changes in the atmospheric pressure. Since this scientific information needs to be available in real time for pure astronomical tracking, this approach seems not practical. In addition it requires highly accurate initial orientation of the instrument in all the three axes.

So early solar tracking approaches came up with an active feedback system (Adrian et al., 1994; Notholt et al., 1995; Washenfelder et al., 2006) using a quadrant diode. However this approach has its disadvantages. Gisi et al. (2011) showed, that deviations using this approach can exceed 0.08° that introduces a systematic error significantly above 0.1% in the retrieved CO_2 trace gas abundance. The most severe flaw of this approach is, that a systematic deviation occurs if the quadrant diode is not carefully aligned with the spectrometer's setup.

Gisi et al. (2011) proposed an active system that observes the spectrometer's aperture with a camera and calculates the current position p_{current} of the solar disc. The resulting deviation $e := p_{\text{current}} - p_{\text{desired}}$ of the solar disc is used to adapt the azimuth and elevation motors accordingly.

With this approach corrections for the mirror positioning motors are linked directly to the desired solar position and brings the advantage of a high absolute pointing accuracy. In the following this tracking principle will be called "fine tracking".

In stationary operation, on start-up the initial position is found with astronomic calculations combined with a search pattern. Since this approach was designed for stationary operation only the system had only to cope with the relatively slow angular velocities in the order of $v < 4.2 \cdot 10^{-3} \text{ }^\circ \text{ s}^{-1}$. A moving platform, such as a ship, poses two additional challenges:

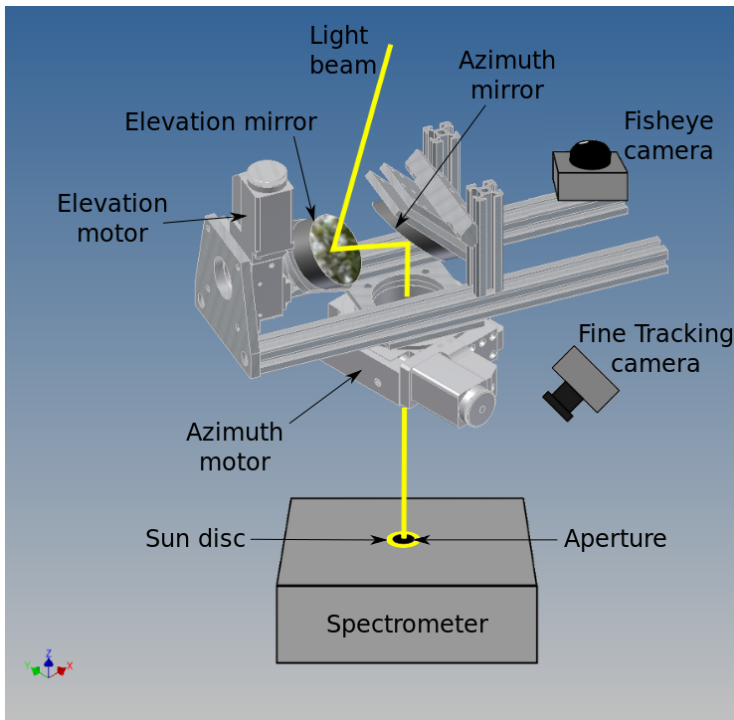


Figure 2.1: Function-principle of the solar tracing device, connecting each possible point of the sky hemisphere optically to the spectrometer’s entrance aperture. Cameras supply optical feedback on a software package, which is in control of the azimuth and elevation motors. These motors adjust such, that the light beam is feed into the spectrometers entrance aperture. Picture taken from Bertleff (2014)

- At start-up or after interruptions of the tracking operations, the solar tracker needs to find the solar disk without knowledge of the observatory’s orientation.
- The control feedback cycle needs to cope with the potentially fast motion of the platform in addition to the slow motion of the solar disk.

Basically, the implemented tracking procedure can be split into two parts, that tackle these required adaptations: the coarse and the previously introduced fine-tracking mode. The latter is a refinement of the concept proposed by Gisi et al. (2011). Both require additional or exchange of hardware. Figure 2.1 shows the implemented setup.

In order to bring the solar disc into the field of view (FOV) of the fine-tracking camera the coarse-tracking mode is used. This tracking mode relies on a 185° fish eye-lens (Lensation, BFM2320) that is mounted on a CMOS digital camera (VR-magic, model C-9+ PRO BW CMOS, 1288×1032 pixel²) and observes the entire sky hemisphere above the instrument. The brightest spot on the camera image gives the approximate position of the solar disk. A look up-table that was generated through lamp calibration in the laboratory translates image positions into azimuth and elevation angles of the tracking mirrors.

The angular resolution of the coarse-tracking is approximately 0.15° pixel⁻¹ and is strongly variable within the FOV. Thus, it is not accurate enough to perform the entire tracking process with the desired accuracy of 0.05° . However, the coarse-tracking ensures that the solar disc of about 0.53° diameter can be located within the field-of view of the fine-tracking camera in the order of 10 – 15° .

Once the solar image is located within the FOV of the fine-tracking camera (VR-magic, model C-9+ PRO BW CMOS, 1288×1032 pixel, $f = 50$ mm), coarse-tracking goes idle and fine-tracking mode takes over and centers the solar image on the aperture of the

Table 2.1: Leading contributions to the duration of fine-tracking control cycles of the solar tracker (average values retrieved from housekeeping data logged during the measurement campaign aboard RV *Polarstern*).

Task	Duration ms
Image acquisition	≈ 10
Image processing	< 3
Motor position request	5–10
Update motor speed	5–10
Overall average	≈ 22

spectrometer through a circle fitting routine. From this routine the current position $p_{current}$ is obtained and can be compared with the desired position $p_{desired}$.

In order to enhance the tracking velocity for a moving platform, it is essential to update the motor control parameters (position, speed or acceleration) as frequently as possible. To minimize the time lost during communication between the fine-tracking camera and the control unit (Embedded PC-System, ARK by Advantech), the camera only transmits a region of interest of approximately 200 pixel² out of the full camera frame of 1288 pixel \times 1032 pixel via USB. Additionally each motor is connected via its individual RS485 connection to the control unit to enable simultaneous send and receive to/from both motors. Based on this hardware setup, the custom-built image acquisition, processing and motor control software achieves control cycle durations on the order of 20–30 ms corresponding to an update frequency of 33–50 Hz. Table 2.1 summarizes individual contributions.

To enhance the performance additionally a proportional-differential-integral (PID) controller is used. Without using this approach, the tracking system would always lag behind the last correction. With the update rate of $\tau = 30$ ms this system could only compensate angular velocities $v_{max} < \frac{e_{max}}{\tau} = 1.5 \text{ }^\circ\text{s}^{-1}$. A PID control calculates and sets a time dependent control variable $V(t)$ (motor position, velocity or acceleration) in dependence of the deviation e .

$$V(t) = \kappa_P e + \kappa_I \int_{t-\Delta t}^t e dt + \kappa_D \frac{de}{dt} \quad (2.1)$$

Here, the PID-parameters κ_P, κ_I and κ_D are determined empirically. Typically higher values make the system more responsive to deviations e but can cause them to oscillate or over shoot. Smaller values however make the system more stable. Further details on PID controlling can be found in literature (e.g. Lunze, 2013).

The choice of the control variable V is of additional importance. The stepper motors have the option to set a new position, velocity or acceleration. Bertleff (2014) could show that for moving systems the acceleration variable is the best choice to minimize the residual tracking error under movement. However, for stationary applications this system is too responsive and the tracking residual could be lowered by approximately 60% under the use of the angular velocity as control variable V .

2.2 Performance of solar tracking device

The described solar tracker was taken out for a measurement campaign on board the research vessel RV-Polarstern operated by Alfred-Wegener-Institute, Bremerhaven, Germany. Two spectrometers were operated in direct sunlight spectroscopy whilst most important tracker parameters were recorded. This allows a performance analysis of the tracking accuracy for a mobile, pitching and rolling platform. For simplicity reasons only the tracker of the EM27 instrument is evaluated. However, the tracking device of the GRC instrument shows a very similar performance.

The solar tracker was operated upon a five week ship cruise over the Atlantic Ocean. The software recorded all major tracker parameters (angular position, velocity, tracking error) into a log file for every PID update interval of approximately 30 ms. The data set covers over 103 hours of solar tracking including all deviations forced due to shadowing by the ship's infrastructure or clouds. The total tracking error of both azimuth and elevation component e_{tot} can be calculated from Equation 2.2 since azimuth and elevation are perpendicular to each other and form an orthogonal basis.

$$e_{tot} = \sqrt{e_{az}^2 + e_{el}^2} \quad (2.2)$$

Figure 2.2 shows a typical record of the tracker parameters during the campaign. The azimuth and elevation angles oscillate gently around an average value with an amplitude of a few degrees (upper panel). Compared to the position the angular velocity v oscillates with a $\frac{\pi}{2}$ phase shift with a few spikes (second panel). These spikes translate into strong angular accelerations a (third panel). After start up at $t = 0$ the tracker total residual e_{tot} decreases and stabilizes within the first 10 seconds (lowest panel).

The temporal interval of 120 s represents a typical time span for two total column scans from the EM27 instrument with a scan-time of 58 s for a 10 fold average double-sided interferogram (see chapter 3).

Figure 2.2 shows further, that the angular position and angular velocity does not correlate with the total tracking error e_{tot} . In contrast, a clear correlation can be seen with the angular acceleration a . This correlation can be used to give a performance estimate on the solar tracker for the azimuth and elevation component upon. The maximum angular a_{max} acceleration the system can compensate without exceeding the desired $e_{max} = 0.05^\circ$ accuracy criteria can be derived from this analysis. To overcome sampling artifacts from unevenly spaced intervals the angular velocity and angular acceleration is smoothed with a 5 fold running mean on the tracker data.

Figure 2.3 shows the color coded histogram of the entire data set for azimuth (left) and elevation (right). There is a clear linear dependency that is fitted with a linear polynomial $e = ma + b$. The slope m represents the tracker responsiveness: A perfect tracker $m = 0$ would show no dependence on the angular acceleration.

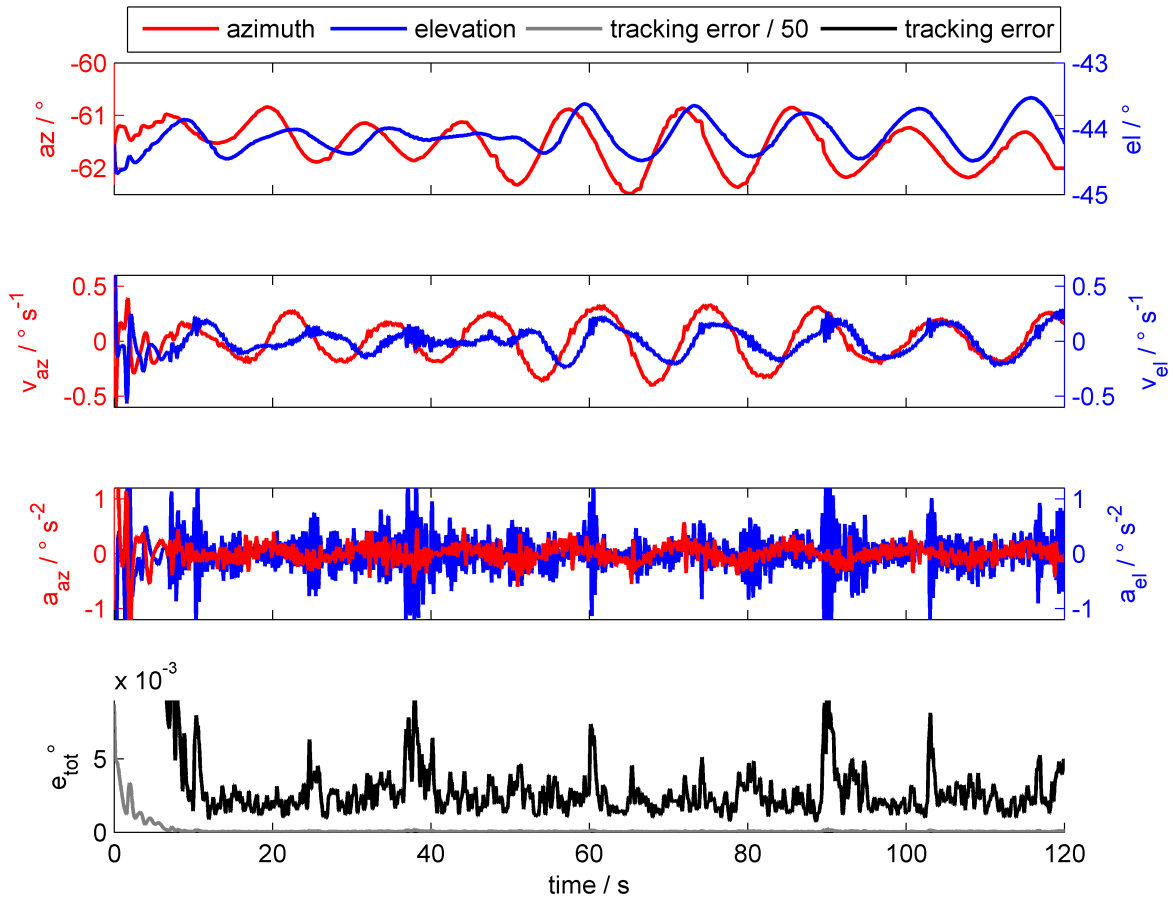


Figure 2.2: A typical tracking situation during the ship campaign. Azimuth is shown in red, elevation in blue. The upper panel shows the angular movement, that the ship produces in angular units. The next panels show the angular speed and angular acceleration for azimuth and elevation. The last plot shows the typical transient oscillation of the total error e_{tot} that stabilizes within the first 10 seconds. A clear correlation of angular acceleration with the tracking error is visible.

Parameter	set 1	set 2	unit
κ_P	0.1099	0.15	s^{-2}
κ_I	0.1128	0.17	s^{-2}
κ_D	25.0	32.0	s^{-2}
m_{az}	$-1.350 \cdot 10^{-2}$	$-6.842 \cdot 10^{-3}$	s^2
m_{el}	$-6.438 \cdot 10^{-3}$	$-4.342 \cdot 10^{-3}$	s^2
a_{max}	3.4	6.3	$^\circ s^{-2}$

Table 2.2: Two different sets of PID parameters (κ_P, κ_I and κ_D) had been evaluated for both the azimuth and elevation component. The linear relation between the angular acceleration a and the tracking error is represented by m (sign is convention). An ideal tracking instrument would yield $m=0$.

During the campaign the PID parameters had been changed from set 1 (green line) to set 2 (red line). Table 2.2 shows the derived parameters and the corresponding PID-parameter-sets. The maximum angular acceleration a_{max} this system can compensate without permanently exceeding desired tracking accuracy can be calculated using Equation 2.4. Here the offset b is neglected:

$$a_{max} = \frac{e_{max}}{m} \quad (2.3)$$

$$a_{max,tot} = \frac{e_{max}}{\sqrt{m_{az}^2 + m_{el}^2}} \quad (2.4)$$

Equation 2.3 can be derived combining Equation 2.2 and Equation 2.3.

The overall performance of the solar tracker during the campaign is shown in Figure 2.4. Here, the color code represents the logarithm of the number of occurrence within a $4 \cdot 10^{-4}^\circ$ interval of azimuth and elevation errors. An ideal tracker would accumulate all points in the center of the panel. The accuracy requirement of 0.05° is encircled in red and contains 98.2% of the entire data set. Note that un-trackable deviations due to clouds or shadowing by the ships infrastructure are included in this data set so this analysis serves as a conservative estimate. Additionally the 1σ and 2σ region is shown, that correspond to 68.3% and 95.5% of the entire data set.

Since this solar tracking system is able to cope with movements on a ship, the question arises how it would perform on a car for example. Figure 2.5 shows a typical tracking situation on a car from a test campaign at mount Etna in Sicily (Butz et al., 2016). The record here is sampled with approximately 400 Hz, so high frequency variations can be made visible. Analogue to Figure 2.2 the angular position, velocity and acceleration are shown. Assuming that the solar tracking system used on the ship campaign responds linear to angular accelerations from a car (see Equation 2.3), the resulting residual $e_{car,tot}$ can be calculated using

$$e_{car,tot} = \sqrt{(a_{az}m_{az})^2 + (a_{el}m_{el})^2}. \quad (2.5)$$

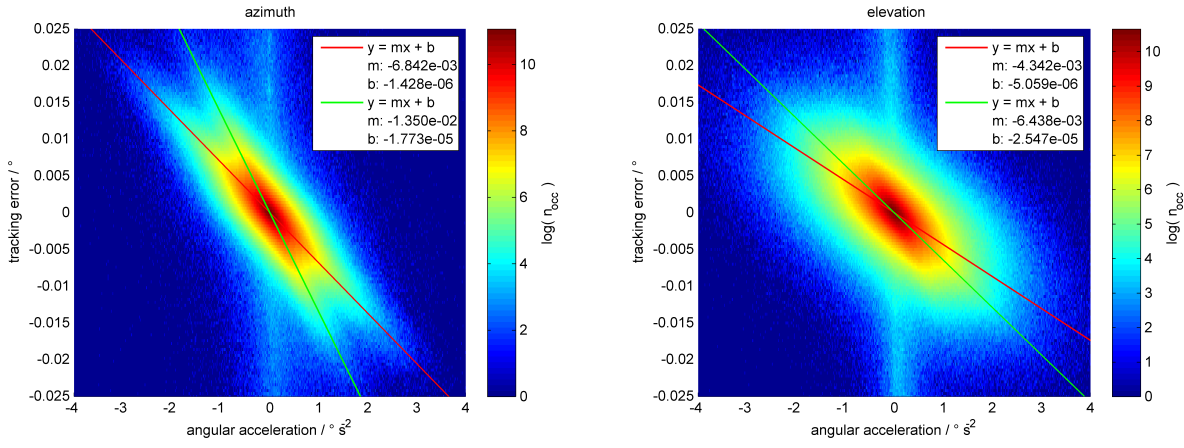
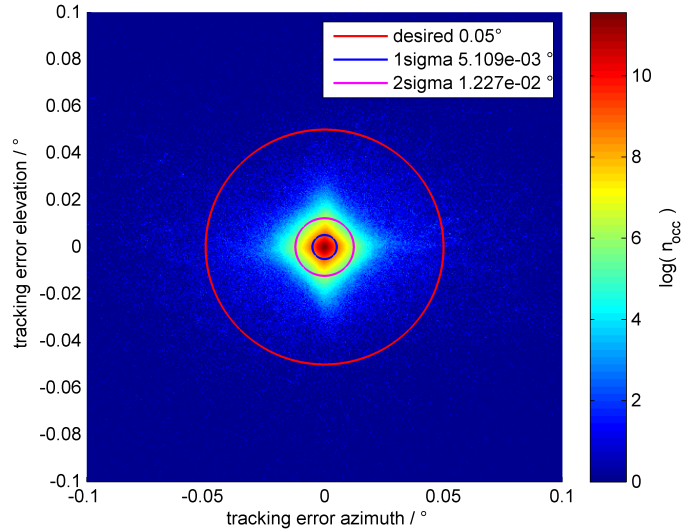


Figure 2.3: Color-coded histogram of the tracking error e (ordinate) in dependence of the angular acceleration a (abscissa) for the azimuth component (left panel) and the elevation component (right panel). There are two PID-parameter sets used (see. Table 2.2) to fit a linear dependency: Set 1 (green) and set 2 (red).

Figure 2.4: Performance of the solar tracker. The figure shows color coded the number of occurrence (n_{occ}) of tracking deviations in dependence of elevation (abscissa) and azimuth (ordinate) within a $2 \cdot 10^{-4}$ interval. An ideal device would accumulate all measurements in the center. Additionally the desired tracking accuracy requirements of 0.05° is encircled (red) and the corresponding 1σ (68.3%, blue) and 2σ (95.5%, magenta) regimes.



The lower most plot of Figure 2.2 shows this calculated residual. The deviation is far beyond the desired tracking accuracy of 0.05° . Hence, using this solar tracker on a car poses an additional challenge and requires further modifications. In order to suppress these strong angular variations a decoupling of the instrument from the platform might be appropriate. Note, that the actual angular movements can vary strongly depending on the speed of the car, the damping system as well as on the condition of the road itself.

In conclusion, the initial solar tracking device by Gisi et al. (2012) could be modified in the framework of a master's thesis such, that accurate and reliable solar tracking on a moving platform such as a ship was possible with great performance. The performance analysis within this work is based on 103 hours of campaign data. It could be shown, that the required tracking accuracy of 0.05° could only be disrupted by un-track-able situations such as shadowing by the ship's infrastructure or clouds. A quantitative analysis could

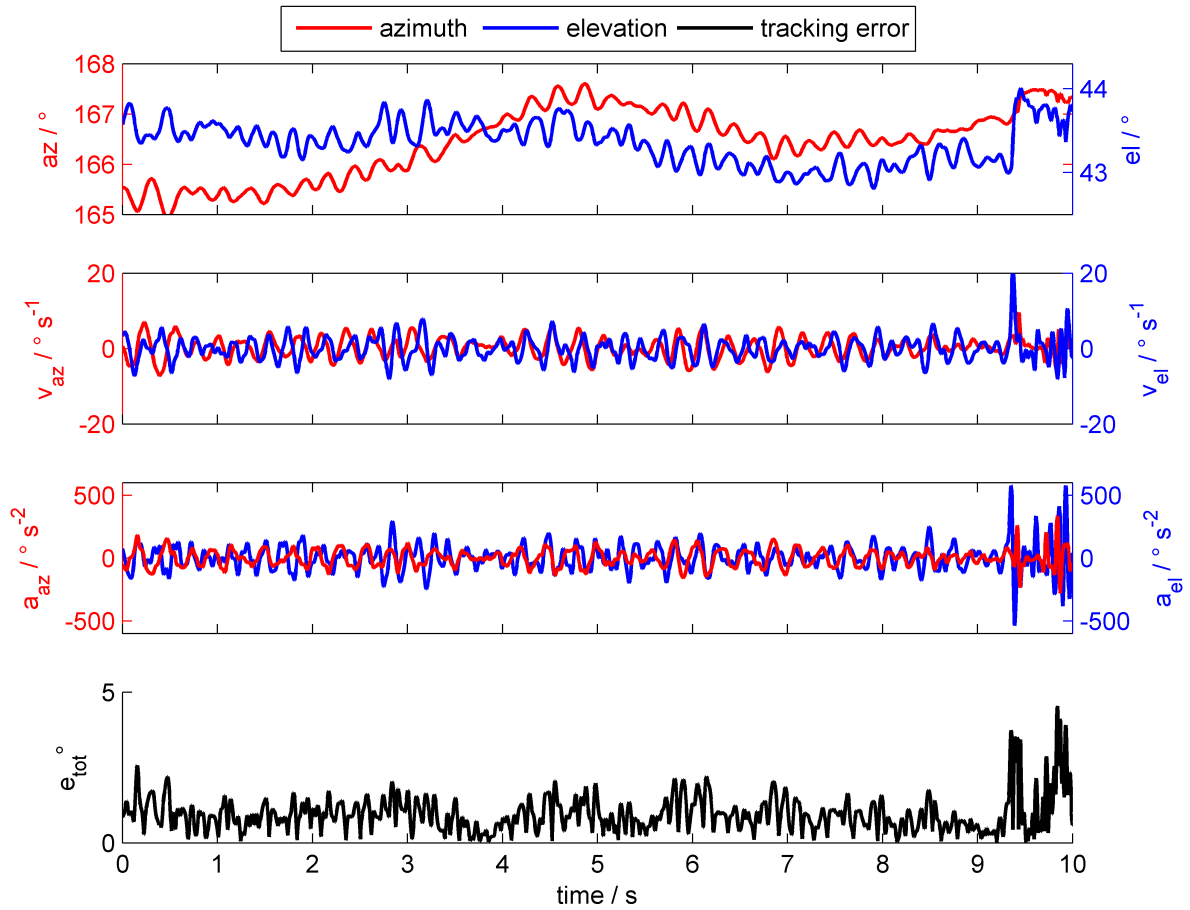


Figure 2.5: A typical tracking situation how it would occur on a car. Azimuth is shown in red, elevation in blue. The upper panel shows the angular movement in angular units. The next panels show the angular speed and angular acceleration for azimuth and elevation. The bottom panel depicts the tracking error $e_{tot}(a)$ using Equation 2.5. Note the narrowed time-span compared to Figure 2.2. In general the angular accelerations exceed the one that occur on a ship by far. Data from Julian Kostinek.

show that this system is able to compensate for angular accelerations of up to 6.3°s^{-2} for both azimuth and elevation.

Finally the use of this implementation for mobile applications on a car is in theory investigated. Extrapolation of this performance to a more agile vehicle than a ship (e.g. a car) revealed that the strong angular accelerations pose an additional challenge for the advanced solar tracking system. Mechanical decoupling from the platform as well as increased PID-cycle frequencies might prepare the solar tracking device for such a challenging application.

3 The miniature Fourier Transform spectrometer EM27 / SUN

As described in section 1.2, atmospheric trace gas abundances can be measured using spectroscopic approaches. For ground based measurements in the near-infra red (NIR, $0.8 \approx 2.0 \mu\text{m}$ wavelength) Fourier transform spectrometers (FTS) are widely used in atmospheric monitoring such as within TCCON¹ or NDACC². In the following a short introduction on Fourier transform spectrometry will be given. Starting out with a brief theoretical introduction the practical aspects of Fourier transform spectrometry will be sketched. Namely a description of shortcomings of intensity fluctuations during the sampling process and additional quality filters. Focus is put here upon the miniature FTS EM27 by Bruker Optics.

3.1 Fourier transform spectrometry

Contrary to grating spectrometers (see chapter 4), Fourier transform spectrometers record the spectrum as an interferogram ($I(x)$) in the Fourier space. The Fourier transformation \mathcal{F} converts this interferogram into the spectrum $S(\nu)$.

$$I(x) = \mathcal{F}^{-1}(S(\tilde{\nu})) = \int_{-\infty}^{\infty} e^{i2\pi\tilde{\nu}x} S(\tilde{\nu}) d\tilde{\nu} \quad (3.1)$$

$$S(\tilde{\nu}) = \mathcal{F}(I(x)) = \int_{-\infty}^{\infty} e^{-i2\pi\tilde{\nu}x} I(x) dx \quad (3.2)$$

i denotes the imaginary number and $\tilde{\nu}$ the wave number. The optical path difference $x = OPD$ can be introduced with multiple approaches depending on the application. For instance optical fibers, plain parallel plates, optical resonators or Michelson interferometers can introduce the optical path difference. Widely used in FTS instruments is the Michelson interferometer. It consists of a beam splitter that divides the collimated entrance beam into two beams. One of the beams usually serves as reference, remains unchanged³ and is directly reflected back into the beam splitter after traveling the optical path of x_r . The second beam is reflected back as well into the beam splitter, but here, the mirror is mounted

¹TCCON stands for Total Carbon Column Observing Network

²NDACC stands for Network for the Detection of Atmospheric Composition Change

³In case of the EM27 instrument both mirrors move and introduce the double optical path difference $OPD = 2 \cdot x$ with the mirror movement x .

movable in x and introduces the optical path difference $OPD = x_r - x$. At the remaining, fourth face of the beam-splitter the interference of the two optical paths (reference and moving mirror) can be observed in the focal plain of a lens with a detector. The detector records to each optical path difference $x + \Delta x$ the intensity $I(x)$ and converts it into a digital signal⁴. In theory the function $I(x)$ is a continuous function. However, in practical applications it only can be recorded in N discrete steps $I(x_n)$. This means the integral Equation 3.1 and 3.2 can be represented by:

$$I(x) = \sum_{m=1}^N S(\tilde{\nu}_m) e^{i2\pi x_n \tilde{\nu}_m} \quad (3.3)$$

$$S(\tilde{\nu}_m) = \sum_{n=1}^N I(x_n) e^{-i2\pi \tilde{\nu}_m x_n} \quad (3.4)$$

So the continuous integral Equation 3.1 and 3.2 is replaced by the sum of discrete measurement steps and transformed with the discrete Fourier transformation into the spectral space. Note, that here the integration limits changed from infinity to the measurement constrained $x_{max} = OPD_{max} = x_N$ (x_{min} analogue). Equation 3.4 thus can be pictured as an approximation of Equation 3.2 with $x_{max} \rightarrow \infty$. Further it is important to mention that the number of samples (N) have to follow the Nyquist-Shannon sampling theorem:

$$\frac{1}{\Delta x} > 2 \cdot (\tilde{\nu}_{max} - \tilde{\nu}_{min}) \quad (3.5)$$

This side constraint avoids ambiguous frequencies that would occur since a discretely sampled periodic function can be represented by a frequency higher than the maximum sampling frequency.

The optical path difference of the interferometer is usually varied continuously, since a stop-record-go pattern would lead to mechanical wear and unprecise movement due to the fact that the static friction of the moving mechanics would have to be overcome each sampling interval. In order to record the continuously varying intensity $I(x)$ within an interval Δx , a reference laser beam travels the same optical path as the measurement beam through the interferometer. An infinite small line width of the laser (which is a good approximation for most applications) yields to the resulting reference interferogram $I_{ref}(x) \propto \cos(x)$. The interferometer electronics can be designed such, that each zero crossing of the reference interferogram triggers the measurement electronic to perform a read out. Typical sampling frequencies are in the order of a few ten kHz. Using a Helium-Neon-laser as a reference with a wavelength of 632.988 nm this corresponds to an optical path difference of the same distance for each zero crossing. This implies high accuracy requirements regarding the optical setup. After analog to digital conversion (ADC) the result is stored as a series of interferogram intensities $I(x_n)$ with the sampling interval Δx . This signal now can computationally be processed with the fast Fourier transformation FFT.

⁴ Detector imperfections (see section 4.6) might introduce errors here.

It is of major importance that the sampling is equidistant. A non-equidistant sampling would lead to sampling artifacts such as sampling ghosts (Dohe et al., 2013).

Because the instrumental line shape (ILS) is of key importance in the trace gas retrieval (see section 5.2) a brief introduction on the ILS in FTS will be given. The ideal ILS of an FTS instrument can be achieved with an infinite number of sampling points and $I_{inf}(x)$ to an infinite large optical path difference in short: The ideal instrument. Real instruments truncate this ideal measurement by the maximum optical path difference OPD_{max} . It follows:

$$S_{instr}(\hat{\nu}) = \mathcal{F}[I_{instr}(x)] \quad (3.6)$$

$$= \mathcal{F}[I_{inf} \cdot box(x)] \quad (3.7)$$

$$= \mathcal{F}[I_{inf}] * \mathcal{F}[box(x)] \quad (3.8)$$

$$= S_{inf}(\hat{\nu}) * \frac{\sin(2\pi OPD_{max}\hat{\nu})}{2\pi OPD_{max}\hat{\nu}} \quad (3.9)$$

Here S_{instr} denotes the spectrum measured by the instrument. In the step from Equation 3.7 to Equation 3.8 the folding theorem is used, where $*$ denotes the convolution operator. Assuming

$$S_{inf}(\hat{\nu}) = \delta(\hat{\nu} - \nu_0) \quad (3.10)$$

$$\text{with } \delta(x) := \begin{cases} \infty & \text{if } x = 0 \\ 0 & \text{otherwise} \end{cases} \quad (3.11)$$

directly follows that the ideal ILS of an FTS is proportional to the $sinc(\kappa) := \sin(\kappa)/\kappa$ as the instrument's response function. The theoretical resolution of an FTS that is only limited by OPD_{max} is given by

$$\Delta\hat{\nu} \approx \frac{0.6035}{OPD_{max}}. \quad (3.12)$$

To reduce sampling artifacts the interferogram $I(x)$ can be filtered such, that the endpoints vanish i.e. $I(x_{min}) = I(x_{max}) = 0$. This causes the resolution further to decrease slightly depending on the used filter. As a rule of thumb the resolution of an FTS can be written as

$$\Delta\hat{\nu} \approx \frac{0.9}{OPD_{max}}. \quad (3.13)$$

For the EM27/SUN ILS parameters are inferred from lab-air measurements as performed by Frey et al. (2015) using water vapor absorption as a reference gas. The retrieval of the ils from the grating instrument (GRC) is describe in section 4.8 in more detail.

The used FTS instrument in this work is an EM27/SUN by Bruker Optics. Its properties will be discussed in the following in more detail.

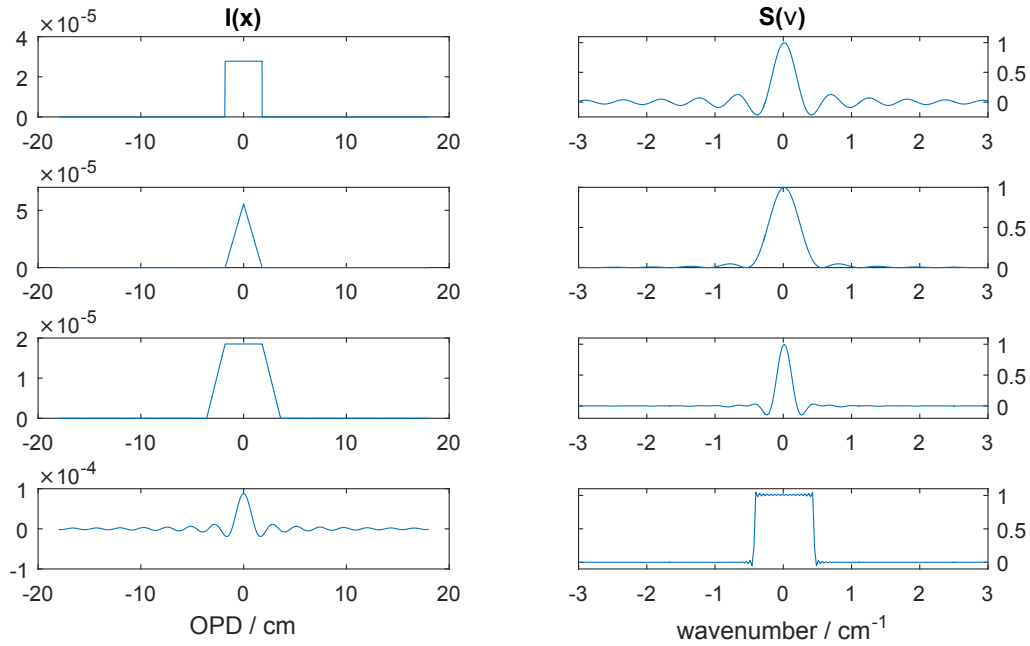


Figure 3.1: Functions in the Fourier space $I(x)$ (left) and their Fourier transformation $S(\hat{\nu})$ (right). a) $box(w = 1.8 \text{ cm})$, b) $tirag(1.8 \text{ cm})$, c) $trap(1.8 \text{ cm}, 1.8 \text{ cm})$ and d) $sinc(\frac{\pi x}{2 \cdot 1.8 \text{ cm}})$. The OPD_{max} of 1.8 cm corresponds to the resolution of the EM27.

3.2 Optical setup of the EM27

Central piece of the EM27/SUN⁵ Fourier Transform spectrometer (FTS) by Bruker OpticsTM is a cube corner pendulum interferometer as sketched in Figure 3.2: The collimated $\approx 40 \text{ mm}$ entrance beam enters the instrument's wedged window. The wedge suppresses Fabry-Perot etalon (see subsection 4.6.3) and additionally filters the visible part of the spectrum in order to avoid stray light on the detectors. A flat mirror can toggle from the external input to the internal calibration lamp. The light beam is then separated by a CaF_2 beam splitter into two individual light beams. They are reflected back into the beam splitter by two cube-corner retro-reflectors. The cube corners are mounted on a pendulum such, that the pending arms introduce the optical path difference of up to 1.8 cm. Since both cube corners move at the same time an effective travel of just $\frac{1.8}{2} = 0.9 \text{ cm}$ is needed. From the remaining face of the beam splitter, the exit beam is reduced in diameter by a $\approx 3 \text{ mm}$ aperture and then focused on the 0.6 mm aperture with a $f = 127 \text{ mm}$ off-axis paraboloid mirror. The corresponding semi-field of view (sFOV) is 2.36 mrad which in turn corresponds to 56% of the solar disc diameter. Directly behind that aperture is a diffuser followed by the 1 mm^2 InGaAs photo-detector with a spectral sensitivity of $5000 - 11000 \text{ cm}^{-1}$, that converts the photon signal into digital values. This spectral range is suited to obtain trace gas information from CO_2 , CH_4 , O_2 , H_2O . In addition the retrieval on HF (hydrogen fluoride) and HCl (hydrogen chloride) can be performed if concentrations exceed the detection limit

⁵SUN denotes the shipping with solar tracker

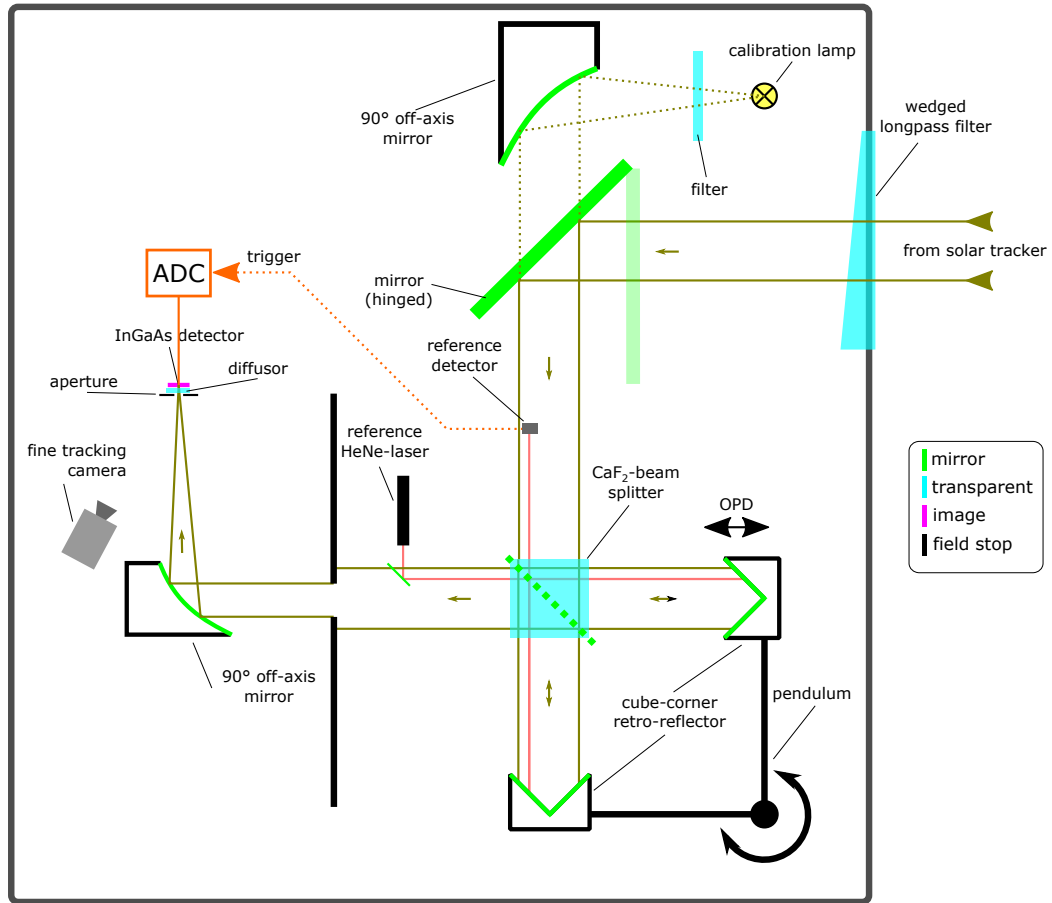


Figure 3.2: The EM27 Fourier Transform spectrometer. The solar light enters the instrument from the right through a wedged window and is split into two beams by the CaF_2 beam splitter. Contrary to the Michelson interferometer, *both* mirrors move and introduce an optical path difference (OPD), that amounts to twice the mirror travel x . The beam exits the cube corner to the left and is focused on the InGaAs-IR-detector. Here, the interference in dependence of the OPD occurs. The Helium-Neon-laser serves as trigger source for the electronics (ADC) to record an interferogram sampling point for each zero-crossing of the HeNe interference intensity. The hinged entrance mirror can toggle the interferometer from external input to the internal calibration lamp.

of approximately $1 \cdot 10^{21}$ molec m^{-2} (HCL) and $2 \cdot 10^{20}$ molec m^{-2} (HF). These two species typically can be measured in volcanic plumes (Butz et al., 2016).

An additional filter mounted in front of the calibration lamp, allows determining the ghost to parent ratio (GPR). As described before, non-equi-distant sampling can cause sampling ghosts. These ghosts appear as an attenuated, shifted spectrum somewhere in the real spectrum. The $GPR := \frac{I_{ghost}(\nu)}{I_{spec}(\nu)}$ can be measured with a narrow spectrum, with spectral intensities only in a certain wavelength range. The filter FB1650-12 by Thorlabs (center wavenumber: 6061 cm^{-1} , FWHM: 44.0 cm^{-1}) provides such a characteristic. The remaining spectral regions should not have any intensity. In presence of ghosts, intensities besides the filter characteristics would be visible. With respect to the retrieval, sampling ghost pose a strong disturbance, since they contain spectral information that can correlate with the retrieved trace gas.

The EM27/SUN is a development in cooperation between KIT and Bruker Optics. It has indicated its long-term stability (Gisi et al., 2012) in measuring atmospheric CO₂ abundances over a four month period. Even strong temperature differences due to free-air measurements in winter as well as summer times, indicated no significant drift in comparison to TCCON measurements. The instrument is portable and operable by a single person and well suited to operate in stationary operation, even in remote regions with low infrastructure. Within this work the EM27 could be operated on board the research vessel RV-Polarstern (see chapter 6) and record the interhemispheric transect of CO₂ and CH₄. Challenging, however was the measurement from a mobile platform such as a car. Here, strong vibrations cause the interferometer to malfunction during movement. In addition the long integration time of approximately 12 s was too long for the strongly varying tracking conditions, even with an enhanced solar tracker version (pers. communication A. Butz).

3.3 DC-fluctuations

A FTS-instrument records the interferogram (IFG) during the integration time. Key assumption to apply the Fourier Transformation is, that during the measurement from OPD_{min} to OPD_{max} the spectral signal remains unchanged. Such a spectral change can be for example the sudden presence of a spectral absorber during the record. For atmospheric conditions, however, this requirement is mostly given, since changes take place slowly. However, this might not be the case by the investigation of a volcanic plume, or other point-like sources, that might have strong variability in trace gas concentration along the line of sight.

In addition the absolute intensity of the spectrum might change due to cloudy conditions or other disturbances. For this reason the interferogram should be recorded in the DC⁶-mode. The correction scheme is described in the following.

Figure 3.3 shows an example spectrum that is affected by DC-fluctuations. In addition the smoothed interferogram is shown. The smoothing here is a 5 times running mean upon $n = 61$ IFG-samples. It is equivalent to

$$I_{s,m}(x) = I_m(x) * box_n(x) \quad (3.14)$$

$box_n(x)$ here indicates a box function that is 0 except for n -samples and $*$ denotes the convolution of the two functions.

From the smoothed interferogram $I_s(x)$ the DC-parameter DC_{par} can be derived using

$$DC_{par} = \frac{|I_s(x)|_{max} - |I_s(x)|_{min}}{|I_s(x)|_{max}}. \quad (3.15)$$

⁶DC stands for direct current contrary to AC (alternate current) record scheme, where $\frac{dI(x)}{dt}$ is recorded instead.

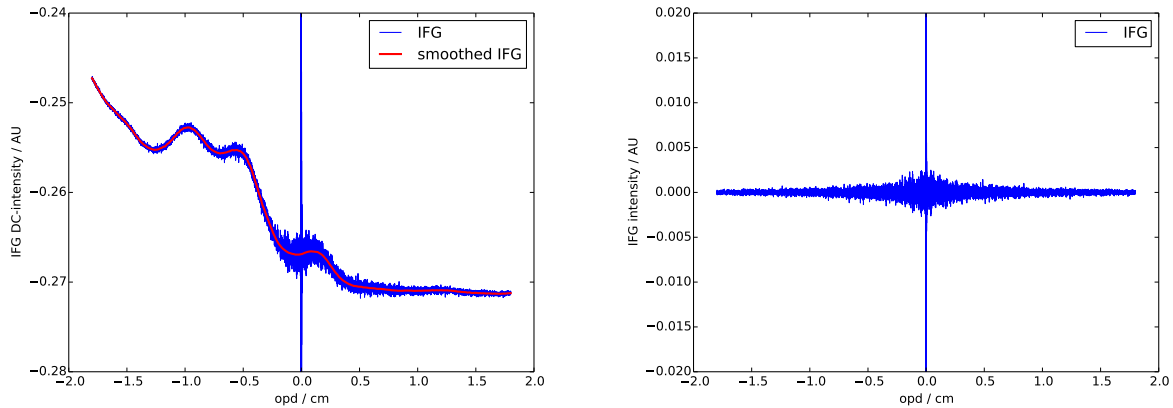


Figure 3.3: Example DC-affected interferogram of the EM27 (left). The center burst at $OPD=0$ exceeds the shown plot by a factor of approximately 1.6. The smoothed interferogram I_s is shown in red. It is used to obtain DC-characteristics as well as for the DC-correction. The corrected interferogram is shown right.

The DC_{par} can be used to characterize and flag DC-affected spectra and discard them from the scientific data set. A value of $DC_{par}=0$ corresponds to a non-DC-affected interferogram, whereas a value of 1 would mean a maximum of the DC-fluctuation. This corresponds to a total loss of intensity in the interferometer during the record. In the course of a ship based campaign (see chapter 6) the DC-threshold of 5% could be found. This empirical threshold selects with good accuracy DC-affected spectra and removes them from the data set. However its capabilities are limited. For instance a small, but high-frequent dc-fluctuation might pass the filter but cannot be corrected properly (according to Equation 3.16) since the smoothed IFG cannot follow this high frequent noise. However, these kind of fluctuations are rare in the stationary or mobile operation on a ship, but might become more frequent at the operation on a car (see Figure 2.5).

As long as the variation in the DC-IFG signal can be followed properly by the smoothed function $I_s(c)$ the dc-correction can be applied as suggested by Gisi (2012):

$$I_c(x) = \left(\frac{I(x)}{I_s(x)} - 1 \right) \cdot E \quad (3.16)$$

Here $E := \langle |I_s(x)| \rangle$ as the mean intensity of the smoothed interferogram. In case of the EM27 record the parameter E ranges from 0 to approximately 0.5 and is proportional to the exposure. The exposure parameter can additionally be used to discard unexposed records from the data set. A threshold of 0.05 (equivalent to approximately 10% of full detector exposure) can empirically be found to discard the weakly exposed spectra from the data set.

These two corrections are applied automatically in a self-programmed routine that will be described in section 3.5.

3.4 Quality filters

Various effects disturb the retrieved final total column mixing ratio of XCO_2 and XCH_4 . Goal is to define quality filters that remove the affected spectra and discard them as soon as possible from the processing chain in order to lower the computational effort. Basically three filters can be applied that will be described in the following. Underlying data-set is the Polarstern record as described in section 6.1. The well mixed oceanic air is little influenced by local sources such as power-plants forests swamps or others, and can be used to constrain the filter-threshold. Outliers are more likely measurement artifacts rather than a real signal.

The first applicable filter is the exposure filter. Since the EM27/SUN records the spectra regardless the illumination conditions, cloudy scenes or other shadowing effects have to be removed from the data set. If the maximum intensity (IFG_{max}) is lower than the threshold T_{exp} then the spectrum will be discarded. This threshold was set to 5% of the maximum possible IFG-value. In addition over-exposure could prevented and would be filtered out if 80% were exceeded. Since overexposure did not occur, this filter was never active. Note, that previous EM27/SUN instruments recorded negative values of the IFG. Because of that the absolute value is taken instead.

The second applied filter is the DC-filter as described in the previous section. Here the filter threshold of $T_{DC} = 0.05$ was found to give the optimal balance between data yield and data quality.

The two previous filters are applicable before the computationally costly retrieval procedure. As a post-processing step a third quality criteria can be used: The O_2 filter. Since the oxygen total column typically is retrieved as well, and the relative change in atmospheric O_2 concentration is rather constant this record can serve as a reference. The partial pressure of the oxygen can be calculated:

$$p_{gas} = \frac{N_{gas}M_{gas}g(lat)}{N_a} \quad (3.17)$$

$N_{gas} = N_{O_2}$ denotes the number of O_2 molecules, $M_{gas} = M_{O_2}$ the molar mass, $g(lat)$ is the latitudinal dependent gravitational acceleration and N_a the Avogadro constant.

Assuming a constant *mass-mixing ratio* of $C_{ref,O_2} = 0.23135$ the total pressure can be calculated including the contribution of H_2O and can be referenced to the measured pressure p_{meas} at station height:

$$R = \frac{p_{O_2}/C_{ref,O_2} + p_{H_2O}}{p_{meas}} \quad (3.18)$$

Ratio R can be used as a sanity check on global retrieval parameters such as solar zenith angle, timing or assumed field of view (FOV). Deviations from unity indicate that these parameters might be incorrect and filtered out.

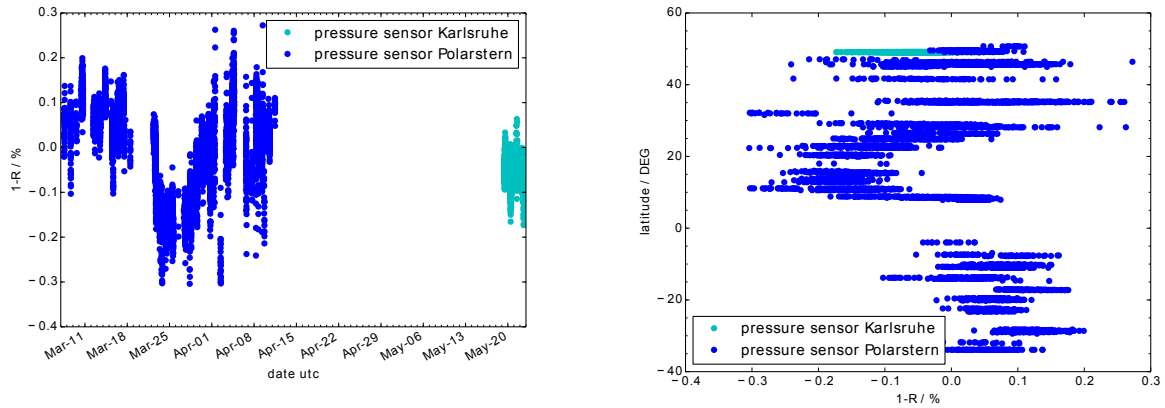


Figure 3.4: RV *Polarstern* data (see section 6.1) of the ratio $1 - R$ (see Equation 3.18) in temporal dependence (left) and latitudinal dependence (right). Note the systematic pattern at approximately 10-25 ° North. The source of this deviation remains unclear. Comparisons with modeled CO₂ concentrations confirmed this systematic deviation (Frédéric Chevallier, personal communication).

Figure 3.5 shows the effects of the O₂ and DC-Filter. It can be seen, that they filter for individual error sources, since only a few data points are filtered by both filters.

With the Polarstern-data-set a threshold of $T_{O_2} = 0.003$ could be found to be suitable. Note, that all measured quantities (O₂, H₂O and p_{meas}) introduce measurement errors, that might disturb the filter approach. In fact, a systematic change in the ratio can be observed with unknown source. Parameters like the ghost-to-parent ratio (GPR) (see section 3.2) are not suspicious. A likely candidate might be interference with water vapor or the H₂O -a-priori profile. Email communications with Frederic Chevallier⁷ revealed systematic model-measurement deviations in this particular region. This hints to re-investigate the approach on referencing by the O₂ column for the XCO₂. It might be possible, that rationing by oxygen column introduces more systematic errors, than it corrects for.

3.5 Spectral calibration - CALPY-mobile

To obtain the trace gas abundances of the EM27 a spectral retrieval has to be performed as described in chapter 5. For this purpose a set of auxiliary data has to be provided for the retrieval. So far the retrieval is only performed on stationary instruments, which did not change its position in means of latitude and longitude. With this change in position a change in atmospheric state comes along that has to be accounted for in the retrieval. Additionally the calculation of the solar zenith angle θ changes with the position. The required pointing accuracy for the solar tracker of 0.05° (see chapter 2) holds as well for the calculation of the solar zenith angle in the retrieval to ensure a retrieval error below 0.1%. The calculation of the solar zenith angle can exceed the 0.05° requirement by deviations of the station from 5 km onwards. This implies the need to account for the moving position in

⁷Frédéric CHEVALLIER, Lab. des Sciences du Climat et de l'Environnement, France.

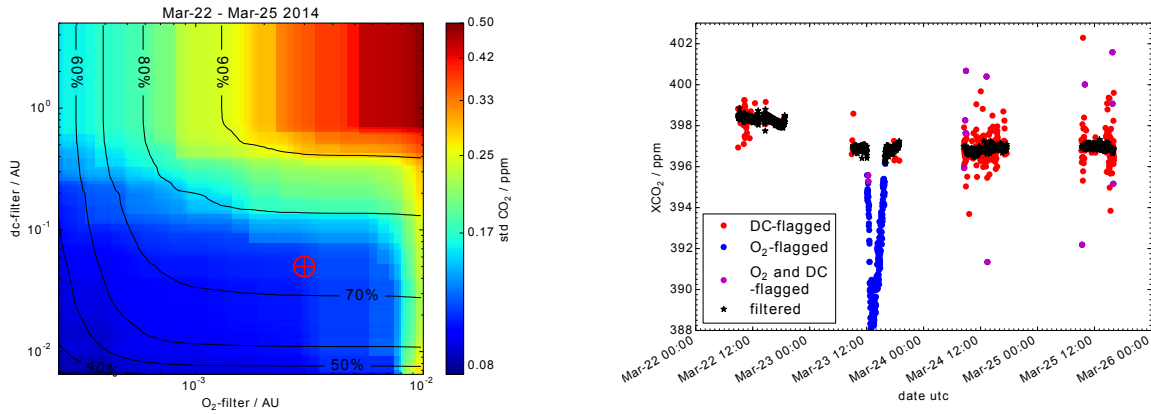


Figure 3.5: A sub set of the Polarstern data-set of four representative days. Left figure shows the logarithmic color-coded standard deviation in the XCO₂ record in dependence on the O₂ filter threshold (T_{O_2} , abscissa) and the DC-filter threshold (T_{DC} , ordinate). In addition the data-yield is overlaid (black lines). The right figure shows the effect of the individual filters in the time series. It can be seen, that they filter for different effects since they have only a few data points in common.

the retrieval. In addition the spectral calibration of the spectrometer’s output has to be performed that ideally applies quality filters as well as corrections to the data set.

Preferable spectral input files for the PROFIT retrieval programme executable is a binary format with prior ASCII-header. This requires several steps in the pre-processing involving multiple programmes: The spectral records in the OPUS⁸-format were exported with a special script (CalA.mtx) to a ASCII data-point table. It required the previous creation of the required pressure-temperature profiles (pT-files). This in turn was done by an email-request to the Goddard-automailer⁹, and the creation of these files with an external program. After the first step, the next step (CalB.mtx) creates the .BIN-files that serve as an input for PROFFIT.

In order to simplify this data-processing the Python-Based script CALPY¹⁰ was developed. The initial version of CALPY had been expanded heavily within this work to CALPY-mobile. The pre-processing includes automated download of the pT-profiles from goddard-automailer and preparing the pT-files for the use in PROFFIT. Additionally the recorded spectra in the OPUS-format are loaded, DC-corrected (if desired) and exported together with the desired additional data (such as solar zenith angle etc.) into the PROFFIT readable .BIN format. In addition multiple intermediate processing data are stored into an ASCII log-file, which can be used for the post-processing. Optionally CALPY-mobile outputs the a-priori-profiles in the PROFFIT-format from model-ncdf-data files. Figure 3.6 shows the input-output scheme of calpy-mobile. Minimum requirement (light green) is the input-configuration file, external data such as ground pressure and temperature values and the spectra in the

⁸FTS-recording software by Bruker, <https://www.bruker.com/products/infrared-near-infrared-and-raman-spectroscopy/opus-spectroscopy-software.html> (last accessed: 19.05.2016)

⁹Provided by NASA: http://acdb-ext.gsfc.nasa.gov/Data_services/automailer/

¹⁰Involved: Frank Hase, and Michael Gisi

OPUS-format. The output then directly can be processed using BAT-SU.exe and then BAT-EX.exe (or BAT-EXPP.exe) to start the PROFFIT job.

CALPY-mobile could be advanced to replace the BAT-SU and the BAT-EX in further versions in order to simplify the work flow further.

In summary, intensity fluctuations during the sampling period of the Fourier Transform Spectrometer can be corrected automatically with the DC-correction. In addition this correction can be used to filter for strongly affected measurements in order to exclude them before the computationally costly retrieval starts. The threshold of $DC_{par} > 0.05$ was found to discard affected spectra properly. The self-programmed python-software package “CALPY-mobile” performs the correction and discards measurements according to the threshold. In addition this software collects auxiliary data such as meteorological profiles or trace gas profile a-priories from model data in preparation for the retrieval with PROFFIT.

In addition the measured ground pressure can serve as an additional filter criterion with comparisons to the measured oxygen total column, that can assumed to be constant. A filter threshold of $R > 0.003$ removes false measurements from the data set reliable after the retrieval process.

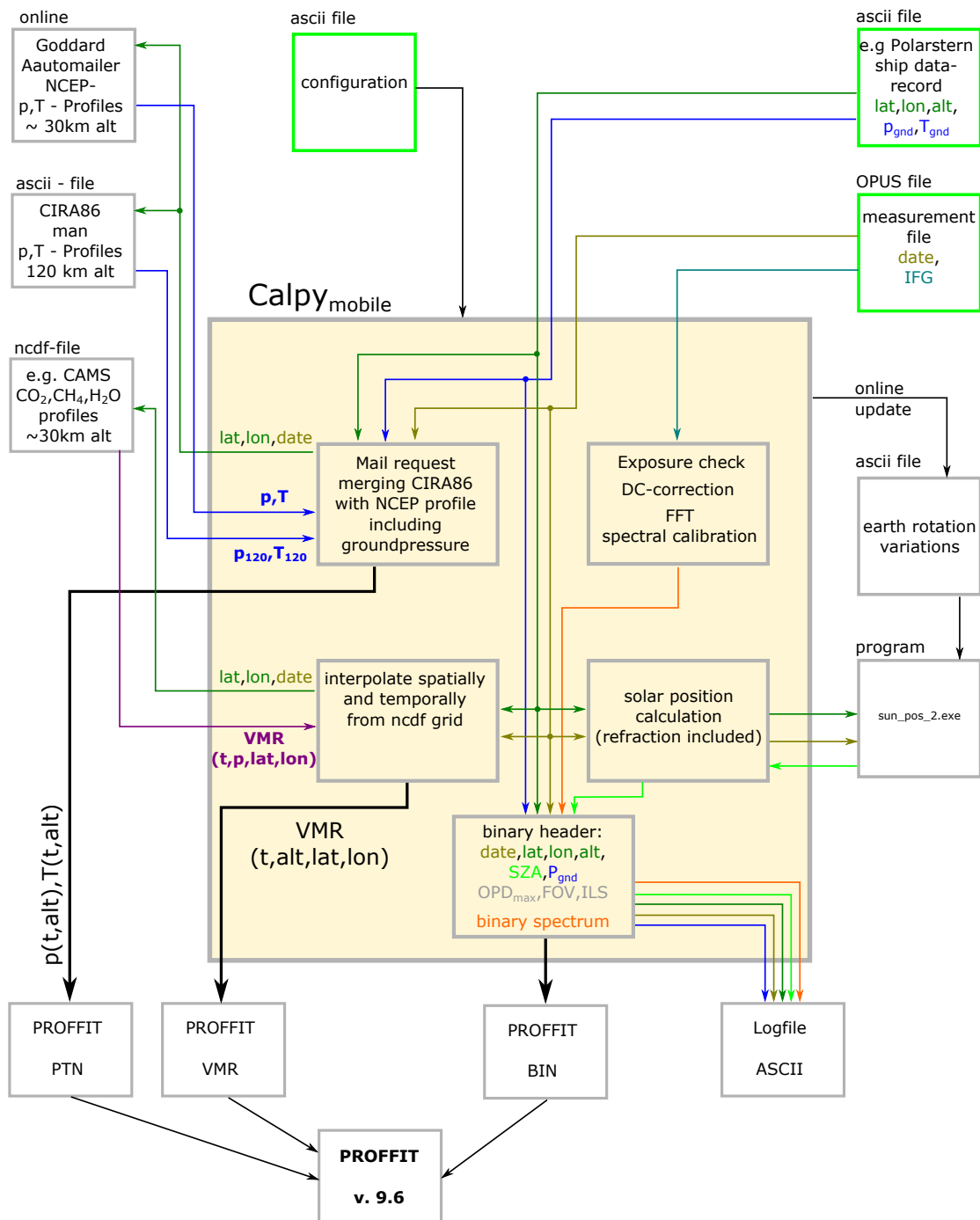


Figure 3.6: Only three inputs are required in CALPY-mobile (light green). The output is prepared such, that the PROFFIT job can started from BAT-SU.exe onwards. Optional input might be profile data from model sources as a retrieval a-priori.

4 Grating spectrometer for mobile applications

High resolution FTS NIR spectrometers, such as used by the TCCON network (see subsection 1.2.3) are well established instruments for accurate trace gas measurements. The EM27/SUN (see chapter 3), as a moderate-resolution FTS with a resolving power of approximately 12,000 could show already great performance under stationary conditions and even on board the research vessel Polarstern in direct sunlight spectroscopy (see chapter 6). However, this instrument is less agile due to its moving parts. On strongly vibrating platforms (e.g. car) the interferometer regularly fails (personal communication A.Butz). Flexibility is required to infer the source strength of a localized source of CO₂ and CH₄ as it can be performed with traverses (passing by a source). To drive mobile remote sensing techniques towards more flexibility the development of a NIR grating spectrometer will be described in the following.

This chapter is structured as follows: Theoretical basics of NIR-Grating spectrometers with focus on a portable and robust instrument will be given first together with the requirements the instrument should comply with. Then, the basic setup of grating spectrometers is described, including the required optical and mechanical parts. An inter comparison of three grating setups, including a highly dispersive “immersed grating” will be presented. A brief sketch on the data acquisition and evaluation scheme will be given, before the finally implemented setup of the grating spectrometer will be described in detail. A considerable part of this section discusses detector characteristics, such as non-linearity and etalon-interference, and approaches to correct them. The section closes with the description of the data processing step from a raw record to the calibrated spectrum as well as a discussion on future instrumental improvements.

The idea of using a NIR-Grating spectrometer for mobile atmospheric measurements is to take advantage of the mechanical robustness of such instruments. Grating spectrometers can be designed without moving parts. If moving parts (e.g. a rotating grating) are chosen, their movement is typically non-critical and deviations can be corrected. This allows constructing a robust campaign instrument, which can cope with vibrations or strong accelerations. Downside, compared to FTS instruments, is, that usually only the prior selected spectral windows are available, rather than the entire spectral range the detector can resolve. This

comes along with integration times (the time for a single record) that are up to 3 orders of magnitude shorter than the FTS - a valuable feature under strongly variable conditions.

The requirements for the instrument are a spectral resolving power $R := \frac{\lambda}{\Delta\lambda} = \frac{\nu}{\Delta\nu}$ of approximately 6400 or better. Here, λ represents the wavelength and $\Delta\lambda$ the minimal distance of two resolvable intensities. This resolving power corresponds to a spectral resolution of $\Delta\lambda = 0.25$ nm at 1600 nm. The spectral windows should cover the absorption range of carbon dioxide (CO₂) methane and (CH₄) as well as the spectral absorption region of oxygen (O₂) as reference (see Table 1.1).

One person should be able to move and operate this instrument and poses the requirement with respect to the physical dimensions and weight. Power consumption should be suitable for field-deployment.

4.1 Optical setup of grating spectrometers

The task of a spectrometer is to measure the intensity within a specific wavelength range. This can be performed by the projection (lens or mirror) of a defined input (e.g. a slit aperture) on a detector (e.g. CCD camera), where the image position on the detector is dependent on the wavelength. Central piece of such an instrument is the dispersing element (e.g. prism or grating), which introduces a wavelength dependent angular dispersion which, in turn, alters the position on the detector image. These dispersing elements typically need a plane wave front. This requires two imaging components (e.g. lens or mirror). Here, the first imaging element forms a plane wave front on the dispersing element, as desired, and the second imaging element focuses the image on the detector.

The following chapter gives a brief overview of the most important optical features. The content is summarized from Hecht (2014), James (2007) and Demtröder (2013).

4.2 Diffracting elements

Two optical elements can be used to perform a wavelength depended deflection of light to be used in spectrometers: Gratings and prisms.

Prisms are dispersing elements that make use of the *change* in refractive index $\frac{dn(\lambda)}{d\lambda}$. Under specific incident angle θ_{in} on a surface with the refractive index $n(\lambda)$ Snell's law gives the relation to the outgoing beam θ_{out} :

$$\theta_{out}(\lambda) = \arcsin\left(\frac{n_{in}(\lambda)}{n_{out}(\lambda)} \sin(\theta_{in})\right) \quad (4.1)$$

Typical values of $\frac{dn(\lambda)_{NBK7}}{d\lambda}$ range in the order of $0.12-2.9 \cdot 10^{-4} \text{ nm}^{-1}$ for a widely used NBK7-glass. This value increases drastically towards the shorter wavelength range of 400 nm and below. The dispersion relation is typically low in the IR-region, so for IR applications

and a small instrument the use of a prism is less suitable using most of the conventional glasses.

Gratings, however, are based on an interference condition depending on the angle θ_{in} . Since a multiple of the specific wavelength gives the same interference condition, the grating equation might have multiple solutions:

$$\theta_{out}(\lambda) = \arcsin(G m n \lambda - \sin(\theta_{in})) \quad (4.2)$$

Here, $G = 1/s$ is the grating constant and the inverse of the periodic spacing s . m denotes the diffraction order, that is a whole number and might also have negative values. n stands for the refractive index of the medium, the grating is embedded. For conventional gratings, $n = n_{air} \approx 1$ applies. Typical values of G range from a few ten to 3600 lines mm^{-1} or more.

Both grating and prism can disperse different wavelengths separated by $\Delta\lambda$ under different angles $\Delta\theta$. These angles can be projected into the image plane with a lens (or mirror) of the focal length f . This translates the angular dispersion into a spatial dispersion $\Delta x = f \tan(\Delta\theta) \approx f \Delta\theta$ in the image plane. A detector pixel in the image plane integrates the intensity along the pixel width w_{pix} . An individual pixel in the image plane of a grating instrument samples the spectral width $\Delta\lambda$ according to

$$\Delta\lambda_{pix}|_{\lambda} = \frac{w_{pix}}{f \frac{d\theta_{out}}{d\lambda}|_{\lambda}} \quad (4.3)$$

$$= \frac{w_{pix} \sqrt{1 - (G m n \lambda - \sin(\theta_{in}))^2}}{f G m n}. \quad (4.4)$$

For a high resolution instrument a small $\Delta\lambda_{pix}$ is desired. Note, that typically the pixel width w has a certain limit that defines the sampling width $\Delta\lambda$. As a rule of thumb $\Delta\lambda_{pix} < 5\Delta\lambda_{optic}$ should hold to ensure a proper sampling of the spectrum. In order to construct a small instrument, a small focal length f is necessary, since large focal lengths need space. According to Equation 4.4, this has to be compensated by a high angular dispersion $\frac{d\theta_{out}}{d\lambda}$.

In order to increase the angular dispersion, the grating order m can be increased such as it is performed with Échelle gratings. This can be further enhanced by the combination of a grating with a prism. Such a “grism” or “immersed grating” is highly dispersive and allows to construct small instruments such as it is desired for satellite applications (van Amerongen et al., 2010; Ebizuka et al., 2002, 1998). The use of immersed gratings is further investigated in subsection 4.3.1.

Additional to the resolution and sampling related parameters, instrumental line shape (ILS) is of major importance for the retrieval (see section 5.2). Here, the optical components

introduce numerous possible imaging errors that cause a point-like source object not to be imaged like a point. These imaging errors can be diffraction on apertures, chromatic aberration, spherical aberration, coma, astigmatism or simply de-focus, which decrease the performance of the instrument's imaging properties. Deviations from the optical axis typically increase these aberrations. Thus, lowering the effective aperture of an optical system typically decreases these image deviations drastically, with the drawback of less intensity on the detector. The f-number defined as $f_{\#} := f/d$ is an indicator for how much light passes the system. Here, higher f-numbers stand better image properties, but less light on the detector and longer integration times. Additionally, the off-axis-angles introduce image aberrations. These angles typically occur with the use of imaging mirrors in an optical system instead of lenses. The source (the element in front of the mirror, for instance a light bulb) and the target component (the element after the mirror, e.g. detector) cannot be at the same physical location and thus mirrors always introduce off axis angles. Off-axis effects might cancel out partly, if two mirrors with contrary off-axis angles are used¹. In order to eliminate chromatic aberrations and additional surface reflexes of lenses, imaging mirrors present a valuable choice within the framework of optical systems.

4.3 Design concepts for a NIR-grating spectrometer

In designing a grating spectrometer, numerous parameters have to be taken into account which are depicted by James (2007) and summarized in the following. The choice to of the grating, focal length, aperture, entrance slit and detector as well as the breadboard and the use of field stops can be implemented in various ways. Additionally practical aspects such as availability of optical components, thermal stability, force free mounting of the optical elements or damage prevention due to user-interaction, focus adjustments and many other aspects have to be taken into account. Here, just a very brief summary of the most important aspects and design considerations will be given. First a suitable mounting configuration will be described. Then the technical aspects such as the focal length or the use of an immersed grating compared to conventional gratings will be discussed. The section closes with the description of the final instrument.

Grating spectrometers can be implemented in multiple ways. Figure 4.1 gives a selection of mounting configurations. The Ebert-Fastie-mounting uses just one mirror for collimation and refocus. Main disadvantage here is, that it is difficult to adjust and stray light cannot be controlled well since most of the beams overlap. The Littrow-Mounting uses just one mirror as well with the condition that the entrance angle on the grating equals the exit angle $\theta_{out} = \theta_{in}$. This results into optimal grating efficiency but only allows very small entrance and exit apertures that can be used in monochromators. The Czerny-Turner-Mounting is the most flexible mounting configuration that allows adjusting two mirrors. Separated

¹Telescopes are a good example: They have a large-diameter primary mirror and a smaller diameter secondary mirror (e.g. Newtonian, Cassegrain or Gregorian Telescope). However off-axis angles occur as well but average to a symmetric distortion

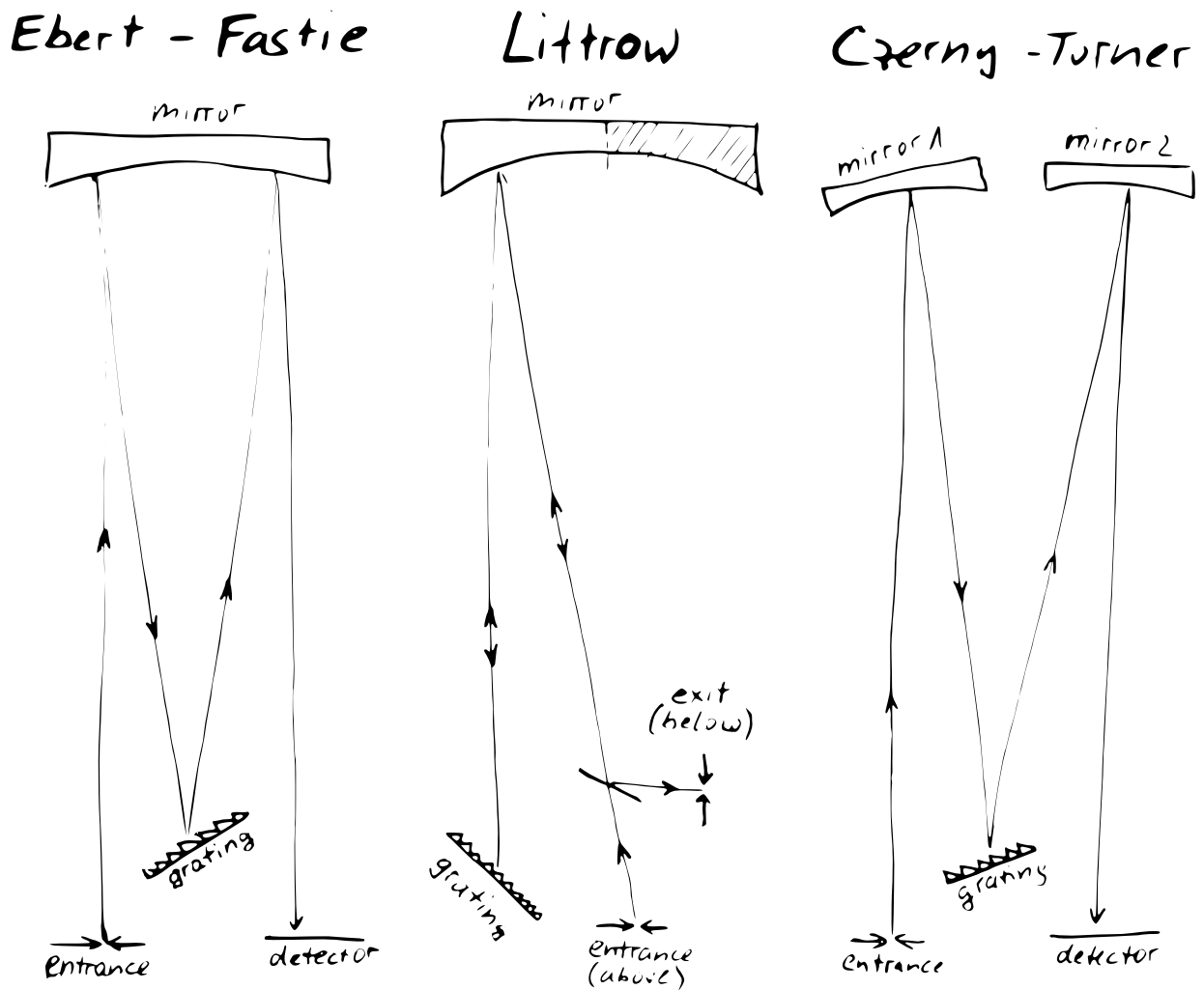


Figure 4.1: A selection of grating mounting configurations. Ebert-Fastie (left), Littrow-mounting (middle) with entrance and exit aperture above and below principle plane, and the widely used Czerny-Turner-configuration (right).

beams allow introducing stray light suppressing apertures. In addition this configuration is flexible enough to integrate a broad detector instead of a small exit aperture.

In order to find the initial setup design for the grating spectrometer, a self-programmed MatLab™ routine was used, to simulate a Czerny-Turner spectrograph with geometric ray optics that gives an estimate on resolution, aberrations and physical dimensions of the instrument. The specifications of the optical elements such as focal length, aperture, ruling of the grating, slit width and many others can be tried out and simulated in real-time. First possible setups were simulated and tested on a breadboard in the second step. Most important here was the question of the focal length to use. Mirrors with the focal length of 300 and 500 mm were available “of the shelf”. Three setups were simulated and tested in a breadboard setup: Two conventional Czerny-Turner setups with $f=300$ mm and $f=500$ mm focal length. The third design is a setup with an immersed silicon grating. Before the results will be discussed, the immersed grating will be discussed in more detail.

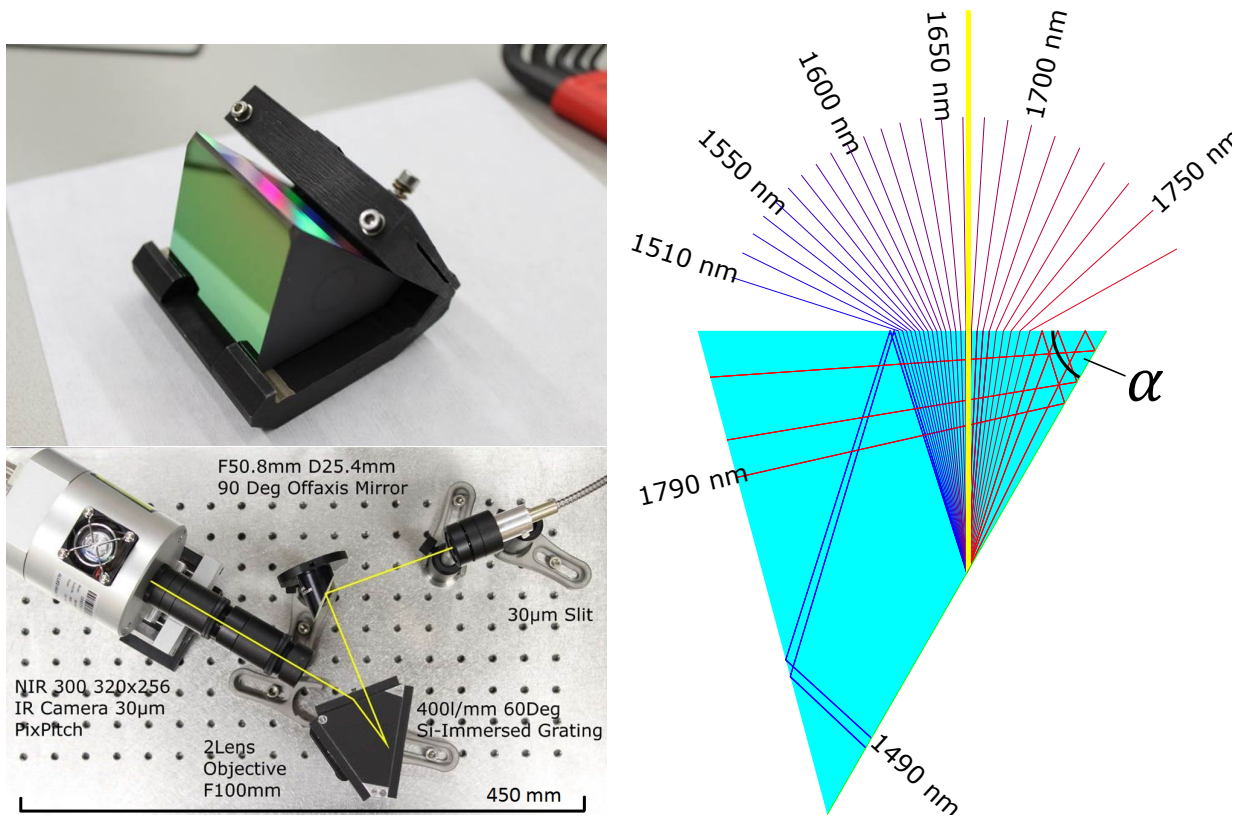


Figure 4.2: The used immersed grating (top left) and the used breadboard setup (bottom left). The fiber coupling is in the upper right section. A 90° imaging mirror collimates the light into the immersed grating. Since there is little space available lenses instead of mirrors image the spectral information on the detector (left). On the right hand side is a ray-simulation of silicon grating as it was available - the angle of the right corner is $\alpha = 60^\circ$. Note that the oxygen-spectral region (1250-1285 nm) does not exit the prism surface but is reflected by a total reflection.

4.3.1 Immersed grating concept

Equation 4.3 depicts that a high resolution instrument can be implemented by increasing the focal length or the angular dispersion of the dispersing element (grating or prism). Increasing the focal length, however, typically results into a larger instrument. Thus increasing the angular dispersion can result in a small and high resolution instrument. Crystalline silicon has a refractive index in the order of $n_{Si} \approx 3.4$ (Li, 1980) whereas the refractive index of a typical glass $n_{BK7} \approx 1.5$ in the near infrared wavelength domain. According to Equation 4.3 the instruments resolution can be improved drastically using silicon as immersed substrate. The overall performance regarding resolving power or free spectral range of grating spectrometers increases for short wavelength regimes (i.e. in the UV region). An immersed grating can be pictured as a grating inside an optical medium with the refractive index n . Here, inside this medium the vacuum wavelength is shortened by the refractive index $\lambda_n = \lambda_{vac}/n$ and thus enhances the grating performance. Note, that this only applies for configurations where the grating surface and the immersed surface are not parallel to each other but under the angle $\alpha \neq 0$.

The immersed grating was a loan from SRON² as a development sample (ID# 11-10-13) (van Amerongen et al., 2010). The design wavelength is 2305-2385 nm with a prism angle of $\alpha = 60.0^\circ$ and a groove density of 4001 mm^{-1} for the use in the $m = -6$ th order. The entrance/exit face has a specially designed anti reflective coating with a reflectivity lower than 0.5 % for the designed wavelength range. The physical dimensions are $50 \times 60 \times 43 \text{ mm}^3$ with a weight of approximately 150 g.

Figure 4.2 shows the simulation of a silicon immersed grating as is was available. The relevant rays from 1490 - 1790 nm are shown. Both wavelength ranges for CO_2 (1590-1620 nm) and CH_4 (1630-1680 nm) exit the prism surface after diffraction. Challenging might be the position of focusing elements for the spectral range of CH_4 , since the angles align with entrance beam. A change in the angle of incidence (rotating the immersed grating) can be an option but this might result into additional stray light in the spectrometer. Further, the desired O_2 absorption range does not exit the prism, so this particular immersed grating is not suited to measure the target gas oxygen as reference gas. These total reflections can reach the detector unintended and produce stray light. If the stray light contains spectral information e.g. from a different wavelength range that overlaps the target spectrum, the spectral retrieval might be disturbed significantly. For this reason the unused left face of the prism is designed such, that its internal reflective properties are low to suppress such stray light sources.

An additional source of stray light is the entrance facet itself. It has an anti-reflective coating optimized for the design wavelength of 2305-2385 nm with a nominal reflectivity of 0.5 % or less. This coating has a different reflectivity in the near infrared wavelength range of 1000-1650 nm. To estimate the reflectivity of the immersed grating entrance surface, a reflection of a homogenous illuminated screen is imaged on the NIR-camera. This reflection can be set into relation to a reflection on an aluminum coated mirror under the same conditions. Using this approach the reflectivity of the immersed grating coating for the wavelength range from 1000-1650 nm can be estimated to $(13.8 \pm 2.5) \%$. Compared to the low reflectivity of less than 0.5 % at design wavelength, a high amount of stray light from direct reflections is to be expected.

The refractive index of silicon is strongly temperature dependent. According to Li (1980) $dn/dT|_{\lambda=1600 \text{ nm}, T=293 \text{ K}} \approx 1.7 \cdot 10^{-4} \text{ K}^{-1}$ which would translate to a relative change in the pixel sampling $\delta_{pix}|_{\lambda}$ of approximately $1 \cdot 10^{-4} \text{ K}^{-1}$ and will affect the ILS as well as spectral shift.

Simulations show, that an immersed grating can be designed such, that it suites the needs for measuring CO_2 , CH_4 and O_2 as reference. Figure 4.3 depicts the simulation of a silicon immersed grating for the desired wavelength ranges. The chosen prism angle is $\alpha = 44.0^\circ$ at a groove density of 4001 mm^{-1} in the use of $m = -8$ th order. It is worth mentioning, that the blaze-angle of the grooves that enhance the intensities for specific wavelength regions might need to be adopted to this new immersed grating design. A spectrometer using this

²SRON Netherlands Institute for Space Research (Netherlands)

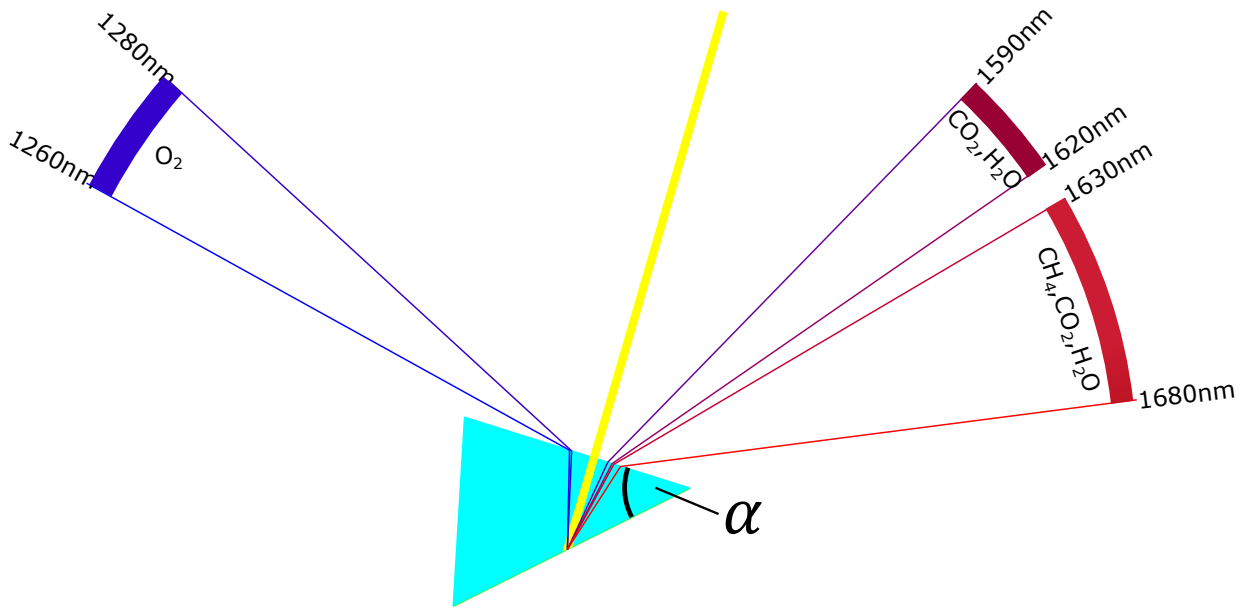


Figure 4.3: Simulation of an immersed grating designed specifically for the measurement of CO₂, CH₄ and O₂. The prism angle $\alpha = 44.0^\circ$ under the order $m = -8$ th.

designed immersed grating could be implemented as a static instrument that uses three detectors under the specific angles of the trace gases. Instead of rotating the (immersed) grating this approach can avoid the use of moving components.

4.3.2 Inter-comparison of three grating setups

As mentioned earlier, three setups were tested in theory and implemented as breadboard setup: Two conventional grating Czerny-Turner setups with $f = 300$ mm and $f = 500$ mm and the immersed grating as it was available. Table 4.1 summarizes the key parameters of the implementation. The used detector differs for the $f = 300$ mm and the immersed setup from the $f = 500$ mm setup. The initial 2D detector (NIR300PGE by VDS Vosskühler) has an additional glass window in front of the detector, which produces additional interference structures (see section 4.6). Further not all detector corrections could be applied to the NIR300 detector (e.g. non-linearity) since the laborious characterization of the detector was only performed for the detector used in the final setup ($f = 500$ mm).

Figure 4.4 shows the 2D records for each setup. All of them used the NIR-2D pixel array as detector. So besides the spectral domain that is resolved in one direction (abscissa) an additional domain (ordinate) can be used to obtain spatial information or as a repeated measurement. The coarse spectral calibration on the abscissa is only for reference purposes. Each record has non-illuminated areas on the detector (dark blue colors). These non-illuminated areas can be used as stray-light estimate or to check on variations in the detector dark-signal. The vertical width of the illuminated area (reddish colors) depends on the external field of view and the height of the entrance slit. The slit height of the immersed grating setup and the $f = 300$ mm setup is 3.0 mm, contrary to 7.5 mm for the $f = 500$ mm setup.

parameter	immersed	$f = 300$ mm	$f = 500$ mm	unit
focal length f	100	304.8	508.0	–
grating G	400 (immersed)	600	950	l mm^{-1}
entrance slit	30	30	10	μm
slit height	3.0	3.0	7.5	mm
aperture diameter d	25.4	20.3	25.4	mm
numerical aperture	3.9	15.0	20.0	–
design wavelength	2305-2385	1606	1606	nm
design resolution	0.04	0.14	0.04	nm
resolving power	40,000	11,000	40,000	–
detector	NIR300	NIR300	Goldeye	–
coupling	fiber	direct	direct	–
dimensions L	350	550	850	mm
dimensions W	300	370	370	mm

Table 4.1: Key parameters of the three tested spectrometer setups.

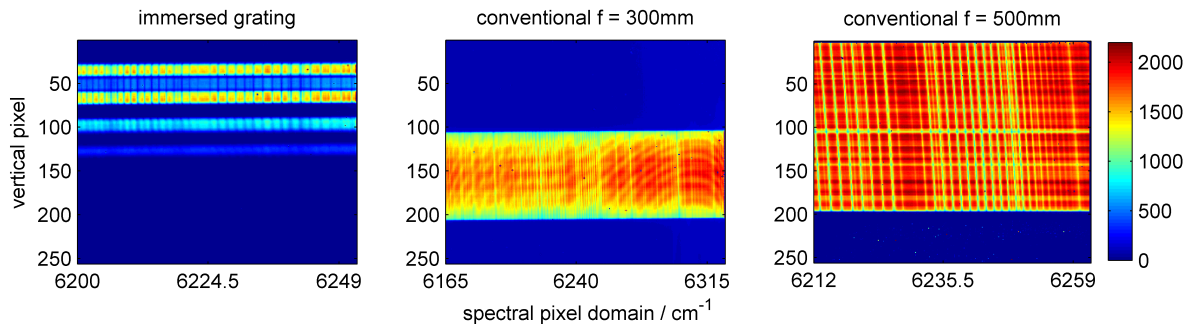


Figure 4.4: 2D-raw atmospheric spectra in the range of CO_2 absorption for the different setups in the range of $6200\text{-}6260\text{ cm}^{-1}$. Color coded is the detector intensity in arbitrary units (AU). The conventional grating with $f = 300$ mm focal length (left) immersed grating (middle) and the conventional $f = 500$ mm setup. The conventional setups are directly coupled into the entrance aperture, whereas the immersed grating (left) is coupled with a 1×7 cross-section converting fiber. All available corrections are applied i.e. background correction.

The illuminated areas show the spectral information along the abscissa. Clearly visible is the broadband continuum intensity - basically the solar black body spectrum. Additionally absorption features of atmospheric gases lower the transmission intensities in specific wavelength regions represented by greenish-blueish colors. These absorption features cause the vertically stripe-shaped pattern that can be seen best for the $f = 500$ mm setup (right). The pattern appears slightly tilted (right, middle) caused by the entrance slit that is gently tilted towards the vertical pixel array for the conventional setups. This enables up-sampling since each horizontal, spectral row is sampled with slightly shifted pixel grids (see. section 4.7).

A very prominent feature is visible especially for the $f = 300$ mm setup: A gently varying reddish pattern that overlays the spectral absorption features. This Fabry-Perot-Etalon, probably caused by a glass-window in front of the detector array, is a strongly interfering feature for the spectral retrieval (see section 4.6). This feature could be removed partly

in the final $f = 500$ mm setup (right) and is not directly visible here. Further some defective pixels are scattered over the detector plane, which cause minor problems after characterization.

To obtain the calibrated spectrum from the 2D raw record some processing steps are needed as described in subsection 4.5.2. All the spectra are BG-corrected (see subsection 4.6.1). For the $f = 500$ mm setup additionally non-linearity and etalon correction is applied since this correction was only available for this setup. Figure 4.5 shows the calibrated and up sampled results for the three setups. The top panel gives an overview of the spectral width that the implemented spectrometers can cover without rotating the grating. The lowest resolution instrument gives the largest spectral coverage (blue). The immersed grating setup as well as the $f = 500$ mm setup (red, magenta) show very similar spectral coverage as they have similar resolution. In the lower left the physical size of the setups is shown in scale to each other.

The lower panels show a zoom into an arbitrary spectral region for each setup. Here, the high resolution TCCON reference spectrum is plotted as reference in the adapted resolution. The immersed setup shows compared to the $f = 300$ mm setup a relative high resolution. This is especially impressive if the size of the instrument is taken into account. Unfortunately up-sampling was not possible since the entrance slit was not tilted towards the vertical pixel domain for the sake of a simpler evaluation in this early stage of the thesis. The $f = 300$ mm setup (middle) shows a rather moderate resolution. Additionally as already seen before in the 2D records the strong interference pattern progresses into the calibrated spectrum and forms a wavy structure. It is to be expected, that this interference will disturb trace gas retrieval. The $f = 500$ mm setup (right) is the one with the best developed evaluation scheme. The spectral resolution is very similar to the resolution of the immersed grating setup but is approximately three times larger in its physical dimensions.

Each of the three setups has their pros and cons. Even though the immersed grating showed excellent results regarding the spectral resolution in relation to the physical size of the instrument, the disadvantages and unknown issues were too predominant. The prevailing downside of the immersed grating as it was designed that it is not capable to measure oxygen as reference. In addition issues regarding the stray light from the highly reflective entrance facet could pose additional challenges. Further thermal drift of the silicon refractive index does not align with the call for a robust instrument that can be operated under harsh environmental conditions. The remaining question to implement the $f = 300$ mm or $f = 500$ mm of the conventional grating setups was decided by the spectral resolution properties. As shown in section 5.2 the spectral resolving power of approximately 12,000 is desired to obtain CO₂ abundances in a high accuracy. The $f = 300$ mm setup is with a resolving power of 11,000 on the edge of this criterion. However the optimal focal length might be in the range of approximately 350-400 mm. Since mirrors of this

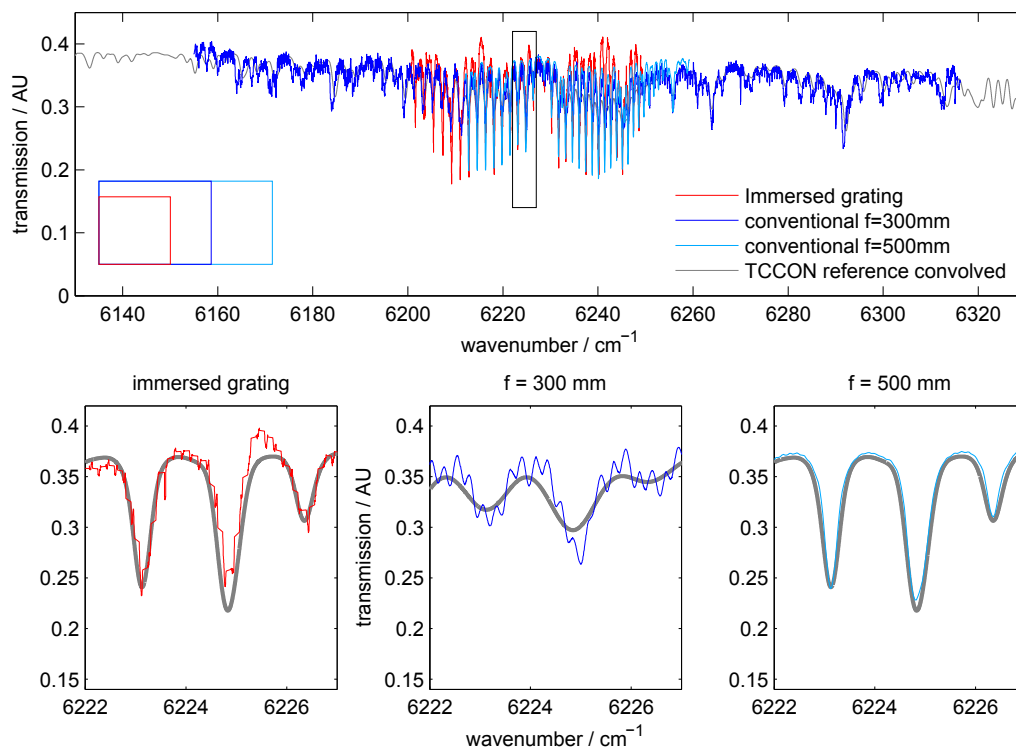


Figure 4.5: Up-sampled and calibrated spectra for the three setups (top panel). Additionally the approximate instruments size is depicted in the lower left of the upper panel. A zoomed spectral region is shown in the lower panels for each setup with the TCCON convolved high resolution spectrum as reference. Note that the data-processing steps for the immersed grating (left) and the $f=300$ mm setup (middle) was still not well elaborated, so these spectra suffer from sampling issues.

focal length are not available in the standard assortment of optic components suppliers the 500 mm focal length setup was the finally implemented one.

In the following section the properties of the $f = 500$ mm setup will be described in detail.

4.4 Ground based grating NIR spectrometer

Based on three test setups of two conventional grating instruments and an immersed grating setup a conventional Czerny-Turner grating spectrometer with $f = 500$ mm focal length was implemented in a campaign GRC-instrument. Here, GRC stands for “Ground RemoTeC³”.

Figure 4.7 shows the linear optical setup of the implemented GRC-instrument. The optical elements are in scale to each other and for illustrative purposes magnified by a factor of 10 compared to their linear positions. In the following the light path through this setup is described as it travels from left to right.

³RemoTeC stands for Remote Sensing of Greenhouse Gases for Carbon Cycle Modeling and is the name of the DFG-funded Emmy Noether Nachwuchsgruppe by André Butz

The solar light beam enters from left and is feed with the angular variable azimuth and elevation mirrors into the aperture lens (APTLens). This lens focuses the 4.6 mm diameter solar image on the round 3 mm entrance aperture (APT). Here, the instruments external field of view is defined that amounts to 3.019 mrad. The fine-tracking camera observes this image and provides optical feedback for the tracking routine (see chapter 2). The SLTLens illuminates the slit aperture (SLT) and projects a solar image on the grating. The image properties are chosen such, that the entrance aperture of the APTLens is imaged on the entrance slit SLT. This ensures, that the radial variation of the solar disc (e.g. different optical thicknesses of the solar atmosphere) is averaged over the entrance slit. This, in turn allows treating the vertical detector plane as repeated measurements in the evaluation. Two plane mirrors deflect the beam by 90° each and have minor effects on the optical setup, but cause the optical setup to be more compact. The mirror M_1 collimates the light beam on the grating. The grating is mounted on a motorized rotation stage to select the desired wavelength range that is projected with the mirror M_2 on the pre-illuminated detector plane. Pre illumination is necessary because the camera has a strong non-linear regime in the lower detector response region (see subsection 4.6.2).

In the following a few details will be given regarding the conceptual design of the GRC instrument.

Breadboard: Thermal and physical stress can cause the breadboard to bend or even oscillate. This causes changes in the optical setup such as de-focus or jitter in the image plane. A stiff breadboard with little thermal response is desired, especially since the instrument should operate in free-air conditions. Here, a carbon-reinforced breadboard is chosen. It is light weight (6.04 kg), very stiff and has a little thermal expansion ($2.7 \cdot 10^{-6} \text{ K}^{-1}$) compared to aluminum ($23.1 \cdot 10^{-6} \text{ K}^{-1}$, (Haynes, 2015)).

Housing: The entire instrument is covered in profile frame. The faces of the frame are covered with aluminum-PVC composite plates and are dust tight. The first lens in the system (APTLens) serves as window. The solar tracker with its mirrors is not covered. Heat producing elements (e.g. Control PC, power supply etc) are located outside for a better cooling.

Electronics: The additional electronics consists basically of two parts: Motor control electronics and communications for tracker motors as well as the grating rotational stage. Additional data such as GPS position, air pressure, internal temperatures, pre-illumination LED intensity is recorded with the second set of electronics. Both communicate with a serial interface with the control PC unit.

Apertures: Surfaces with low reflection in the visible range are not necessarily low reflective in the infra-red regime. Here, for field stop apertures, mostly made of metal sheet, are painted with a special black paint (Antireflexfarbe by Astrogeräte Berger⁴). Optic mounts by Thorlabs are usually shipped with a black paint. From measurements with the

⁴Astrogeräte Berger, Andreas Berger, Lützowstrasse 180, 42653 Solingen, Germany, <http://www.astrogeraete.de/index.html> (last accessed 16.05.2016)

parameter	value	unit	annotation
focal length f	508.0	mm	symmetric, gold coated
aperture diameter d	40.0	mm	
numerical aperture	20.0	–	
grating G	950	l mm ⁻¹	holographic, blazed at 900 nm
design wavelength	1606	nm	
design resolution	0.04	nm	at design wavelength, simulated
resolving power	40,000	–	at design wavelength, simulated
entrance slit	10	μm	
detector pixel width	30	μm	25 μm active area
design resolution	0.055	nm	at design wavelength, measured
design resolving power	29,000	nm	at design wavelength, measured
integration time	250	ms	at design wavelength, 80% exp.
field of view (FOV)	0.346	°	full angle, 65.2% of solar diam.
dimensions	850 x 370 x 260	mm	L x W x H
weight	≈ 18	kg	
power consumption	≈ 100 (150 peak)	W	peak occurs during calibration

Table 4.2: Key parameters of the implemented grating spectrometer.

optical setup the reflectivity of the used Antireflexfarbe, the reflectivity in the NIR is over $\frac{1}{4}$ lower than the black paint used on the Thorlabs mounts.

Table 4.2 gives an overview of the final design parameters of the implemented grating spectrometer GRC. In addition the used optic or mechanical parts are presented in Table 4.3. All these parts contribute to the properties of the final instrument. In the following section the used detector characteristics will be described in more detail, since this part of the spectrometer posed several challenges regarding non-linearity and unintended interference phenomena.

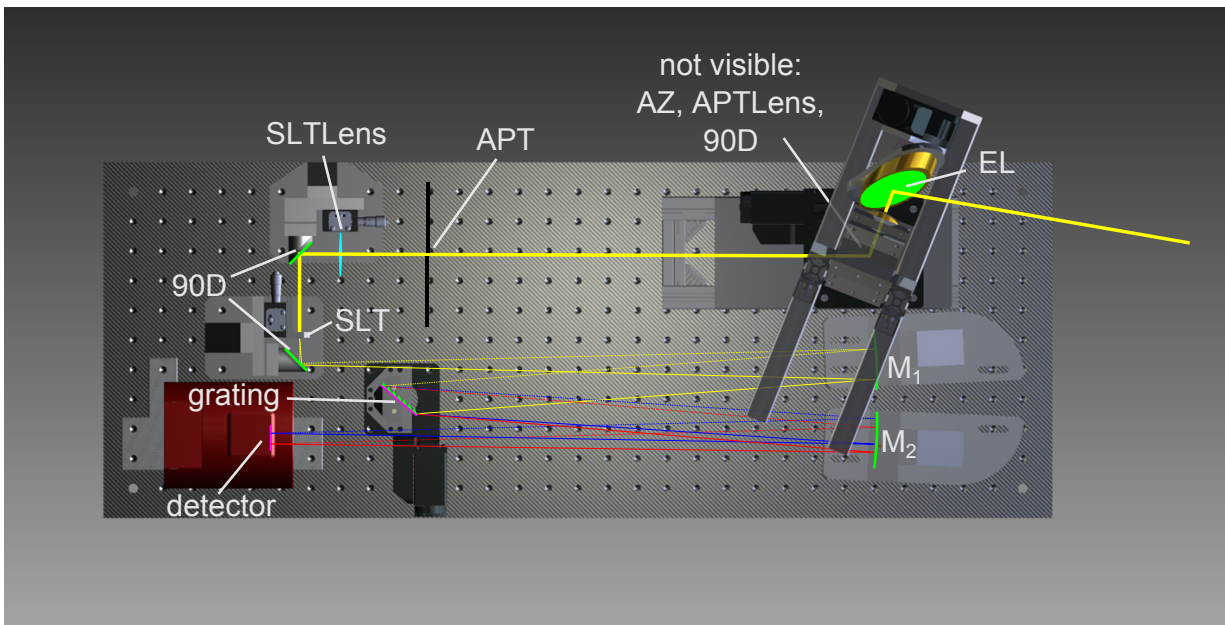


Figure 4.6: CAD-drawing of the implemented grating setup. The light beam is sketched in yellow. Colors of the optical components are analogue to Figure 4.7. Two flat mirrors (90D) fold the light path such that the instruments dimensions tend to be more compact. Not shown here are additional stray light apertures, which prevent uncontrolled optical paths on the detector.

component	properties	order number	supplier
tracking mirrors	Al coat. elliptical. 50 mm small axis	GSFS50	teleskop-express
large 90D flat mirror	Al coat. elliptical 63 mm small axis	GSFS63F	teleskop-express
APTLens	NBK7, IR-coat. f=500 mm d=2"	LB-1909-C	Thorlabs
SLTLens	NBK7, IR-coat. f=75 mm d=1"	LBF245-75-C	Thorlabs
SLT	W=10 μ m, h = 7.5 mm, black one side	custom	National Aperture inc.
small 90D flat mirror	Al coat. elliptical 20 mm small axis	GSFS20	teleskop-express
M _{1,2}	Au-coat. f=508 mm d=2"	32-822	Edmund Optics
Grating	9501 mm ⁻¹ , 30(h) x 40(w) mm ² , holo, 900 nm blaze	530 60	Horiba scientific
Grating Turntable	Motorized rotational stage	8MR190-2-28	Vision Lasertechnik
InGaAs 2D detector	256 x 320 pix , window removed	Goldeye P-008 SWIR cool	Allied Vision Technologies
CFK Breadboard	300 x 800 x 60 mm	custom	Carbon Vison
Black Paint	less than $\frac{1}{4}$ reflectivity in the NIR nm	ref. to Thorlabs paint	Astrogeräte Berger

Table 4.3: Key components of the implemented grating spectrometer and their suppliers.

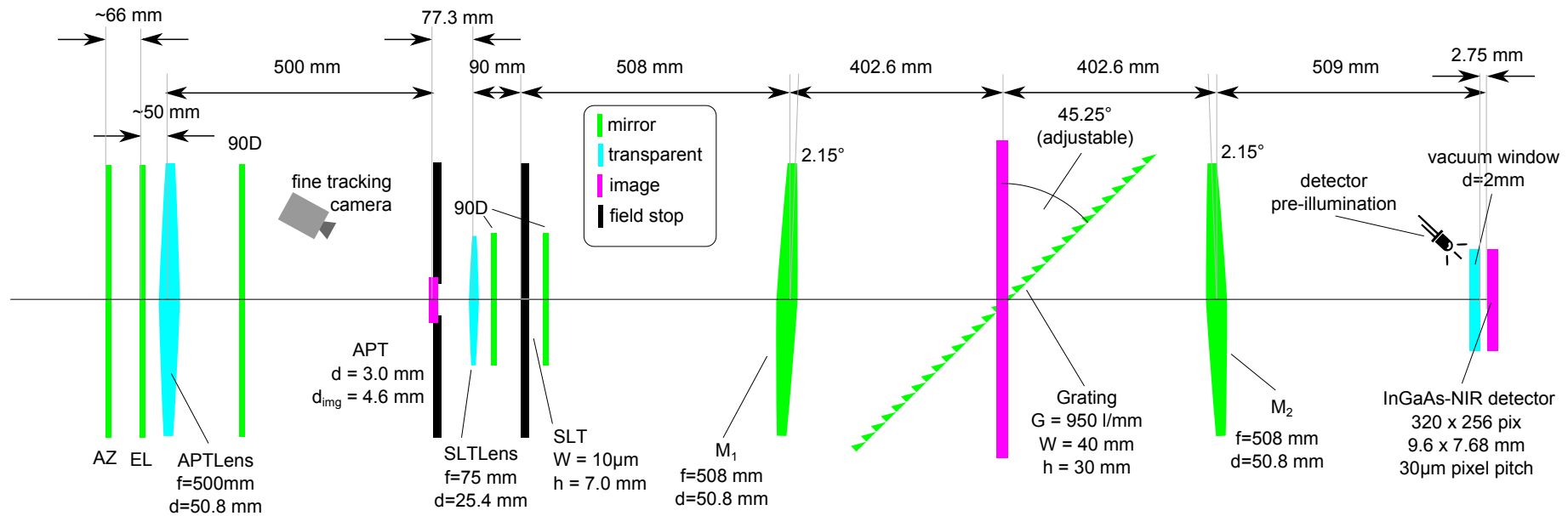


Figure 4.7: Linear representation of the optical setup of the grating spectrometer GRC. Reflecting surfaces are sketched in green, transparent surfaces in light blue field stops are black and image surfaces are purple. Here, AZ and EL denoted as azimuth and elevation flat tracking mirrors. The aperture lens (APTLens) images after a 90° deflection by a flat mirror (90D) the solar image on the entrance aperture APT. This image is used for the solar tracker as optical feedback. The second lens (SLTLens) focuses the solar image on the Grating. Before and after the entrance slit aperture (SLT) the light is deflected by 90° twice. The collimation mirror (M_1) projects the light on the grating by introducing an off-axis angle. The grating disperses the light and reflects it onto the camera mirror (M_2). Here an off-axis angle negative to the one before compensates off axis effects partly, before the image is projected onto the pre-illuminated camera array.

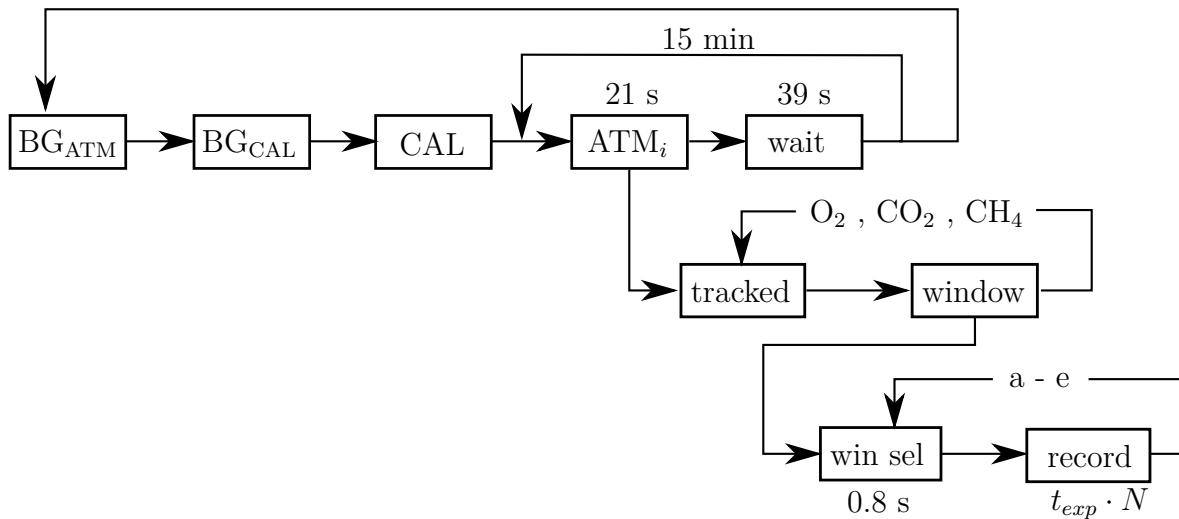


Figure 4.8: Atmospheric measurement scheme of the grating spectrometer (GRC). The atmospheric measurement series (ATM_i) is framed by the reference measurements (BG,CAL). This measurement scheme can be optimized for the sake of fast data acquisition if desired so that a single ATM-measurement can be recorded within 3 seconds by skipping the window select (O_2, CO_2, CH_4) and the micro-window select (a-e).

4.5 Data acquisition and processing

Before details on the used components of the grating instrument will be discussed, the acquisition and processing scheme of the grating instrument GRC will be presented. This includes the atmospheric data acquisition scheme as well as a principle introduction into the use of a 2D detector element.

4.5.1 Data acquisition

Due to the working principle of grating spectrometers a distinct wavelength range called “window” can be recorded at a time. These narrow windows in the order of approximately 40 cm^{-1} have to be selected individually. One spectral record contains the 2D spectral pixel array stored as an 256×320 int32 array. If averaging is selected the average is stored and additionally the standard deviation as a 256×320 int64 array. Further data such as the center wavelength, temperatures, pressure, tracking residual during record and many other parameters are stored in the human readable header of the 964 kByte file. Figure 4.8 explains the acquisition. One atmospheric measurement (ATM) sequence consists of five micro-windows for each of the O_2 , CO_2 and CH_4 windows and needs 21 seconds if the solar tracking is not disturbed. Since the trace gases are not expected to be very variable in time, a wait cycle of 39 seconds is implemented before the next ATM-cycle begins. This cycle is embedded into a 15 minute calibration cycle. Here, the dark or background (BG) and the calibration lamp spectra are recorded. The BG record is taken while the tracker points on a target of black paint with low reflectivity in the NIR. For the lamp calibration spectra the tracking device points into a collimated tungsten lamp (see subsection 4.6.3). Table 4.4

parameter	O_2	CO_2	CH_4	unit
window	1250-1290	1575-1615	1620-1660	nm
micro-window - step	10	10	10	nm
window	7752-8000	6292-6350	6024-6173	cm^{-1}
micro-window - step	34.5	21.7	37.2	cm^{-1}
window name	O	N	M	
exposure time	20	50	60	ms
cycle time (effective)	2.6+0.8	7.3+0.8	8.9+0.8	s
max freq (estimate)	50	20	16	Hz

Table 4.4: Window wise record parameters.

summarizes the acquisition scheme with respect to further parameters such as window size, exposure,- or cycle-times.

This recording cycle is not optimized for speed yet and can be made faster using the advantage of the grating instrument. Since the signal to noise ratio of the detector is well above 1000 for a single pixel, averaging over several 2D spectra is not necessary. Additionally a set of 5 micro-windows is recorded for each trace gas species in this cycle. A careful selection of one micro-window for each trace gas species can increase the record frequency by an additional factor of 5. The remaining dominant delay is given by the selection of the micro-window what is well below 1 second. So an ATM-series for O_2 , CO_2 and CH_4 can be recorded within less than 4 seconds. The focus on a single species would make grating rotations obsolete and single spectra can be recorded with a frequency of 20 Hz for CO_2 and 16 Hz for CH_4 . Compared to the EM27 instrument with a minimum integration time of approximately 12 seconds for a two fold spectrum the grating instrument here brings a significant advantage of a high frequent data acquisition, best suited for strongly variable trace gas concentrations.

Before the processing steps will be sketched, a single record will be explained in the description of Figure 4.9.

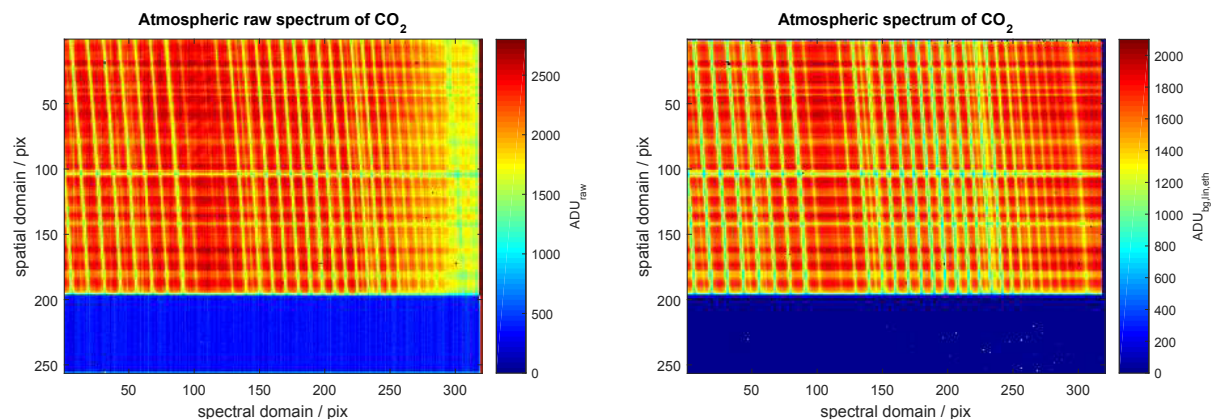


Figure 4.9: A single atmospheric spectrum from the spectral window N (CO_2) and the micro window 'd'. Left figure shows the color coded raw record with no corrections applied. Here along a row (abscissa, indexed by j) the spectral information is contained and the vertical dimension (ordinate, indexed by i) represents the spatial dimension, basically represented by the entrance slit (SLT) that is by design gently inclined towards the vertical pixel dimension. Reddish colors correspond in good approximation to the solar intensity I_0 whereas the bluish vertically inclined rows are atmospheric absorption features, mainly of CO_2 . By design, the lower section from approximately row 200 onwards is a non-illuminated section, with the background intensity. The non-zero values indicate the background intensity as the sum of detector dark-current and the additional background illumination (see subsection 4.6.2 or Figure 4.7).

The right figure shows the identical spectral record, but with all corrections (linearity,-, background,- and etalon-correction) applied. Defective pixels that are most abundant at the top and right side of the picture, are flagged as nan-values. The previous non-zero background region from row 200 onwards is approximately zero due to the BG-correction. The correction for etalon (ETH) removes the faint interference pattern at the pixel coordinates $i \approx 120$ and $j \approx 60$.

After the description of the measurement scheme now the evaluation will be described in more detail from the raw record series to the calibrated spectrum. The section starts out with the overview of the applied corrections. Later these corrections will be described more in detail. It can be divided into three parts. First the Level 0 processes that are applied to the 2D record. Secondly the up-sampling process described in section 4.7 and finally the retrieval process described in chapter 5.

4.5.2 Data processing

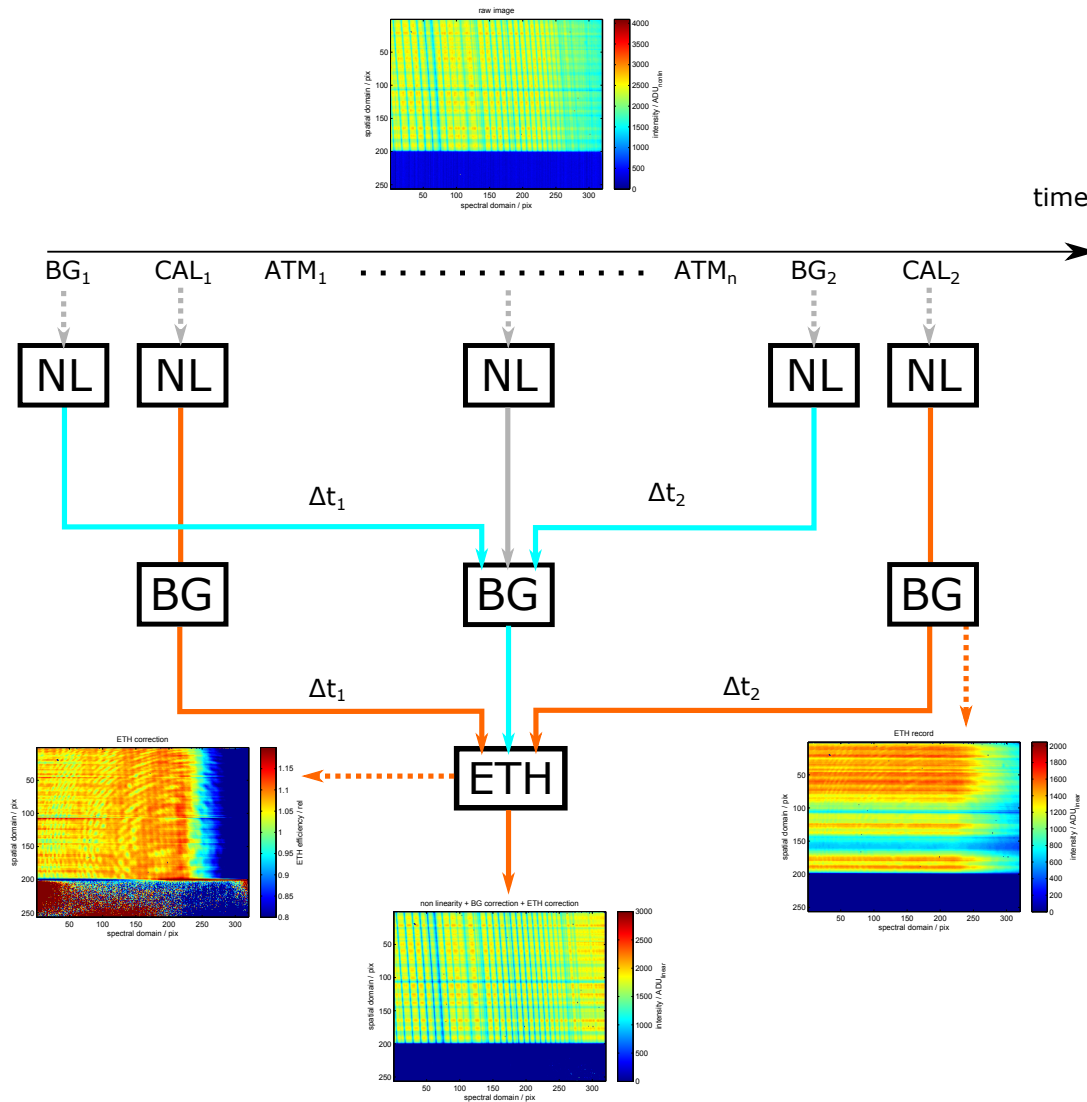


Figure 4.10: Level 0 data processing on the 2D data. First the non-linearity correction is applied (NL) and then the background-correction (BG) on the atmospheric measurement (ATM). After all the correction for the detector etalon (ETH) is applied, using the calibration record (CAL). The calibration records before and after the ATM are weighted each with the time difference to the ATM record (Δt)

In the following section the data processing scheme will be presented. It connects the data acquisition scheme 4.5 with the corrections described in the previous sections and

ends up with a calibrated spectrum that can be analyzed in the trace gas retrieval (see chapter 5)

The Level 0 process contains all corrections that can be applied to the 2D record. Despite this, each pixel has its individual treatment. Basically three corrections are applied in this step. First the non-linearity is corrected according to the characterization according to Equation 4.12. All records, regardless of the purpose, are corrected for non-linearity according to the specific exposure time. This includes the background records (BG) as well as the etalon reference records (CAL). The value of defective pixels is replaced by nan⁵-values. In further processes these values will be ignored. Next step is the BG-correction.

Finally the correction for etalon is applied (ETH). The linearized calibration images (CAL_{*i*}) are weighted temporally after BG-correction analogue to Equation 4.6. This approach might be questionable, since averaging the etalon might not be similar to the real etalon. Attempts to take just the closest record, however, lead to similar results. In a next step the record is normalized row-by-row and then used as a correction as described in Equation 4.12.

After the Level 0 data process the up-sampling (see section 4.7) takes place and calibrates the record to a spectrum $I(\nu)$.

4.6 Photonic detectors

In the following section the properties of photon detectors suitable for spectroscopy will be discussed. After a brief introduction on the working principle of photon detectors and their flaws are presented and how they can be characterized in order to correct them. Mainly the detector background (BG), non-linear detector response (non-linearity) and unwanted interference effects will be discussed.

Nowadays photons can be detected using semi-conductor devices. Figure 4.11 sketches the working principle of this array, which can be separated into three steps: First the conversion of photons into an electronic signal, second, the pre-amplification of this signal and finally the conversion from the electronic signal to a digital value with an analog-digital-converter (ADC).

Central element here is a semi conducting p-n-junction that is a diode. Photons with a discrete energy $E_\gamma > E_{gap}$ can generate electron-hole pairs if the band gap energy is lower. These charge carriers (in the following photo electrons) produce a photo current. This current can either be converted in a resistor to a proportional voltage or alternatively charge a capacitor. The voltage on the capacitor increases proportional to the number of photons and after the exposure time t_{exp} the voltage is processed further. Before the next readout, the capacity has to be reset before the next integration starts. In the next step this weak signal in the order of typically a few mV is amplified and then converted to a digital value. This value are discrete steps, typically from $0-2^n$ that map to the voltages $V_{min}-V_{max}$. In the

⁵nan stands for not a number

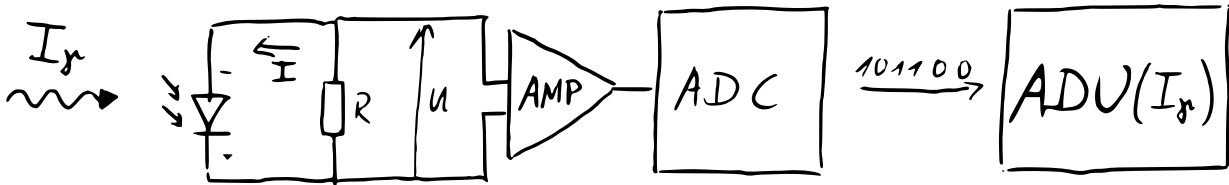


Figure 4.11: The photon intensity I_γ can be absorbed by a photo diode that produces a current I if the photon energy is higher than the band gap energy $E_\gamma > E_{gap}$. After pre-amplification this current can be converted by an Analog to Digital Converter (ADC) into a digital value ADU that can be computationally processed.

following these values are called AD-units (ADU). A wide range of pixel arrays is available today for multiple applications from X-ray detection in medical and scientific applications along photography in the visible spectral range to multiple near-infra-red applications for science and defense purposes. All these detectors work in a similar principle with variations depending on the application. For practical applications some effects of photo detectors have to be accounted for. To begin with the dark-current, a generation of photo-electrons even in complete darkness.

4.6.1 Detector dark current

Photon stimulation is not the only way to overcome the band gap energy E_{gap} to produce a photo current I_γ . Thermal excitation can increase the population density of the conduction band according to the Maxwell-Boltzmann-Distribution. This is called dark-current, since it is present with the non-illuminated detector. For the generated dark current follows in dependency on the temperature T and the Boltzmann-constant k_b the strongly non linear relation (Widenhorn et al., 2002)

$$I_{dark} = AT^3 \exp\left(-\frac{E_{gap}}{k_b T}\right) + BT^{3/2} \exp\left(-\frac{E_{gap}}{2k_b T}\right). \quad (4.5)$$

A and B are constants that depend on various chip parameters such as the detector size and further parameters.

Since this effect is statistically reproducible a non-illuminated detector signal can be recorded and subtracted from further measurements. Using this approach, it is important that all detector parameters, i.e. the exposure time and detector temperature remain constant over time. Detectors can be temperature stabilized to keep the dark current constant. Subtracting the dark record from the target measurement cancels out additional detector effects such as electronic offsets and thus is a common approach. However, this correction requires a linear photon response.

To correct for BG, the linearized background intensity is subtracted from the ATM spectrum that is recorded at the time t . To avoid discontinuities and compensate thermal drift effects, the background from before the ATM at (BG_1, t_1) and the background from after (BG_2, t_2) is weighted by the time differences $\Delta t = |t - t_i|$:

$$ATM_{BG} = ATM - (w_1 \cdot BG_1 + w_2 \cdot BG_2) \quad (4.6)$$

$$\text{with } w_i = \frac{\Delta t_i}{\Delta t_1 + \Delta t_2} \quad (4.7)$$

In this work the entire used detector images regardless the purpose are corrected for BG. Since multiple electronic elements within the detector electronics may introduce non-linear photon response, this effect is discussed in the following subsection.

4.6.2 Detector non linearity

Ideally there is a linear relation between the incident photon flux (I_γ) on the detector and the digital *ADU*-value. However, several electronic effects disturb this linear relationship so the photon detector response is not necessarily a strictly linear function.

The effects of nonlinear detectors in Fourier transform spectrometers are very different since they appear in the Fourier space rather than the actual transmission spectrum (e.g. Chase, 1984; Richardson et al., 1998; Palchetti et al., 2002).

Basically two techniques are common to characterize detector photon response (Sha, 2013): Both record a series of detector signals while the photon flux on the detector is varied in an accurate way. There are calibrated light sources available to perform this task directly. However, these light sources are technically difficult because most current driven light sources (light bulb or LED) vary their intensity non-linearly with driving power and depend strongly on temperature. Instead of tuning the light source itself one could use variable apertures as suggested by Sanders (1962) or Zwinkels and Gignac (1991). This in turn requires a highly homogeneous light beam as well as high precision apertures.

Alternatively the intensity can be altered using the fact that irradiance I from a point source depends on the distance r : $I_\gamma \propto \frac{1}{r^2}$. This approach, however requires a long distance travel of a point-like-source with a high precision.

Since most detectors have an integrating mechanism implemented to cope with different light conditions the variation of the integration time is an alternative option under the assumption that the integration time correlates linearly with the detector electrons generated. However, this comes along with the disadvantage that the dark signal changes with the integration time. Also the electronic amplifier or the AD-converter might behave differently with different integration times due to device specific characteristics.

In the framework of a bachelor's thesis by (Kostinek, 2013) an alternative approach was tested without the need for a calibrated light source similar as described in Frehlich (1992): Again a series of detector signals is recorded. This differential method uses two light sources S : The intensity of S_{var} can be varied stepwise whereas the second light source S_{ref} is a constant reference. Two detector signals belong together: The first record is an arbitrary

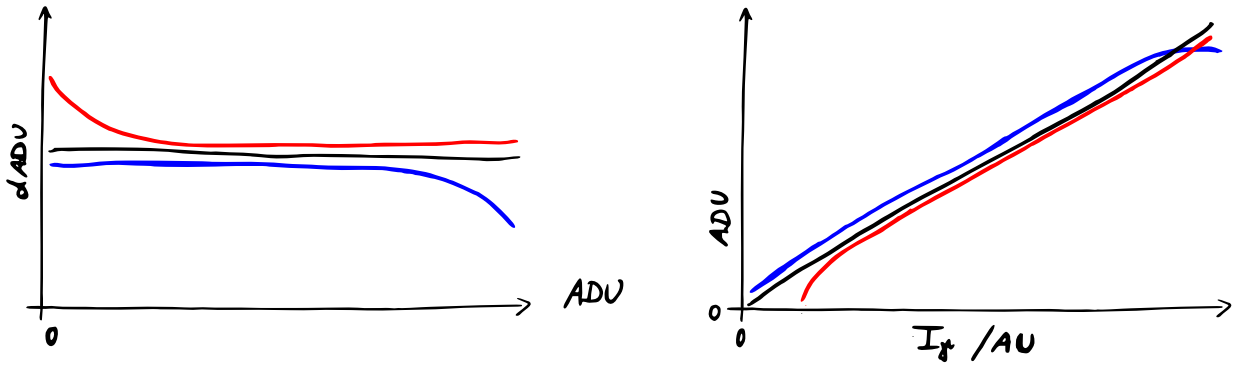


Figure 4.12: Differential detector response (left) and nominal detector response function (right). An ideal detector response (black) is compared to nonlinear functions with nonlinear behavior at high intensities (blue) and low intensities (red).

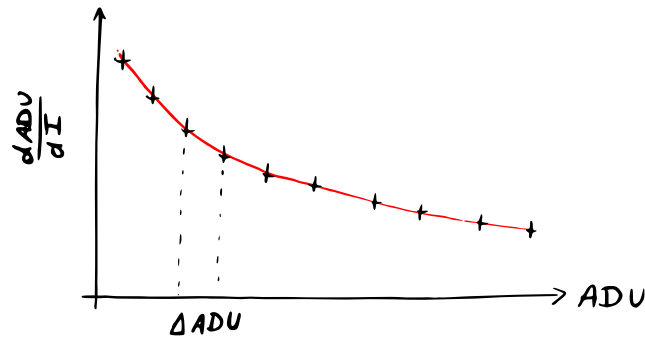


Figure 4.13: The linear response ΔI_γ can be approximated by ΔADU since the local, linear response to the intensity dI at ADU is measured as $dADU$. Here, I_γ represents the linear intensity.

detector signal ($ADU(S_{var})$) that is recorded. The second, weaker signal S_{ref} is added to the first one and a second detector signal is recorded which in turn leads to

$$ADU(S_{var} + S_{ref}) = ADU_{var} + dADU = ADU_{var+ref}. \quad (4.8)$$

The result gives a good quantitative measure on the regions of strong nonlinear detector response by plotting the results as sketched in Figure 4.12 (left). With this method non-linearity's can be identified without the need of a calibrated light source and without the variation of the exposure time.

To obtain the transfer function from the photon intensity to the detector response $I_\gamma(ADU)$ the previous work can be advanced as follows. Starting with the dark detector signal ($ADU(I_\gamma = 0) = 0$). From this point the linear response to another recorded detector signal ($ADU_{var_1} - ADU_{var_0} = \Delta ADU$) can be linearly approximated with

$$\Delta I_\gamma = \frac{\Delta ADU}{dADU} dI_\gamma \quad (4.9)$$

since the response to an additional amount of photons dI_γ is known. Here, the absolute value of dI_γ is not important, but it is constant. These intensities ΔI_γ can be summed up upon the desired detector signal. Figure 4.13 depicts this idea.

$$I_\gamma(ADU) = \sum_{ADU(I_\gamma=0)}^{ADU} \Delta I_\gamma|_{ADU} \quad (4.10)$$

$$= \sum_0^{ADU} \frac{\Delta ADU}{dADU} dI_\gamma \quad (4.11)$$

To remove the small error from the local linearization this procedure can be iterated until $dADU_{linearized}$ is constant within the detector noise for all detector intensities ADU in the record.

The used NIR-2D InGaAs pixel array ‘‘Goldeye P-008 SWIR Cool’’ from Allied Vision Technologies has a strong nonlinear response function and could be characterized with this method. Figure 4.14 shows the result after several iterations of Equation 4.11 for an individual pixel bottom and the entire pixel array (top). Since dI_γ is given in arbitrary units the result can be scaled such, that $ADC_{max} = I_{\gamma,ax} = 4100$.

Additionally this method comes along with the advantage of characterizing defective pixels that can be identified as outliers in the retrieved parameters. Furthermore the correction of pixel to pixel variations known as ‘‘non uniformity error’’ comes along with this correction procedure. Here it is important that the intensity ΔADU is fairly homogeneous along the pixel array. Figure 4.15 demonstrates this correction for one of the illuminated images.

With respect to spectroscopic measurements the non-linearity can be characterized for each desired exposure time t_{exp} and applied to the spectroscopic record with the same exposure time. To lower the computational effort a set of parameters $\mathbf{p}_{t_{exp}}$ represents the derived linear response $I(ADU, t_{exp}, i, j, \mathbf{p})$ for each pixel i, j , so this correction can be applied with very little computational effort:

$$I(ADU, t_{exp}, i, j, \mathbf{p}(i, j)) = \sum_0^n p_n \cdot ADU^n \quad (4.12)$$

This correction is part of the processing chain described in section 4.5.

Besides the great advantage of this method that there is no need for a calibrated tunable light source, it can be applied easily and repeated during a measurement campaign if desired. The computational effort for the characterization takes a few minutes per exposure time. The correction itself (Equation 4.12) has negligible computational time, even for a 256x320 pix array.

Limitations of the approach show in very low illuminated detector regions. Since this forms the starting point of the integral, errors here propagate to the upper regimes as well.

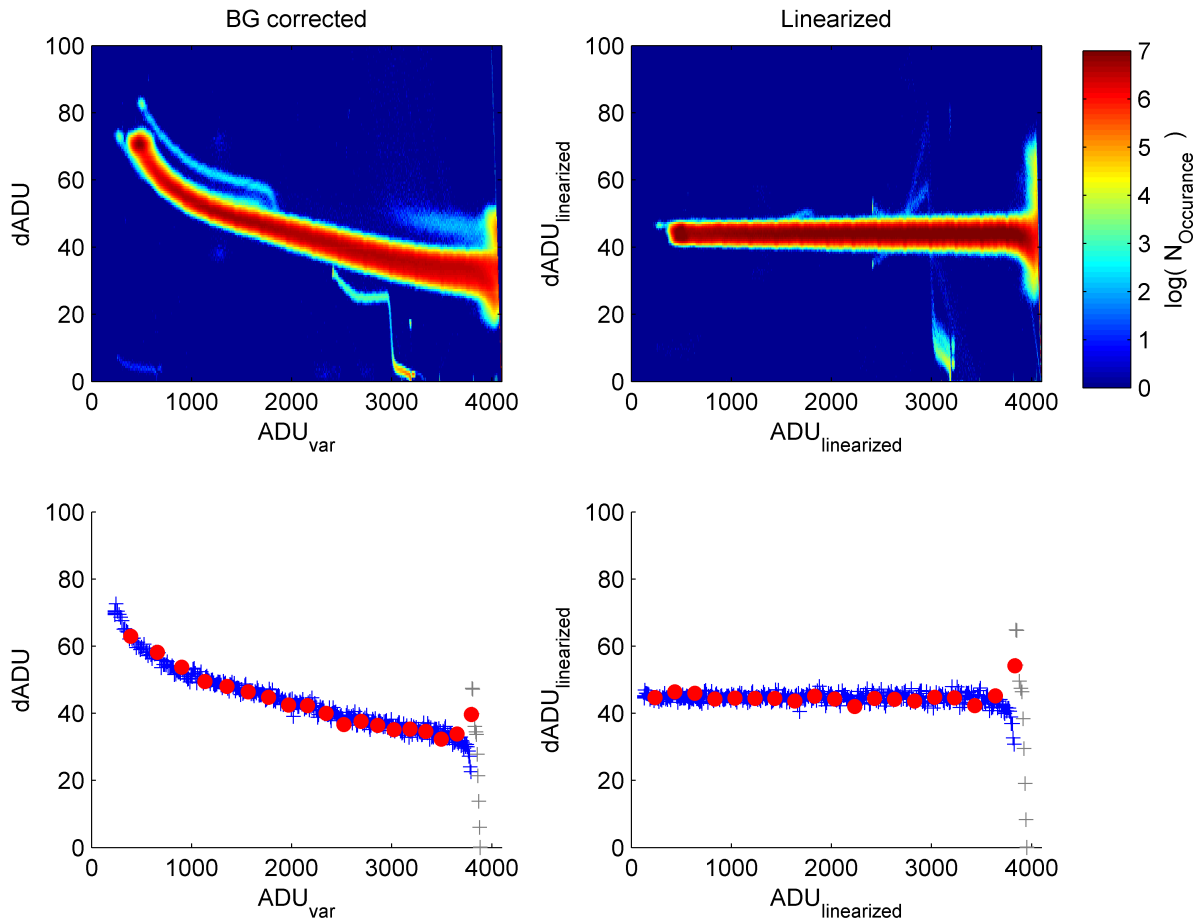


Figure 4.14: Left panels show the raw detector response with just the BG-correction applied. The right panels show the linearized detector signal. The upper panels show a 2D histogram in logarithmic color scale of the entire pixel array of 320x256 pixels. Most of the pixels show a similar detector response. However some outliers can be identified and considered as defect pixels. The lower panel shows one arbitrary pixel. Some of the measurement points (blue +) are not evaluated (gray +). Additionally a subset of linear, equidistant measurements (red dots) is displayed: Both represent the same measurement and demonstrate the change in the abscissa before and after calibration.

To overcome this downside, the detector can be characterized and pre-illuminated by a constant light source during the spectroscopic measurement to avoid these low intensity regions. This comes along with a slightly smaller dynamic range of the detector response, for the sake of an advanced linear detector response. In the example shown in Figure 4.14 a pre-illumination of additional 300 ADC would be sufficient to avoid this low intensity region. This would lower the dynamic range by approximately 7%. Additionally the non-linearity might change with temperature or other external effects such as a variation of the supply voltage or electromagnetic interference. These effects have not been investigated in this work and so far there is no indication of any further detrimental effects.

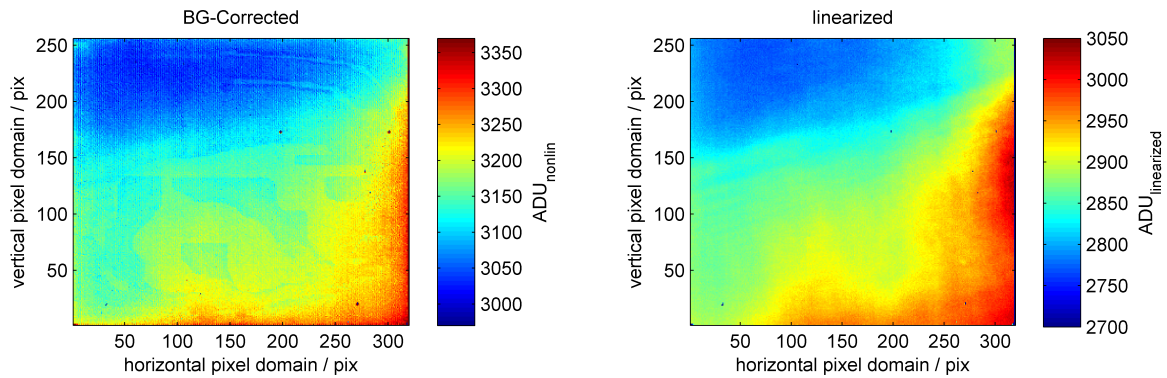


Figure 4.15: The side effect that pixel to pixel variations can be corrected is shown here. A measurement that is just BG-corrected shows clear variations along the illuminated array. This variation disappears for the non-linearity corrected image.

4.6.3 Etaloning - unwanted interference patterns

As shown in subsection 4.3.2 already, the test setups revealed interference patterns on the detector. The transmission intensity on the detector is altered by 9% or more. Since this effect is not a global scaling on the spectrum but a strongly wavelength dependent modification it is to be expected that this will have influence on the trace gas retrieval.

The section is structured as follows: First the theoretical basics of etalon effects will be given. In a next step the individual contributions to the total interference signal will be disentangled, basically by applying a Fourier analysis on a lab measurement series. From this analysis the characteristics, mainly the thickness d can be derived and allows to avoid the sources of interference in future instruments. The subsection closes with the correction scheme for the interference on atmospheric measurements.

Interference on a detector can occur if multiple optical paths join in the detector plane and these paths differ by the optical path difference O . Plane parallel surfaces such as glass plates, thin lenses or detector layers can add additional optical paths due to multiple surface reflections and cause interference structures.

The transmission intensity I_t from the intensity I_0 through plane parallel plate reflective surfaces, reflectivity r and the transmission $t = 1 - r$ can be described as a Fabry-Perot-Etalon:

$$I_t = I_0 \frac{(1 - r)^2}{1 + r^2 - 2r \cos(\delta)} \quad (4.13)$$

$$\text{with } \delta := 2\pi\nu O \quad (4.14)$$

$$\text{and } O := 2n_r d \cos(\theta) \quad (4.15)$$

Here θ is the angle of incidence, d the thickness and n_r the refractive index of the plane parallel plate. In the following $\theta = 0$ is assumed. Here O corresponds to the free spectral range (\mathcal{FSR}) in terms of wave numbers. Defining the contrast amplitude A of the etalon

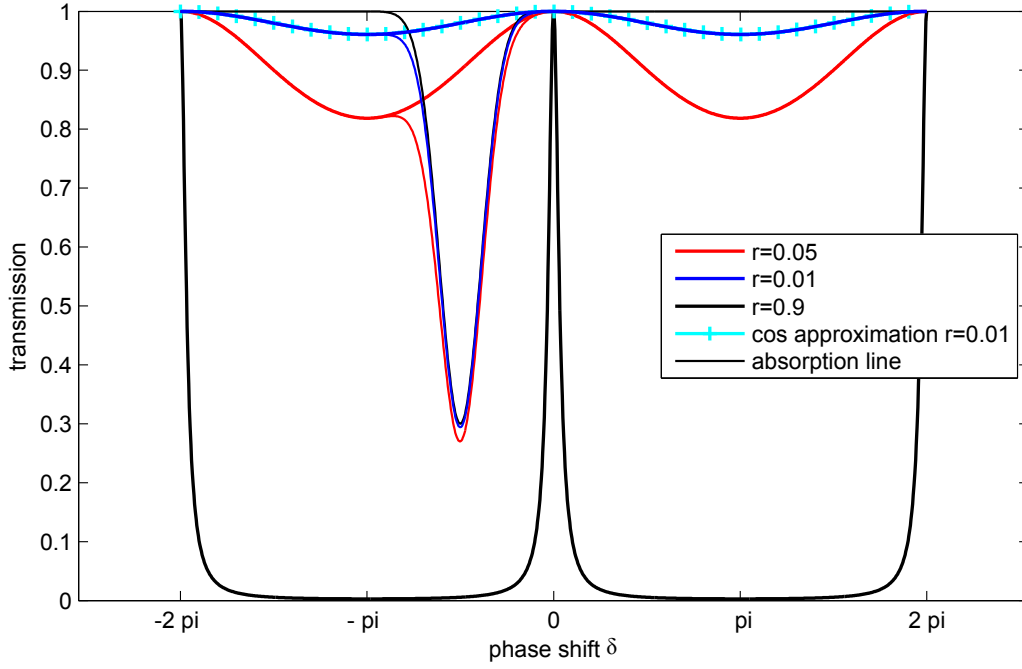


Figure 4.16: Illustrative transmission characteristics for several Fabry-Perot-Etalon structures with variable reflectivity (see Equation 4.13). Low reflectivity's r (blue), can be approximated by Equation 4.17 (cyan +). The absorbers intensity will be attenuated accordingly, regardless of the spectrometer's resolution qualities.

as $A := I_{t,max} - I_{t,min} = 1 - \frac{(1-r)^2}{(1+r)^2}$ one can see that an increasing reflectivity r increases the etalon effect.

If multiple interferometers are present in an optical system, the effective I_{eff} transmission intensity can be calculated by the superposition of individual contributions.

$$I_{eff} = I_0 \sum_n I_t(r_n, \delta_n) \quad (4.16)$$

For low reflectivities $r \ll t$ this contrast A can be used to approximate I_t

$$I_t \approx I_0 \left(1 + \frac{A}{2} (\cos(\delta)) \right) \quad (4.17)$$

Figure 4.16 illustrates the transmission to a given optical path difference in dependence of the phase δ . Low reflectivities r show little attenuation of the signal. They can be approximated by the Equation 4.17. In addition the effect on an spectral absorber is shown located at $-\pi/2$. With increasing reflectivity the shape and depth of the absorption feature is altered and is expected to propagate into the final retrieved trace gas concentration, if unaccounted.

There are basically two options to suppress unwanted interference patterns: The removal of plane parallel surfaces from the optical setup and lower the surface reflectivity r of the

residual plane parallel surfaces. Transmission windows as they are used as protection glasses or optical filters can be replaced by wedged windows, with an angle of a few arc-seconds that destroys the interference condition. Additionally anti-reflective coatings lower the Fabry-Perot efficiency.

Regarding the used InGaAs 2D pixel array two measures in the optical setup were undertaken to suppress interference patterns. In the standard shipping configuration the camera comes with a window in front of the detector array to protect it from mechanical and chemical influences. This detector unit is mounted on a thermal control and embedded into a vacuum chamber with an additional window. Since the detector is well protected from the exterior surrounding by the vacuum window the additional detector window was removed by the supplier⁶. Additionally the vacuum window is coated with a anti reflective coating. The option to replace this window by a wedged window, with non-plane parallel surfaces was not chosen. The wedge angle on these windows can cause leakage of the vacuum chamber if not properly sealed.

Despite these actions interference patterns remained on the detector image. In order to find the sources of the interference, the following characterization approach has been undertaken. There is no need for changes on the GRC instrument and the detector can be characterized “in-situ”. Here, a broadband spectrum of a halogen lamp is used since this spectrum reveals the detector interference undisturbed by spectral absorption features. This record is identical with a *CAL* record (see Figure 4.8). An $f=60$ mm lens with AR-coating is mounted 60 mm in front of a 50 W light bulb⁷ feeds the collimated source intensity with the solar tracker into the spectrometers entrance. After a few minutes of thermalization the measurement started.

A series of N spectra \hat{S} is recorded while the grating is rotated in the smallest possible steps (approximately $9.2 \cdot 10^{-2} \text{ cm}^{-1}$). Figure 4.17 (left) illustrates this record. Spectral calibration (see section 4.7) assigns for each pixel i, j and for each record $n = 1, \dots, N$ a corresponding wavenumber $\nu(i, j, n)$.

$$\hat{S}(i, j, n) \rightarrow S(i, j, \nu) \quad (4.18)$$

A Fourier transformation \mathcal{F} converts this series $S(i, j, \nu)$ into transmission attenuation of optical path differences $A(i, j, O)$ and a given phase $\delta(i, j, O)$.

$$S(i, j, \nu) \xrightarrow{\mathcal{F}} A(i, j, O) \text{ and } \delta(i, j, O) \quad (4.19)$$

The calibration from grating-steps n to wavenumbers ν allows to identify the corresponding optical path difference O_n for each amplitude A_n and phase δ_n .

⁶Allied Vision Technologies - former VDS Vosskühler

⁷Osram Halogen Display/Optic lamp 64602 50 W 12 V G 6.35 NAED 54607, e.g. leuchtmittelmarkt.com

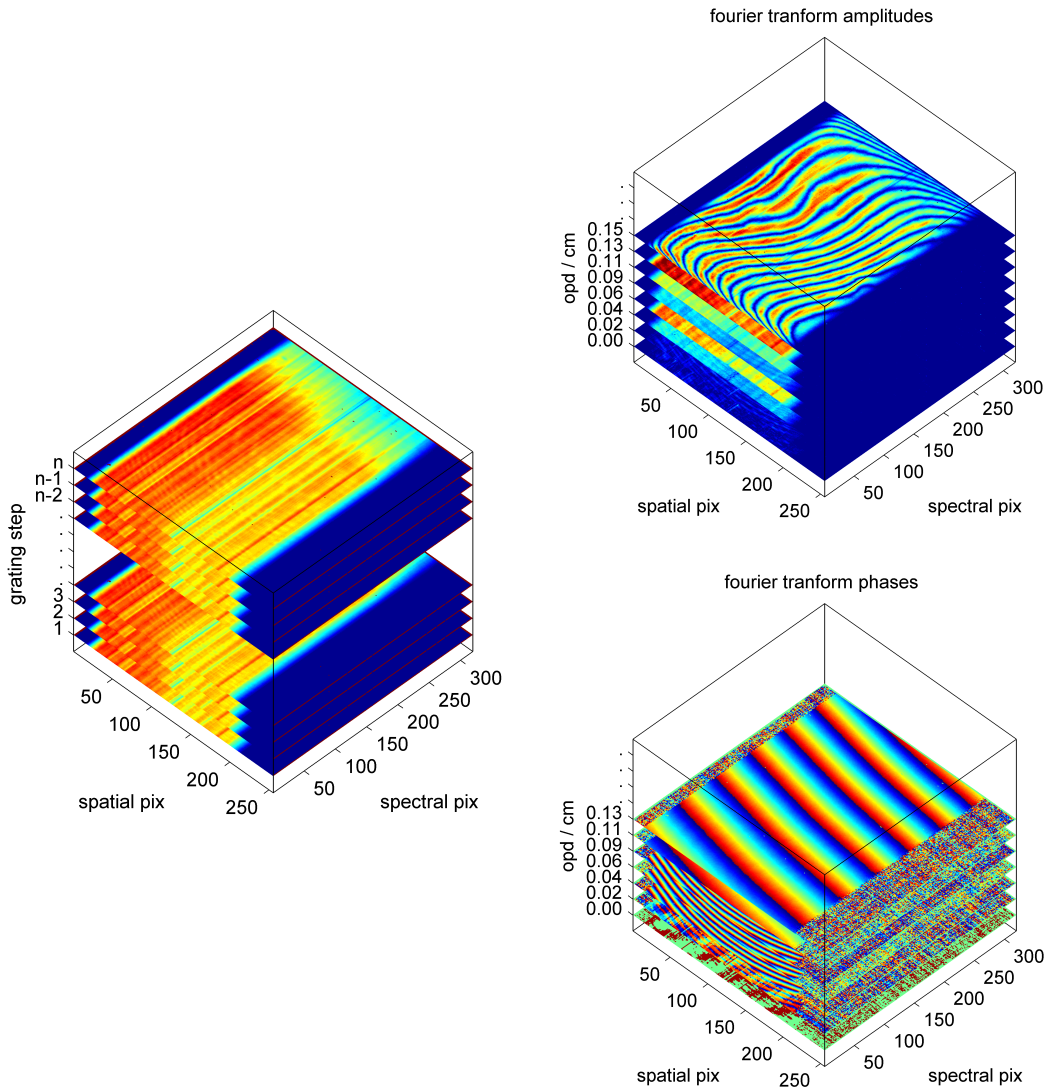


Figure 4.17: Illustration of the characterization approach: A series of N broadband spectra (left). For each individual image n the grating is turned and selects a different wave number domain. After Fourier Transformation (right) along the series axis (vertical axis) the interferometer-amplitude (top right) and corresponding phase (bottom right) is obtained.

For using the Fourier analysis in this assessment presupposes a low contrast A , so that the approximation Equation 4.17 holds and the result can be represented by a Fourier Series. In addition an equi-distant sampling in terms of wavenumbers is assumed. This is not entirely correct and might produce sampling artifacts. Figure 4.17 shows the idea of this approach. The set of N broad band spectra (left) can be represented by the corresponding amplitude A (top right) and phase δ (bottom right) via a Fourier transformation. Figure 4.18 shows a representative series before (left) and after (right) the Fourier Transformation for the arbitrary pixel $i = j = 100$. In this representation the dominant resonators are visible (upper right) with their corresponding optical path differences. This amplitude can be used to disentangle the individual contributions. The phase (lower right) here is of minor importance for this single pixel, but shows a shift to neighboring pixels: Going back to Figure 4.17 one can see that the phase here provides the most important information, since

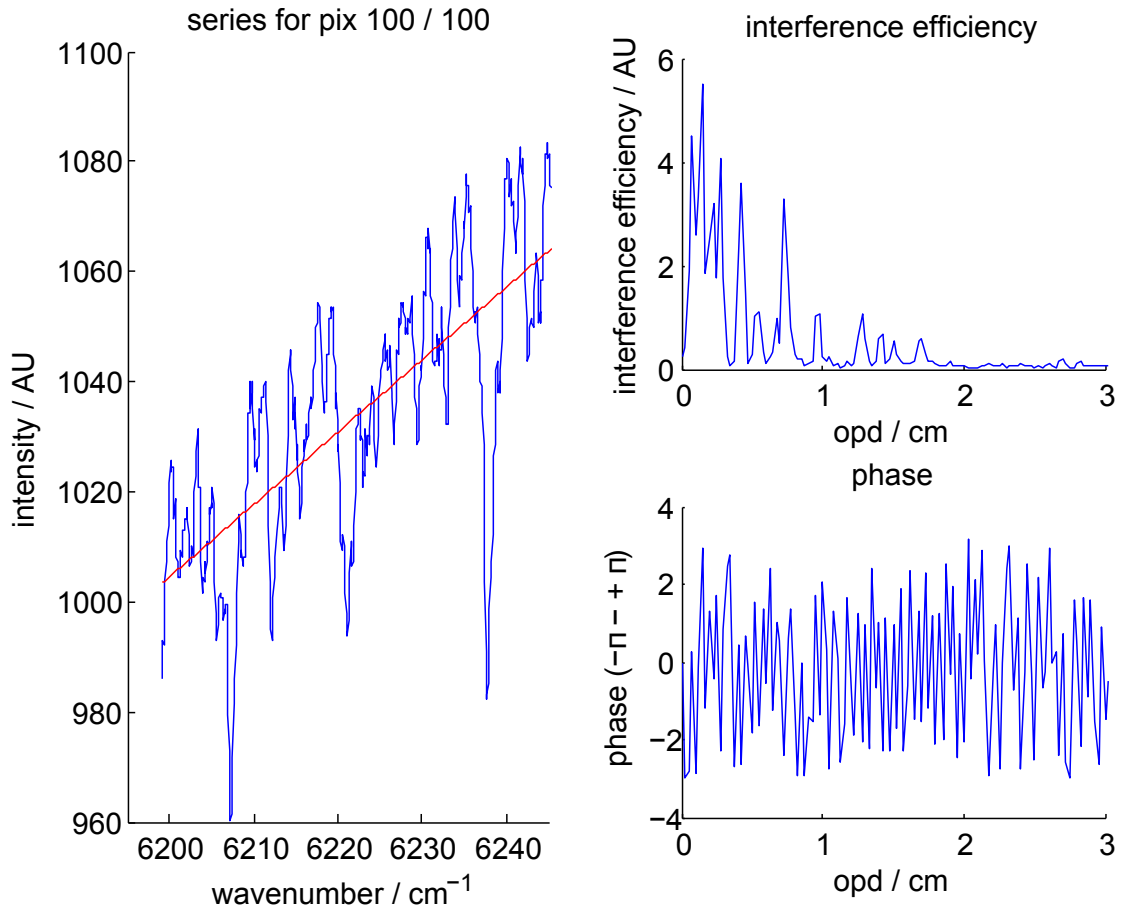


Figure 4.18: Illustrative Fourier analysis for pixel $i = j = 100$. The Fourier Transformation of the series record (left) gives the etalon efficiencies (top right) and the corresponding phase (bottom right). Assuming that the interference pattern does not change strongly from pixel to pixel, the phase for nearby pixels is similar. This can be used to obtain a phase map for each relevant etalon surface.

the phase shows pixel to pixel variations to a given optical path difference O (lower right). In this particular case the phase δ systematically increases from $-\pi$ to π along the spectral pixel domain.

Since the etalon amplitudes $A(i, j, n)$ only varies little from pixel to pixel a global presence of etalon amplitude a_n can be assumed:

$$A(i, j, n) \approx a_n \quad (4.20)$$

$$\approx a_{O_n} \quad (4.21)$$

Note, that there is an corresponding optical path difference O_n to each index n . Thus the most intense amplitudes a_n can be linked to a corresponding optical path difference O_n . Equation 4.15 allows to calculate the corresponding etalon surface thickness d assuming a refractive index n_r . With this approach it is possible identify the source of the interference pattern. Figure 4.19 shows corresponding layer thicknesses to the given interferometer n for different refractive indexes. Glass substrates used in the optical setup are basically

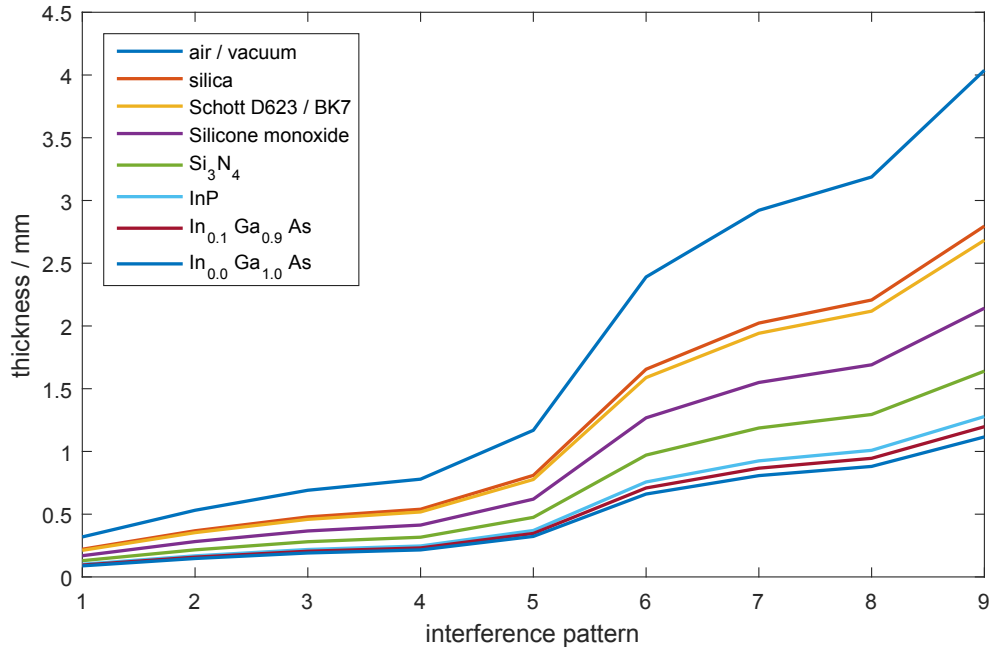


Figure 4.19: From the derived etalon efficiencies the source of the etalon effect can be estimated using the etalon equation (see Equation 4.13). An unknown variable is the refractive index of the plane parallel plate. Here some of the used materials are shown with the corresponding thickness d . It is likely that the etalon pattern #6 and #7 originate from the detector window with the thickness of 2 mm and made from Schott D623 glass. Ranging in the sub mm domain the patterns #1-#5 can originate from the detector substrate itself. A special case is #8 that might originate from the glass bulb of the calibration lamp.

fused silica⁸ in the light bulb and NBK7⁸ for the lenses. According to the manufacturer⁹ the vacuum window of the detector is made of 2 mm Schott D623-Glass. Used lenses with center thickness of 5.0 mm (APTLens) and 4.3 mm (SLTLens) made of NBK7 glass are not candidates for the source since they are too thick and not plane parallel. The distance from detector to vacuum window is unknown and could range in the order of 4mm that would correspond to surface #9. But it is very likely, that the patterns from #1-#5 originate from the detector itself. Typical materials used are InGaAs¹⁰ in various dopants as well as indium phosphoride (InP)(Pettit and Turner, 1965) and silicon nitride (Si₃N₄) (Kischkat et al., 2012). Since these semi-conductor layers typically have a high surface flatness and parallelism they are prominent candidates for etalon interference. However the detector structure with respect to the layer thickness d and the refractive index n_r is a business secret of the manufacturer and could not be confirmed. Thus the source of the etalon remains speculative, but likely originates from the detector itself.

Since the etalon could not be removed by the changes in the optical setup, it has to be corrected before the trace gas retrieval.

⁸Data sheet SCHOTT AG; Hattenbergstrasse 10; 55122 Mainz; www.schott.com

⁹Allied Vision Technologies GmbH; Branch Office Ahrensburg; Klaus-Groth-Str. 1; 22926 Ahrensburg

¹⁰Online source: http://www.batop.de/information/n_InGaAs.html

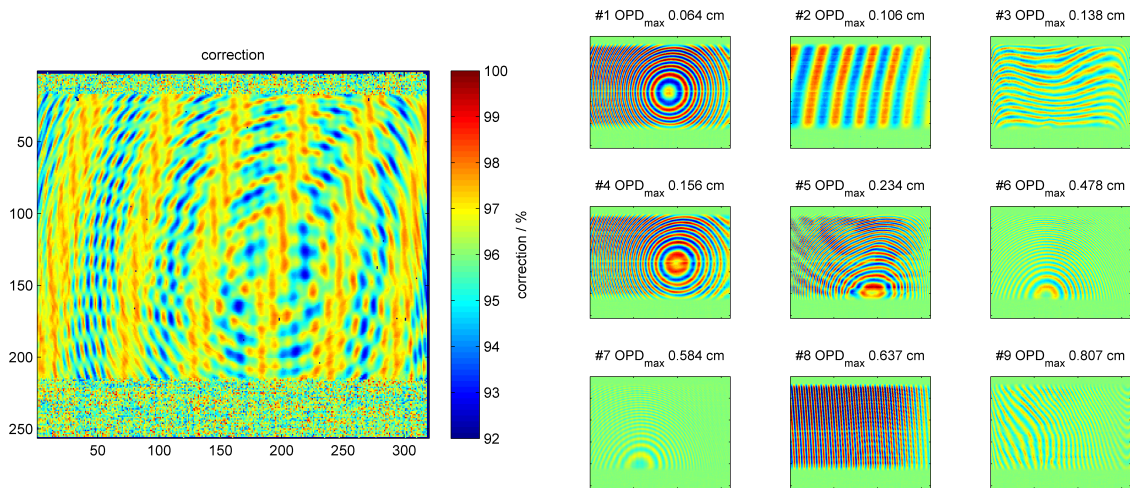


Figure 4.20: Color coded spectral attenuation intensities of a single record of a broadband spectrum of a light bulb at approximately 1600-1610 nm (left). Here the abscissa is the spectral domain, the ordinate the spatial domain in slit direction. This pattern is a superposition of individual interferometers to a given optical path difference O (left, s. Equation 4.16), derived from the lab characterization.

Now that the characteristic of each individual interference surface is known, it is possible to reproduce the transmission intensity of the interference using Equation 4.13 or the approximation Equation 4.17. Figure 4.20 shows the corresponding superposition (left) of nine individual interference structures (right). An obvious step would be to use this calculated transmission efficiency to correct for the interference. Tests on one of the lab record $S(i, j, \nu)$ showed a reduction in interference from 9% down to 2% using only the most important 9 surfaces. Including all 256 surfaces of this analysis the interference could be reduced to the residual noise level well below 1% with higher computational costs. Unfortunately the reproduction of the interference is too unstable to apply it to a measurement recorded under different conditions. Especially thermal drift makes this lab-characterization unique in the sense that it cannot be used to correct for interference of a spectral record recorded at another time for instance one of the *CAL* images (see Figure 4.8).

In general correcting for detector etalon requires that the interference can be resolved by the instrument. This means that the free spectral range of the etalon must cover several pixels. Or in other words there must not be interferometers in the system with $2\pi/O \gg \Delta\nu_{pix} \approx 0.14 \text{ cm}^{-1}$. Unresolved interference might not have a visual effect on the detector image. However, the narrow absorption features of individual trace gases, might be disturbed by these unresolved interferences as illustrated in Figure 4.16. This error will then propagate into the trace gas retrieval. Under controlled circumstances the Fabry-Perot etalon can be used to increase the resolution, combining a grating and an FTS instrument as Hajian et al. (2007) suggests.

Hence, a second approach can be applied, that uses a calibration measurement (CAL) temporally as close as possible to the atmospheric measurement to correct for the interference: From the raw CAL -image the correction I_{ETH} is derived and then applied to the spectrum ATM . Typically the spatial domain (ordinate) varies in intensity along the calibration record. This variation is different from that in the atmospheric spectrum. Thus it is not possible just to divide both spectra, since this would lead to in-homogeneities in the up sampling process. So before the etalon correction can be applied, the calibration spectrum recorded at the time t has to be normalized row by row to the average value of the row $\langle I_{CAL} \rangle_j$. Here, j is the spectral index and i the index for each row.

$$I_{ETH}(i, j) = \frac{I_{CAL}(i, j)}{\langle I_{CAL(i,j)} \rangle_j} \quad (4.22)$$

Assuming weak etalon intensities this then can be used to correct the atmospheric spectrum:

$$ATM_{cor}(i, j) = \frac{I_{ATM}(i, j)}{I_{ETH}(i, j)} \quad (4.23)$$

This approach avoids complicated estimates on the background intensity I_0 (see Equation 4.13) and rather assumes the cosine-approximation (see Figure 4.16) instead. However, this approach is simple to use, but has several downsides. First, it is important, that exactly the same window is selected by the grating rotation dish. Slight variations in spectral domain cannot be accounted for with this approach. This effect might be negligible with broadband interference patterns (e.g. surface #2 Figure 4.20) but becomes serious if high-frequency etalons are present (e.g. surface #4 left side Figure 4.20). In addition it might be possible, that interference structures originate from the calibration process itself. For instance, the light source might introduce interference at the glass housing. In this case the correction on an atmospheric spectrum, without the light-bulb interference, introduces an additional interference pattern instead of correcting it. The previous approach would allow to remove this contribution in the correction characteristic for the atmospheric spectrum. Lastly this approach cannot interpolate to an atmospheric measurement from the wrapping calibration measurements. So drift effects on the interference pattern from one calibration record to the next, cannot be corrected properly.

4.7 Spectral calibration and up sampling

The great advantage of the 2D detector array is that it either can resolve spatial information in one direction perpendicular to the slit direction or, if this domain does not contain additional information, it can be treated as repeated measurements. This only holds if the

imaging properties in the vertical slit direction can be assumed to be constant. In particular off-axis effects have to be negligible. The most important advantage of the additional dimension is the option to sample the spectrum with a higher sampling resolution. A typical bottleneck of a small sized grating spectrometer is the sampling resolution given by the detector pixel width (see Equation 4.4). In the UV-VIS (VIS stands for visible) spectral region detectors with pixel sizes of a few μm are available. However, NIR pixel arrays are larger by approximately a factor of 5 compared to UV-VIS detectors and range in the order of 25-30 μm pixel size. This limits the sampling of the obtained spectrum by the same factor. The sampling can be increased by inclining the slit direction gently towards the pixel orientation in order to sample the same part of the spectrum with a different pixel grid. In the data processing chain the up-sampling and spectral calibration is performed in one step. So first the spectral calibration procedure will be described and then the up-sampling.

The 256x320 ($i \times j$) pixel array of the used detector records the intensity $I(i, j)$ at a pixel at the vertical position i and the horizontal position j . Here, a horizontal pixel row corresponds to the spectral domain. Each pixel integrates the spectral intensity ν_{min} to ν_{max} and corresponds to a center wave number $\nu(i, j)_c$ for this particular pixel. To relate each pixel to its corresponding wave number, a calibration map can be created for a particular spectral window, which contains 256 of these rows. This calibration array is obtained row by row as follows: First a coarse calibration is performed. The spectral coarse calibration $\nu(i, j)_{coarse}$ can be calculated with the use of the grating angle θ and an angular calibration from the self-programmed simulation tool (see section 4.3). Besides a global offset in the order of 5 cm^{-1} the spectral coarse calibration still deviates approximately 0.4 cm^{-1} along the spectral row. A 2Deg polynomial $f_i(j, p)$ with the parameters p is used to refine this calibration:

$$\nu(i, j) = \nu(i, j)_{coarse} + f_i(j, p) \quad (4.24)$$

$$\text{with } f_i(j, p) = \sum_{n=0}^2 p_n j^n \quad (4.25)$$

The set of three parameters p for each row i is obtained by minimizing the difference D_i from the coarsely calibrated spectrum I to a reference spectrum I_{ref} recorded simultaneously with the EM27 instrument.

$$D_i = (I(i, j, \nu_{coarse} + f_i(j, p)) - I_{ref}(\nu(i, j, p)))^2 \quad (4.26)$$

So for each spectral window a calibration map $\nu_{win}(i, j)$ can be specified, that associates each pixel with the corresponding wavenumber.

Due to variations in thickness along the entrance slit, some of the rows happen to have lower intensities than others. These intensity variations affect in good approximation the

entire row i and can be characterized using the mean intensity $\langle I_i(j) \rangle_i$ to normalize the different illuminated rows to each other:

$$I_n(i, j) = \frac{I(i, j)}{\langle I_i(j) \rangle_i} \quad (4.27)$$

$$(4.28)$$

A fully illuminated detector would result in a spectral record of $256 \times 320 \approx 8 \cdot 10^4$ data points. Assuming a homogeneous distribution to the corresponding wavenumber calibration, this would result in an average sampling interval of approximately $6 \cdot 10^{-4} \text{ cm}^{-1}$. Since the instruments resolution ranges at approximately 0.25 cm^{-1} a down sampling to approximately $r = 2.5 \cdot 10^{-2} \text{ cm}^{-1}$ seems appropriate. The up sampling can be pictured as co-adding all relevant rows and reduces the statistical noise by \sqrt{n} , whereas n is the number of samples within the sampling interval $\nu \pm \frac{r}{2}$. The up sampled spectral Intensity $I_r(\nu)$ is calculated by

$$I_r(\nu) = \sum_n I(\nu_n) \cdot K_n \quad (4.29)$$

$$\text{with } K_n = A_n(r - |\nu_n - \nu|) \quad (4.30)$$

$$\text{and } A_n = \frac{1}{\sum_n K_n} \quad (4.31)$$

The weighting function K_n gives samples the more weight, the closer they are at the center sampling wavenumber ν . The choice of the weights has direct influence on the ILS since it can be pictured as a convolution kernel, a triangular shape in this case. Improvements might include the investigation of an alternative weighting function K for the up sampling process.

So far, this spectral calibration includes the characteristics of the nonlinear wavelength calibration on the detector plane. It does not account for a spectral shift that occurs because the grating motor does not drive to exactly the same position as it has been during calibration. This shift is in the order of up to $\pm 0.2 \text{ cm}^{-1}$. The local minimum of a strong absorption line is used to calibrate the residual offset for each individual spectrum.

The final result is an equ-distantly sampled and spectrum $I_n(\nu_n)$ with the spectral spacing $r = \nu_{n+1} - \nu_n$. It can be processed further in the trace gas retrieval described in chapter 5.

4.8 Instrumental line shape (ILS)

An important characteristic of the instrument is the instrumental line shape (see section 5.2 for more detail). The instrumental line shape, also called impulse response function, can be pictured as the instrumental's response to a δ -impulse-function. It can then be used as a

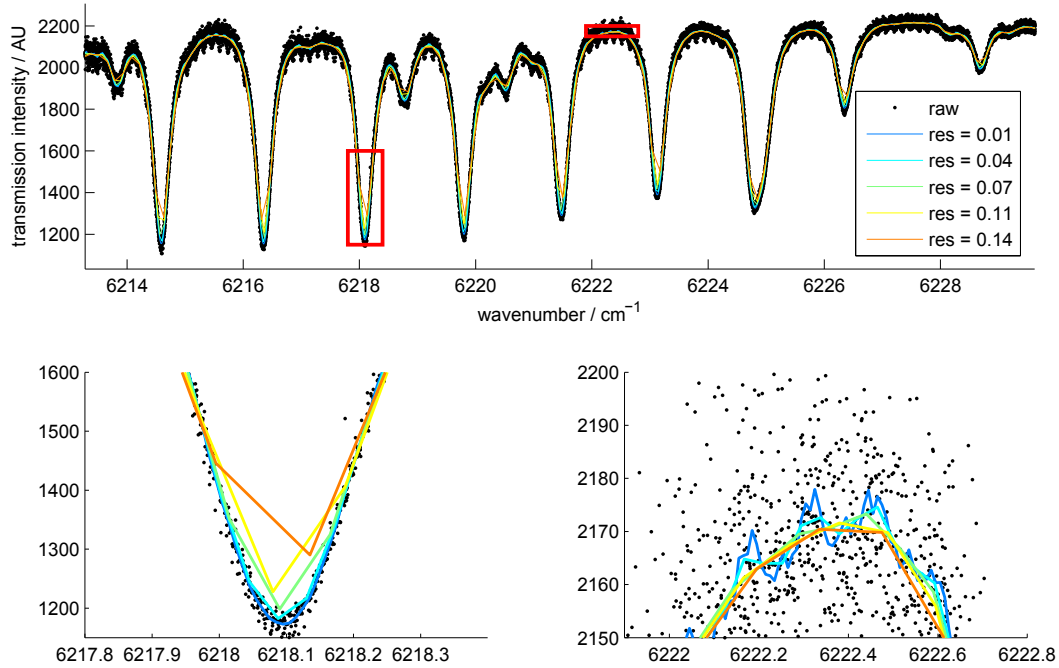


Figure 4.21: Top panel presents the overview of a raw calibrated spectrum (black dots). In addition final calibrated spectra are shown, with multiple sampling intervals in units of cm^{-1} . The lower panels show a zoom into two spectral regions (red boxes). High sampling resolutions produce sampling artifacts (lower left, blue line) where as low sampling resolutions decrease the overall resolution. The sampling resolution of 0.14 cm^{-1} corresponds to the approximate pixel pitch. Most of the scatter of the raw data points is introduced by the normalization process and corresponds to a standard deviation of approximately 1.1 % in reference to the up-sampled spectrum.

convolution kernel for the evaluation procedure. Here it will be described in more detail how the instrumental line shape of the GRC-instrument can be characterized with the use of a laser calibration source in addition with the ILS-retrieval software LineFit (Hase et al., 1999).

The transition function $h(\nu)$ can be measured directly by the impulse response of the used system (see Equation 5.4). In practical terms a spectral, narrow emission line with $\Delta\nu_{line} \ll \Delta\nu_{spec}$ is desired, where $\Delta\nu_{spec}$ represents the spectral resolution of the instrument. For this purpose elementary spectral emission lines from gas discharge lamps can be used¹¹. For example Hg-gas-discharge lamps emit a prominent and narrow line at 253.65 nm with a natural line width of $1.34 \cdot 10^{-7} \text{ nm}$ (Fuhr and Wiese, 2005). Especially in UV-VIS spectroscopy there are numerous intense emission lines that can be used for the ILS characterization. However, there are a few emission lines from elements in the NIR-region, where as Thorium suits best for the design wavelength (Redman et al., 2014). They are

¹¹The National Institute of Standards and Technology (NIST) provides a comprehensive list of emission lines with an online selection tool http://physics.nist.gov/PhysRefData/ASD/lines_form.html

parameter	value	unit
tuning range	1540-1650	nm
	6060-6493	cm ⁻¹
tuning step	0.01	nm
	0.039	cm ⁻¹
optical power	≈ 5	mW
FWHM	100	MHz
	8.5·10 ⁻⁴	nm
	3.3·10 ⁻³	cm ⁻¹
NA	0.11	–

Table 4.5: Tunable diode laser specifications

generated by hollow-cathode discharge lamps since the element Thorium is contrary to Mercury not gaseous under normal conditions. These lamps typically have low emission intensities and an emissive area of a few mm². Tests showed, that a Thorium-hollow cathode lamp is not suited for the characterization of the spectrometer since the intensity is too weak.

An alternative approach is to use a laser line for the ILS-characterization. Lasers typically have very narrow transition lines in the order of $\Delta\nu_{las} \approx 5 \cdot 10^{-4} \text{ cm}^{-1} \ll \delta\nu_{spec} = 0.15 \text{ cm}^{-1}$. In addition they are high in intensity and tunable designed. This means they can be selected to lase on a desired resonance wave number over a few ten to hundred cm⁻¹ range. In this work a tunable diode laser was used to characterize the ILS. The Osics ECL 1600 External Cavity Tunable Laser by Yenista¹² was used for this purpose. Table 4.5 summarizes most important laser parameters. A cost efficient alternative might be tunable laser electronics for telecommunication purposes, that use the so called “L-band” (1565-1625 nm, CO₂) or “U-band” (1625-1675 nm, CH₄)¹³.

Challenge here is to feed a homogeneous laser beam intensity into the spectrometers entrance aperture with a beam-diameter of 2” (≈ 50.8 mm). Figure 4.22 explains the optical coupling. The laser output is a single mode fiber with a numerical aperture $NA = f/D = 0.11$. It is collimated with a $f = 37.31$ mm fiber collimator (Thorlabs F810APC-1550) to a beam with approximately $d = 7$ mm diameter. This collimated beam is pointed on a diffuser plate. The diffuser plate is a micro-lens array (Thorlabs ED1-C20-MD) with the size of a single lens of approximately 50 μm. In total approximately 15,000 micro lenses with negative focal length open the collimated beam to 20°. A $f = 60$ mm lens collimates this beam again to the final 2” spectrometer aperture.

An additional effect has to be considered. Lasers usually have coherence lengths of a few hundred meters or more. This means that interference occurs within the dimensions of the spectrometer. In this case a typical speckle pattern on a screen can be observed. To break the coherence of the laser beam the diffuser plate is additionally rotated with a few hundred rotations per minute. This phase scrambler changes the optical path differences

¹²Yenista Optics S.A, 4 rue Louis de Broglie, 22300 Lannion, France

¹³JDSU-CW-TOSA type 5206-T, <http://wircom.ua/content/1728/5205t5206titlads.pdf>

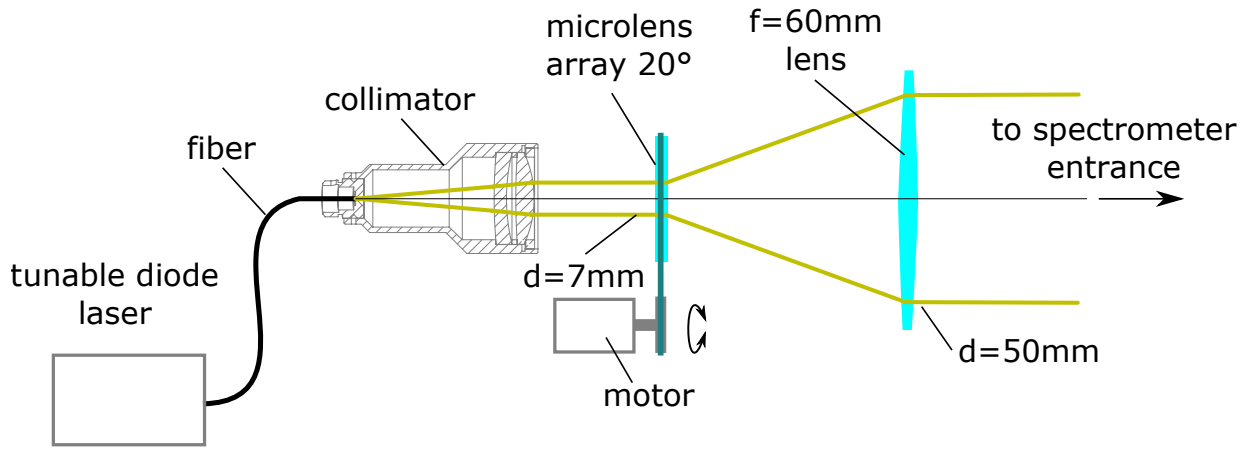


Figure 4.22: Optical setup of the laser coupling from the tunable diode laser (left) to the spectrometer entrance (right). The phase scrambler (middle) ensures a homogeneous, and speckle free detector image (see Figure 4.23).

continuously with high frequency. The integration time of the camera averages over these high frequency changes within the integration time of 20 ms.

Figure 4.23 shows the effects of the phase scrambler. The strong inhomogeneities are averaged under the use of the phase scrambler. All laser measurements have been performed using the phase scrambler. Possible weaknesses of this approach might arise from detector non-linearity. As depicted in subsection 4.6.2, the used detector suffers from non-linearity in photon response. The use of phase scrambler causes strong intensity fluctuations on an individual pixel during the integration time t_{exp} .

$$\int_0^{t_{exp}} e_{\gamma}(I_{\gamma}(t))dt = e_{\gamma} \left(\int_0^{t_{exp}} I_{\gamma}(t)dt \right) \quad (4.32)$$

Here $e_{\gamma}(I_{\gamma})$ denotes the photo electrons generated by the intensity I_{γ} in the semi-conductor absorber. Non linearity in this generation process of the photo electrons e_{γ} can cause systematic deviations. If Equation 4.32 does not hold, the non-linearity correction cannot correct for non-linearity properly. Residual structures in the retrieval (see chapter 5) indicate, that an errorus ILS results in a systematic residual at strong spectral absorbers. The recording scheme can be improved by using an alternate phase scrambler that could be a homogeneous stray target instead of the micro lens array.

If Equation 4.32 holds, non-linearity from further detector-parts (amplifier, ADC,...) can be corrected by the non-linearity correction and the non-linearity correction can be applied safely to the phase-scrambled records.

Figure 4.24 shows a record of a series of laser lines within the spectral window “a”. Due to vignetting effects (see Figure 4.10) the laser line at 6374 cm^{-1} is attenuated in the right section of the spectrum. It is to be expected that the ILS changes due to this vignetting effect. Thus the affected spectral range is neglected in further considerations. For reference purposes an atmospheric spectrum is shown as well.

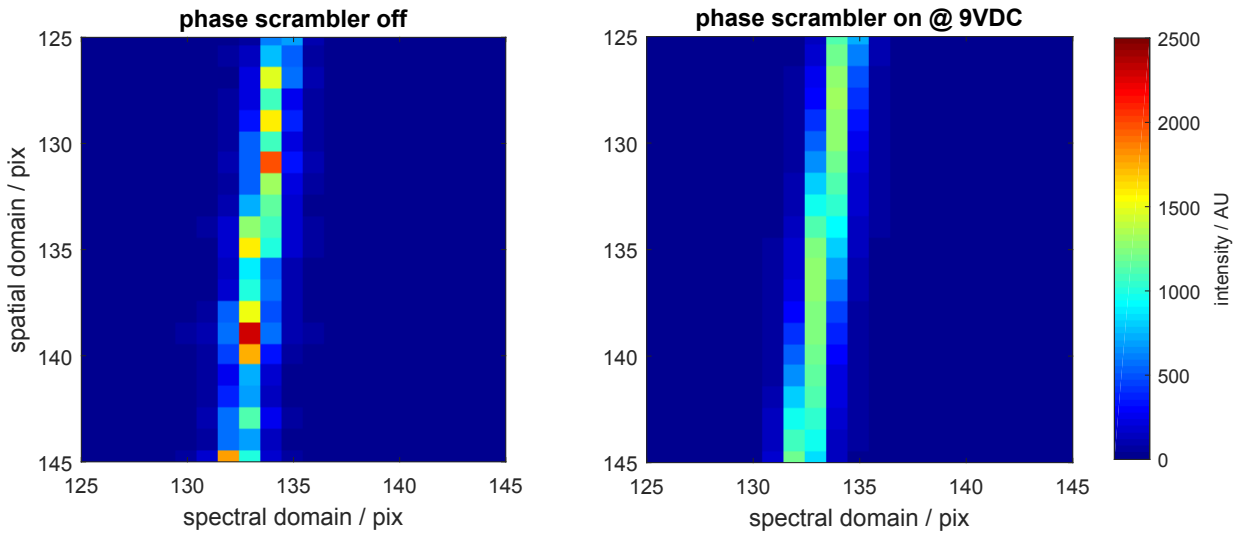


Figure 4.23: The color coded intensity of a single laser line coupled into the spectrometer, for a selected pixel section. Without phase scrambler (left) strong inhomogeneous pixel responses occur (speckles). The phase scrambler changes the speckle pattern with a high frequency, so the pixel response shows the average during the integration time of 20ms (right). Note that by design the slit is slightly inclined towards the vertical pixel domain.

Figure 4.25 allows a closer look at the ILS properties. All laser peaks are centered and referenced to the mean ILS of all peaks $I_{ref} = \langle I_n \rangle$. The residual is shown below. It is calculated by $R = (I - I_{ref})/I_{ref}$. A variation in ILS along the spectral axis would lead to a systematic residual. In fact this systematic residual can be seen on the vignettted laser line (dotted line) and causes a strong systematic offset (scaled by 0.1). The laser lines that correspond to each other show a much smaller deviation here. However there is noise involved. Typical detector noise for a single pixel is in the order of 6 *ADU* that would translate to a noise to signal ratio of 0.12% for a 50% illuminated scene with 2000 *ADU*. Lower intensities increase this ratio to more than 12% for a 1% illuminated scene. So the residual noise basically originates from detector noise. This could be enhanced by averaging over a multitude of records. It is to be expected, that this background noise translates directly into the retrieval process if this ILS is used for the instruments characteristic.

This procedure might be improved in three points: The correction of the etalon was not possible, since it has not been characterized during this measurement. Since etalon effects range in the order of a few percent (see subsection 4.6.3), this is a likely candidate to lower the noise of the ILS characterization. A second thought might be given to the phase scrambler. The speckles pose a highly dynamic variation, which might alter the ILS. It could be worth to consider an alternative approach of phase scrambling such as the use of a diffuse target instead of the micro lens array. The last option to suppress this noise can be the use of more laser lines. According to the laser specifications the number of laser lines could be increased to well above 1000 lines per spectral window.

For spectral fits that are shown in this work the corresponding ILS parameters are taken from this characterization set. The software package LineFit (Hase et al., 1999) retrieves a set of 2x20 parameters that reproduce the ILS within the retrieval. This parameters suit

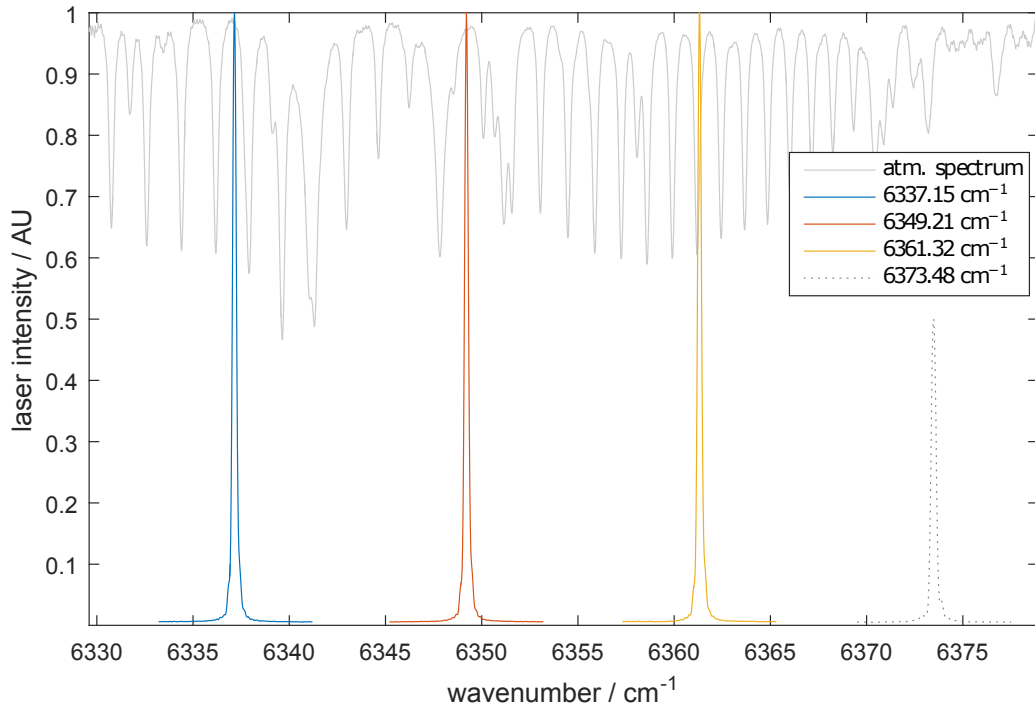


Figure 4.24: Records of the ILS for the spectral window “a” along the entire window range. The right most line was recorded with a lower intensity due to vignetting effects of the spectrometer. An atmospheric transmission spectrum is shown in gray for reference purposes.

best for the use with Fourier-Transform-spectrometers but are considered to be applicable within this work for the grating instrument as well. More details on the ILS-characteristics with respect to the retrieval can be found in section 5.2.

4.9 Performance and future improvements of the GRC

Three grating setups had been tested within this work for their fitness as a portable and robust IR-grating spectrometer to operate in direct sunlight spectroscopy. Despite the “immersed grating” could show excellent dispersing properties with respect to the instrument’s size, this setup was not chosen to be implemented in the final instrument. The design was not suited to measure atmospheric oxygen as a reference. In addition stray-light from the strongly reflective entrance face of the grating and possible thermal issues influenced the decision.

The final setup was chosen to be a conventional grating in Czerny-Turner configuration with 500 mm focal-length. Key feature is the use of a 2D InGaAs detector-array in order to enhance the spectral sampling. The detector could be characterized with respect to non-linearity and detector interference within this work.

The nonlinear detector response (ADU) to a linear photon flux (I_γ) could be successfully derived without the need of a calibrated light source and without the need to change the detector exposure time. For each pixel and integration time a correction function with

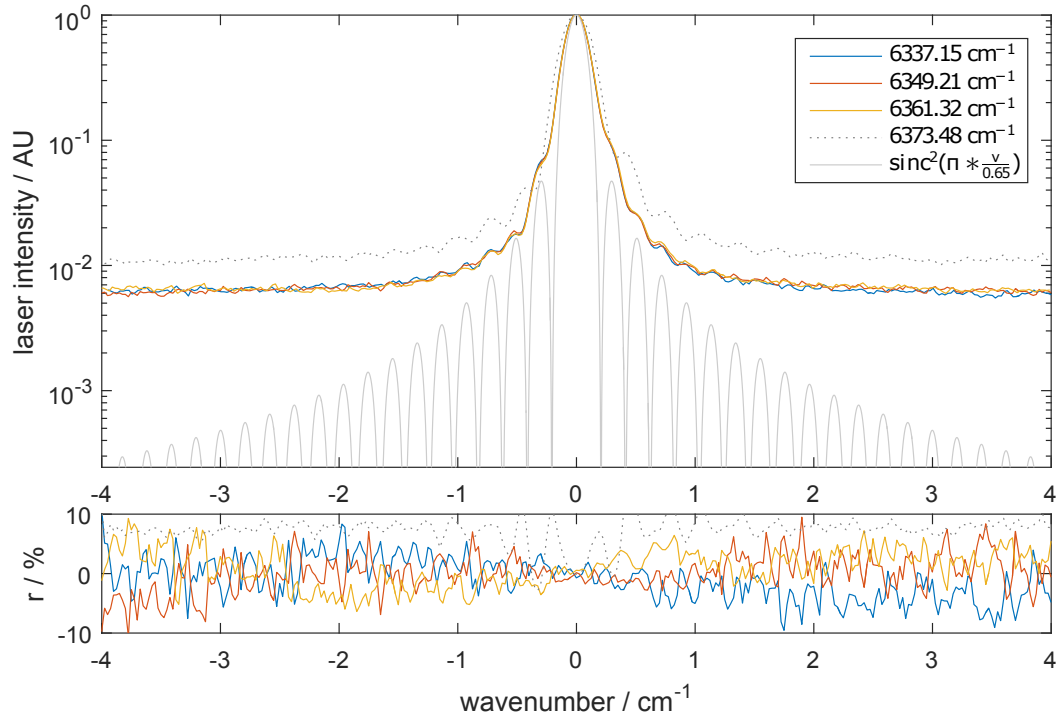


Figure 4.25: Variation of the ILS along the spectral window “a” for the four different laser lines in a logarithmic intensity. The lower end corresponds to the smallest, non-zero value that can be represented by the ADU ($\frac{1}{4096}$). The residual to the average peak is shown below and indicates slight systematic variations of the ILS along the spectrum. The residual of the vignettted laser line (dotted) is scaled by a factor of 0.1 and shows strong systematic deviations.

coefficients could be found that convert the nonlinear ADU units into linear intensities. In addition pixel-to-pixel variations in the photon response are automatically homogenized with this approach.

Further detector shortcomings are unwanted interference patterns that alter the signal by up to 9%. They could successfully be characterized in a lab measurement. From the characteristics it was possible to disentangle the sources from each other. From this characteristics the source of the patterns can be estimated and are very likely to originate from the detector structure itself. The corresponding thicknesses of the etalon-plates range in the order of a few ten to hundred μm - typical layer thicknesses of semi-conductor detectors. With a sub-set of the obtained characteristics it was possible to lower the interference to less than 2% when applying it to the lab measurement itself. This might be further improved by increasing the subset towards the entire set with the burden of higher computational costs. However it was not possible to derive a universal, parameter controlled correction set for each interference structure at any time of record. Thus the correction of the etalon has to be performed using the frequent calibration records CAL directly during the atmospheric measurements ATM .

The instrumental line shape (ILS) of the instrument could be successfully retrieved with a tunable diode laser as a light source. A challenge here poses the strong variation in intensity

(speckles) over the detector area due to the long coherence length of lasers. These speckles could be averaged away with a phase scrambler. Deficiencies show the line-wings which should be approximately an order of magnitude lower than they really are and indicate stray light. From these measurements the resolving power of the instrument can be determined to be 40,000 at the design wavelength of 1605 nm.

From the evaluation of a representative diurnal record (see upcoming section 5.3) the standard deviation of single CO₂ measurements amounts to 1.6 ppm. With respect to a 400 ppm background this is equivalent to a precision of 0.4%. Main driver for this scatter might be the detector interference in combination with in-accuracies of the grating rotation. The individual spectral window is selected by grating rotations. In-accuracies in re-visits of a distinct spectral window disturb the etalon correction scheme.

Further, the thickness of the used entrance slit material amounts to approximately 12.7 μm stainless steel. It is likely that the slit height of 7.5 mm in combination with local inhomogeneous heating due to solar intensity on the slit causes instabilities. It is possible that the slit bends or even flips over during the measurements. A filter that removes the visible intensity on the entrance slit could reduce the heating power. Additionally a smaller slit height might be appropriate and give more stability.

Spectral residuals (see Figure 5.3) indicate that the instrumental field of view might not be properly chosen. This effect should be subject to future investigations in the retrieval process together with stray-light assessments. Despite much effort had been made to suppress stray-light, the zero-stray light assumption might not be correct.

Finally the focal length of the instrument can be decreased in future implementations. Here a focal length of 350-400 mm seems appropriate that would reduce the instruments dimensions accordingly.

However, the GRC grating spectrometer has a significantly shorter sampling interval (exposure time) in comparison to FTS-instrument EM27/SUN with similar properties. For the EM27/SUN IR-FTST the shortest possible sampling interval amounts to approximately 12 seconds for a double sided interferogram. A grating instrument with three static detectors could measure the desired target gases of CO₂, CH₄ and O₂ within approximately 250 ms or less, yielding a factor 48 faster instrument.

5 Retrieval - from spectrum to total column

This chapter introduces the retrieval theory that is used to obtain the trace gas concentrations from the measured spectrum as described in section 1.2. Focus is put upon key aspects of relevance within this work. Since the instrumental line shape (ILS) is an important impact parameter, it will be discussed in a dedicated section.

After this introductory part, spectral retrieval results of the GRC-grating instrument as well as the EM27/SUN FTS-instrument are presented in section 5.3. This chapter closes with the description of post-processing steps such as the reference to the oxygen total column, SZA-correction, calibration to the WMO-calibrated TCCON instrument. In addition it will be described, how the exhaust plume detection is performed in order to identify soundings that read enhanced CO₂ concentrations when the line-of-sight passes the ships exhaust plume.

5.1 Retrieval theory

As introduced in section 1.2.1 qualitative and quantitative information about atmospheric trace gases can be obtained from a spectroscopic absorption or emission signal due to the presence of spectroscopic active molecules. Most of the section 5.1 and section 5.2 is summarized from Rodgers and Connor (2003), Hase (2000); Hase et al. (1999) and the publication Klappenbach et al. (2015).

The general idea of the spectral retrieval is to minimize the differences of the measured signal $\mathbf{S}(\nu)$ to the modeled signal $f(\mathbf{x}, \mathbf{b})$ by the forward model f . Here, the forward model includes the physical knowledge about the system. \mathbf{x} denotes the unknown atmospheric state vector and \mathbf{b} denotes parameters which are not part of the state vector and considered to be constant or known. Assuming \mathbf{x}_{true} as the true (typically unknown) atmospheric state vector, an ideal retrieval with an ideal measurement $\mathbf{S}(\nu)$ leads to

$$\lim_{\mathbf{x} \rightarrow \mathbf{x}_{true}} |\mathbf{S}(\nu) - f(\mathbf{x}, \mathbf{b})| = 0. \quad (5.1)$$

Here the norm of \mathbf{X} is denoted by $|\mathbf{X}|$.

A convenient measure of the retrieval result is the total column, or total vertical column of a gas that can be calculated from the measured spectrum. It basically represents the

total number of molecules per unit area along a vertical atmospheric profile and can be calculated using the total column operator \mathbf{h}

$$n_{gas} = \mathbf{h}^T \mathbf{x}_i \quad (5.2)$$

In case the state vector \mathbf{x} would only contain the number of molecules per unit area of each atmospheric layer \mathbf{h} , would return the sum of \mathbf{x} . The molar mixing ratio, often given in ppmv (parts per million volume mixing ratio) is then given by

$$c_{gas} = \frac{n_{gas}}{n_{col}} \quad (5.3)$$

with n_{col} the number of all atmospheric molecules. Note, that for inter comparisons with other instruments (including model data) the a-priori-profile as well as the averaging kernel has to be taken into account (Rodgers and Connor, 2003)

This trace gas retrieval can be implemented into multiple software packages such as PROFFIT¹ (Hase, 2000; Schneider et al., 2008; Sepúlve da et al., 2012), GFIT (Wunch et al., 2011) or RemoteC (Butz et al., 2009, 2010)). The implementations, however may differ in the regularization algorithm and complexity.

This work uses the software package PROFFIT v.9.6 (Hase et al., 2004) for the spectral retrieval of absorber total columns. In principle, PROFFIT is capable of retrieving vertical profile information from high spectral resolution measurements of the atmospheric transmittance in direct-sun view (García et al., 2012). However, the medium resolution of 0.5 cm is not sufficient to retrieve profile information since the pressure and temperature broadening effects are not resolved properly by both instruments GRC and EM27/SUN. Therefore, here, a setup is chosen, that only retrieves a scaling parameter for the a-priori absorber profiles. In particular the number of degrees of freedom (DOF) was chosen to be one (DOF=1). Table 5.1 gives an overview of the most important retrieval setup properties for the EM27/SUN and GRC respectively.

In the following the most important retrieval parameters within this work will be pointed out. To begin with the best known part \mathbf{b} that is typically not retrieved and left unchanged.

Instruments field of view (FOV) The instrument’s FOV defines the section of the solar disc that corresponds to the solar background intensity I_0 (see Equation 1.11) before telluric absorption features are added. The larger the FOV the more solar absorption features are added, since solar limb regions correspond to larger solar “air-masses”. Typically this parameter is considered to be known and left unchanged.

Spectral line list Spectral absorption features of individual trace gases (see subsection 1.2.1) are listed in “line list” repositories. Within this work line lists based on the HITRAN² (Rothman et al., 2009). Adaptations in these lists are found to be necessary and used within this work (Lamouroux et al., 2010; Wunch et al., 2011). Besides the spectral position and absorption intensity of the particular gas these lists contain parameters to

¹PROFile FIT

²High resolution TRANSition molecular absorption database

control the pressure and Doppler broadening effect (see subsection 1.2.1). Along the light path through the atmosphere typically various pressure and temperature conditions are present. In order to account for these variations properly, a pressure and temperature state of the atmosphere is needed called “PT profile”.

Pressure-Temperature profiles Atmospheric pressure and temperature conditions along the light path alter the spectral line shape. The accuracy of these profiles is of particular importance especially at high resolution spectra. Meteorological models provide such profiles on a global scale (e.g. NCEP³). Since these vertical profiles typically modeled up to 60 km altitude average monthly atmospheric conditions are used for altitudes above up to 120 km from CIRA-86⁴(Chandra et al., 1990). These profiles typically do not represent variations over the day. From the measured ground pressure these variations can be accounted for in the entire profile.

Profile a-priori Since the retrieval problem is considered to be ill-posed, meaning that solutions are not unique, additional information has to be provided, mainly by the profile a-priori \mathbf{x}_a . This a-priori is a best estimate on the trace gas concentration along the line of sight and is part of the state vector $\mathbf{x}_a \cap \mathbf{x}$. In case of a scaling retrieval a single parameter x_{sc} is retrieved, that scales the a-priori profile. Within this work profile a-priories are used from CAMS⁵-model output (Agustí-Panareda et al., 2014; Massart et al., 2014). The choice of the a-priori influences the retrieval result and should be chosen carefully. Comparisons of the inter-hemispheric transect with a stationary profile a-priori and the best-estimate considered CAMS-profile, revealed deviations in the order of 0.23 % for CO₂ and deviations of more than 1.5 % for CH₄ .

Since the instrumental line shape (ILS) plays a key role within this work a separate section is dedicated to this topic.

5.2 Instrumental Line Shape - ILS

The instrumental line shape (ILS) plays an important role in the retrieval. With the ILS it is possible to modify the ideal measurement for the use with real instruments. A spectrometer (regardless the type) can be described by system-theoretical considerations (Oppenheim et al., 2004). The output or system response $S(\nu)$ can be described by

$$S(\nu) = I(\nu) * T(\hat{\nu}) \stackrel{\text{def}}{=} \int_{-\infty}^{\infty} I(\nu) \cdot T(\nu - \hat{\nu}) d\hat{\nu} \quad (5.4)$$

This approach requires a temporal and spectral independent transition function $T(\nu)$. In particular this means that the shape does not change within the spectral domain and is constant in time.

³National Centers for Environmental Prediction, http://acdb-ext.gsfc.nasa.gov/Data_services/automailer/

⁴CIRA stands for “COSPAR International Reference Atmosphere”, whereas COSPAR stands for “Committee on SPACE Research”.

⁵Copernicus Atmosphere Monitoring Service data assimilation and forecasting system

	CO ₂	CH ₄	O ₂	H ₂ O
EM27 window cm ⁻¹	6173–6390	5897–6145	7765–8005	8353.4–8463.1
GRC window a cm ⁻¹	6331.30–6365.50	–	–	–
GRC window d cm ⁻¹	6213.50–6243.40	–	–	–
line list	HITRAN08 (mod)	HITRAN08	HITRAN08 (TCCON)	HITRAN09 (TCCON)
disturbing gas	H ₂ O, CH ₄	H ₂ O, CO ₂	H ₂ O	–
continuum points	40 (20)*	20	25	5
sza dependency (Θ = 80°)	≈ 0.6% (–)*	≈ 0.4%	none	not assessed
a priori profile	CAMS	CAMS	static	CAMS

Table 5.1: List of key retrieval parameters. The line lists are altered from the original HITRAN line lists where “mod” indicates a modification suggested by Lamouroux et al. (2010) to take line mixing effects into account. Likewise “TCCON” indicates a modification suggested by Wunch et al. (2011). * denotes values from the grating instrument (GRC).

As described in section 3.1 the ideal ILS of an FTS-instrument is the Fourier transformation of a box-function $T(\nu) = \mathcal{F}(\text{box}(O, O_{max}))$. Here, O corresponds to the optical path difference and O_{max} to the instrument’s maximum optical path difference. Deviations from this ideal ILS can be represented by replacing the $\text{box}(O)$ function with the modulation efficiency $m(O)$ and the phase $p(O)$.

$$\mathcal{F}(\hat{T}(O)) = \mathcal{F}[m(O) * (\sin(p(O)) + \sqrt{1-\cos(p(O))})] = T(\hat{\nu}) \quad (5.5)$$

This approach allows variations in the ILS along the spectrum. In addition the phase introduces asymmetry into the ILS in $\hat{\nu}$. This is from particular importance for the grating instrument (GRC), since off-axis effects (see section 4.3) introduce asymmetries in the intensity distribution of a point source in the image plane. Figure 5.1 shows the ILS parameters retrieved from the laser measurements (see section 4.8) for the GRC-instrument, represented by 20 parameters each. To allow for variations of the ILS over time t the modulation efficiency parameter can additionally be modified by $m_{mod}(k, t)$ via

$$m_{var}(O) = m(O) \cdot m_{mod}(O, k(t)) \quad (5.6)$$

$$\text{with } m_{mod}(O, k(t)) = 1 - \frac{k(t)}{O_{max}} O \quad (5.7)$$

This modification allows accounting for changes over time in ILS while the overall shape ILS is maintained. The GRC instrument showed a spurious variation in the retrieved product (see upcoming section). The variation in modulation efficiency as shown in Figure 5.2 could improve the result in both spectral retrieval as well as systematic deviations from the reference measurement by the EM27/SUN.

After this introductory part the trace gas retrieval results will be presented and discussed in the upcoming section.

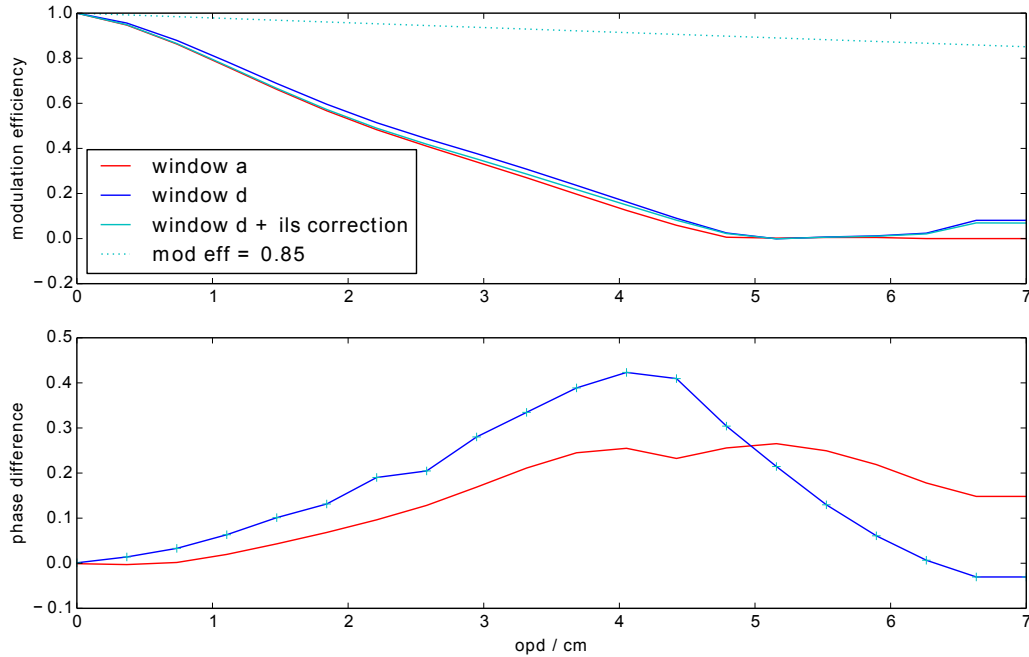


Figure 5.1: ILS-parameters used for the GRC-retrieval in dependence of the optical path difference for window a and d. Top panel shows the modulation efficiency. This modulation efficiency is additionally multiplied by the values $m_{mod}(O, k = 0.85)$ (dashed line) to allow variations in the ILS over the day (see Figure 5.2). The lower panel shows the phase shift in dependence of the optical path difference. Non-zero values introduce an asymmetric ILS. Note that there is no physical optical path difference or phase present in the GRC instrument, but PROFFIT calculates with this parameter since this program is optimized for FTS-instruments.

5.3 Trace gas retrievals from the EM27 and GRC

Both the EM27/SUN and the NIR-grating spectrograph “Ground based RemoTeC” (GRC) were taken out for a measurement campaign on the research vessel “RV *Polarstern*” as described in more detail in section 6.1. The solar tracking device for the GRC instrument was designed in very similar configuration as for the EM27/SUN device described in chapter 2. The tracker was capable to feed the solar beam into the spectrometer regardless the ships movements. In the following focus is put upon the GRC properties whereas the EM27/SUN data serves as a reference.

In total approximately 9000 atmospheric spectra were recorded from both instruments coincidentally. The GRC spectra were recorded in the measurement pattern depicted by Figure 4.8 for each of the target species (CO_2 , CH_4 and O_2). The ILS parameters as described in section 4.8 could only be retrieved in the absorption region of CO_2 and CH_4 since the laser’s tuning range from $6060\text{--}6493\text{ cm}^{-1}$ excludes the O_2 spectral region. The development of the data processing steps is a challenging task and requires specific adaptations for each micro window. Thus, the focus here is put on the retrieval of CO_2 for two reasons: First, CO_2 is less variable in the atmosphere than CH_4 and secondly, on

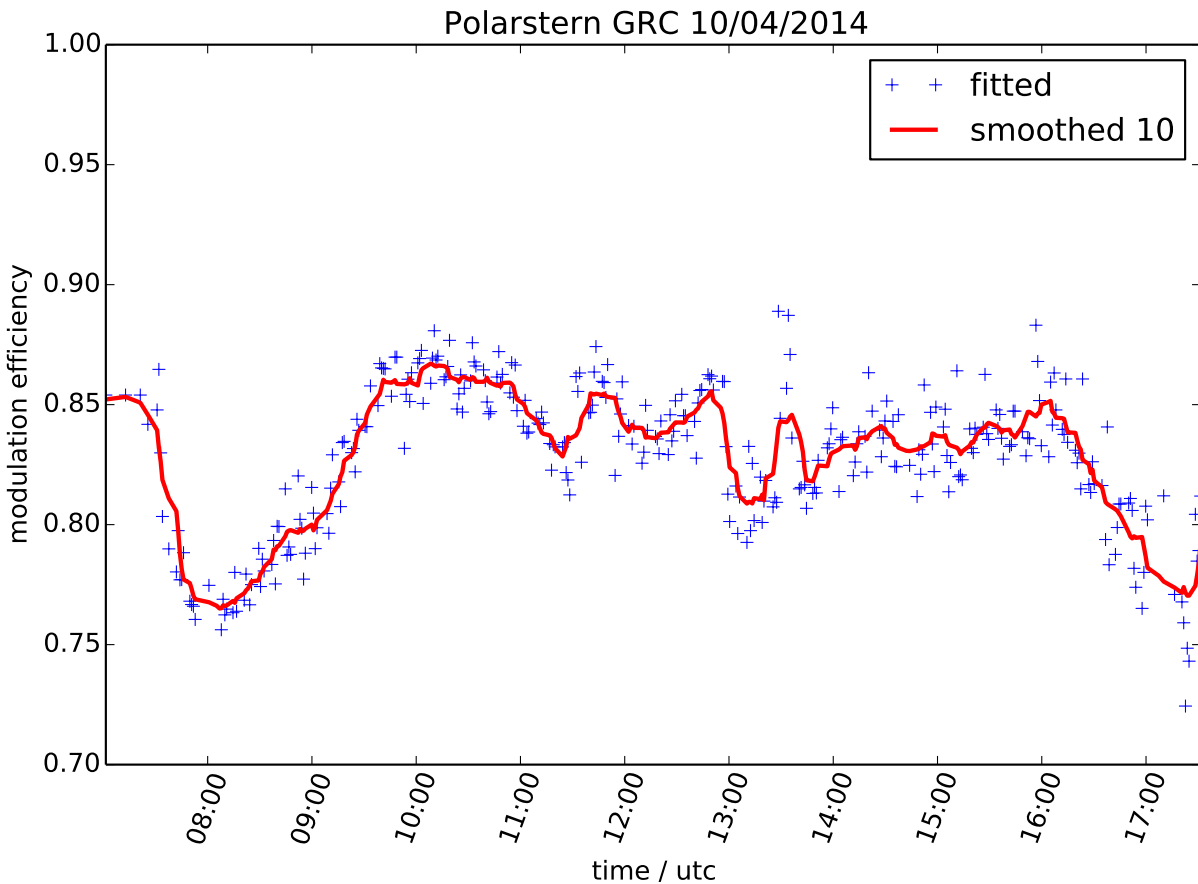


Figure 5.2: GRC modulation efficiency used for the atmospheric measurement on mar 10th 2014 on board the RV *Polarstern*. The running mean (red) is used to introduce a modification in ILS over the day for the GRC instrument.

Apr, 10th the line-of-sight passed the ships exhaust plume that created a strong signal of approximately 2ppm CO_2 in the EM27/SUN record, that measured aside the GRC instrument. Aim for the GRC instrument is to reproduce this signal accordingly.

The GRC dataset for this consecutive day is prepared as described in the previous chapter as sketched in subsection 4.5.2 including correction for detector non-linearity, dark background and detector interference from a periodic reference measurement. From this corrected spectral image, that still is in a 2-dimensional shape, the up sampling process is performed as described in section 4.7 and results into a 1-dimensional, wavenumber-calibrated spectrum. Here only the rows from 107 to 193 (vertical domain) are included in the up sampling. An increase of the number of rows does not enhance the retrieval residual. This already indicates the presence of systematic error sources instead of detector noise as a dominating source of noise. This particular vertical domain was chosen, since the standard deviation from the 10fold average of each image, indicated elevated standard deviations in the region from row 40 to 80. This calibrated spectrum then was analyzed using PROFFIT v9.6 (see section 5.1). Hereby identical atmospheric conditions for both the EM27/SUN and the GRC are taken. In especially the identical profile a-priories as well as identical pressure and temperature profiles were used for the retrievals of both instruments and

allows for a direct comparison. The ILS parameters are inferred as described in section 4.8 and altered as described in the previous section. Further retrieval setup parameters are shown in Table 5.1.

Figure 5.4 shows the spectral retrieval for a representative spectrum. The spectra from the GRC are shown left, for different evaluation setups. The corresponding spectral sections from the EM27/SUN are shown right. The measured and retrieved spectral shapes are nearly identical shown in blue and dark green. The residual $I_{measured} - I_{fit}$ is scaled by a factor of 10 in order to increase the visibility and shown in red. In addition the background intensity I_0 is shown in light blue as a free retrieval parameter for each data point '+'. Note that not the entire spectral window of the EM27/SUN is shown.

The GRC instrument shows a general higher spectral resolution than the EM27/SUN as indicated by the deeper absorption features of CO_2 . Further the number of sampling points within the spectral region is significantly higher.

The residual of the GRC is dominated by mainly two effects: A periodic pattern with a periodicity below 0.2 cm^{-1} and amplitudes in the order of 2-8% is visible in the left section of the spectral window. In addition there are sporadic systematically increased residual structures visible. The high frequent feature in the order of are likely to be a residual, non-corrected etalon interference feature (see subsection 4.6.3). The shape of the individual interference structures in the 2D spectrum (see Figure 4.20) supports this hypothesis, since the pattern aligns parallel with the entrance slit direction in the left region of the image - and thus is not averaged by the up-sampling process.

The sporadic increase of the residual, as depicted by “window-a” retrieval at approximately 6347 cm^{-1} can be correlated with solar absorption lines as Figure 5.3 shows. This hints to the presence of stray light on the detector. However, several retrievals that included various artificial broadband stray light backgrounds could not support this hypothesis. An additional candidate is the assumed Field Of View, which is used for the calculation of the solar intensity, but not investigated further within this work.

Figure 5.5 shows the retrieved CO_2 concentrations measured by the GRC over the selected day. The retrieved CO_2 total column is here derived from ground pressure since the oxygen retrieval could not be performed yet. In order to ensure a direct comparability of GRC and EM27/SUN measurements the CO_2 concentration from the EM27/SUN is derived with the same approach.

From 15:00-16:00 UTC the line-of-sight of both instruments passed the ships exhaust plume (see subsection 5.4.3) what can be clearly seen in the EM27/SUN record by enhanced values of 2 ppm. However, besides a global scaling factor the GRC evaluation deviates in the order of $\pm 5 \text{ ppmv}$ from the EM27/SUN instrument. “Window a” and “window d” show similar systematic deviations that indicate a systematic effect that is not window-dependent. Attempts to correlate this effect with the instruments internal temperatures lead not to a significant correlation.

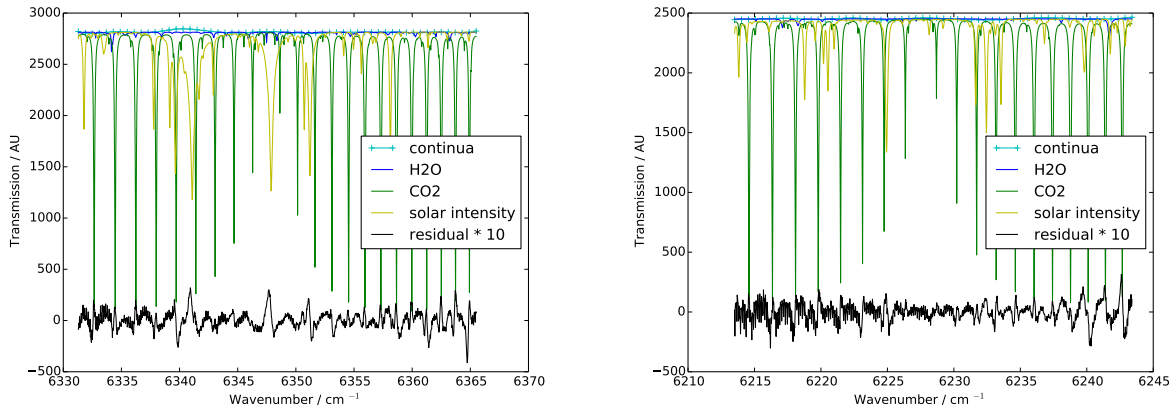


Figure 5.3: Contributions to the fitted spectrum before convolution with the ILS. The estimated continuum I_0 is shown in cyan. The transmission spectrum consists of the solar intensity (yellow) absorption lines and the absorption features of CO_2 (green) and H_2O (blue). Note the significantly broader line-width of the solar spectrum compared to the telluric lines. The increasing residual at strong solar features in combination with strong deviations in the background estimate (cyan) indicates deficiencies in connection with solar lines. Possible candidates are stray light on the detector or a deviating field of view (FOV).

A possible candidate for the variation is a variation in the ILS. The entrance slit (SLT, see section 4.4) is made of $12.7\ \mu\text{m}$ thin stainless steel. Along the slit height of $7.5\ \text{mm}$ it might be possible that this slit bends or even flips over due to thermal inhomogeneous heating effects. It is to be expected, that this will directly influence the ILS. This can be tested by implementing a broadband filter, which removes the entire visible light on the entrance slit in order to reduce the heating power. Alternatively a different slit might be chosen with lower vertical extend. This will reduce the effectively used vertical detector range. However, a retrieval with a variable ILS over the day (see Figure 5.2) increased both the residual (see Figure 5.4, bottom left) as well as the systematic scatter of the retrieval result.

5.4 Post processing

The total column average c_{gas} of the trace gas that can be obtained from the spectroscopic measurement as described in the previous section requires additional post-processing steps. First, referencing to the oxygen retrieval, second, correction of the solar zenith angle dependency and finally the calibration to the WMO-calibrated TCCON side-by-side measurements. The section closes with an approach to detect the enhanced measurements by the FTS where the instruments line-of-sight passed the ships exhaust plume and caused enhanced CO_2 measurements in order to remove these soundings from the scientific data-set.

5.4.1 Referencing to the oxygen total column

As suggested by Wunch et al. (2010) the total column average of the target gas c_{gas} in units molec m^{-2} can be referenced to the total column of the additionally retrieved oxygen total column c_{O_2} :

$$X_{gas} = 0.209420 \cdot \frac{c_{gas}}{c_{O_2}} \quad (5.8)$$

The factor of 0.209420 represents the dry molar mixing ratio of oxygen and is assumed to be constant over space (latitude, longitude) and time (see Equation 3.18). The result is typically called XCO_2 and XCH_4 and is given in molar mixing ratios parts per million (ppm) or parts per billion (ppb).

This approach is chosen to cancel out systematic spectroscopic effects. For instance a false ILS is assumed to affect both the c_{gas} as well as c_{O_2} , assuming a linear relation between the deviation in ILS and the retrieved trace gas c_{gas} . In addition deviations in the light path through the atmosphere are corrected with this common approach. Especially for satellite remote sensing, where the light path through the atmosphere might be influenced by multiple scattering effects of aerosols, this rationing gives a good estimate on the light path.

However, this approach might be questionable for ground based remote sensing in direct sunlight spectroscopy. Figure 3.5 from section 3.4 indicates that the oxygen retrieval might introduce additional errors instead of correcting for it. Spectral ghosts are likely candidates, which introduce errors in the oxygen retrieval. Ghosts are expected to be predominant in the spectral region of O_2 rather than in the spectral region of CO_2 and CH_4 and might be subject to further investigations. Despite there is no clear correlation with the water vapor present in the retrieval the O_2 retrieval might be influenced here as well by variable water vapor.

5.4.2 Dependency on solar zenith angle

Spectroscopic trace gas measurements in the NIR appear to suffer from a dependency on the solar zenith angle θ e.g. (Deutscher et al., 2010; Wunch et al., 2011). This effect seems to be a spectroscopic shortcoming with increasing air mass $A \approx \frac{1}{\cos(\theta)}$ and thus also known as “air mass dependency”. Despite the source of this effect still remains unclear, uncertainties of spectroscopic line broadening parameters or shortcomings of the Voigt line shape model are likely candidates. In addition a variation in the used a-priori profile might as well have influence on this effect. For the EM27/SUN instrument the air mass-dependency in the course of the campaign can be estimated to up to 0.6 % for XCO_2 and 0.5 % XCH_4 for solar zenith angles of up to $\approx 80^\circ$. Since the source of this effect remains unclear, a correction can only be performed on an empirical level as suggested by Wunch et al. (2011). Atmospheric measurements in vicinity of local sources and sinks, as it is mostly the case

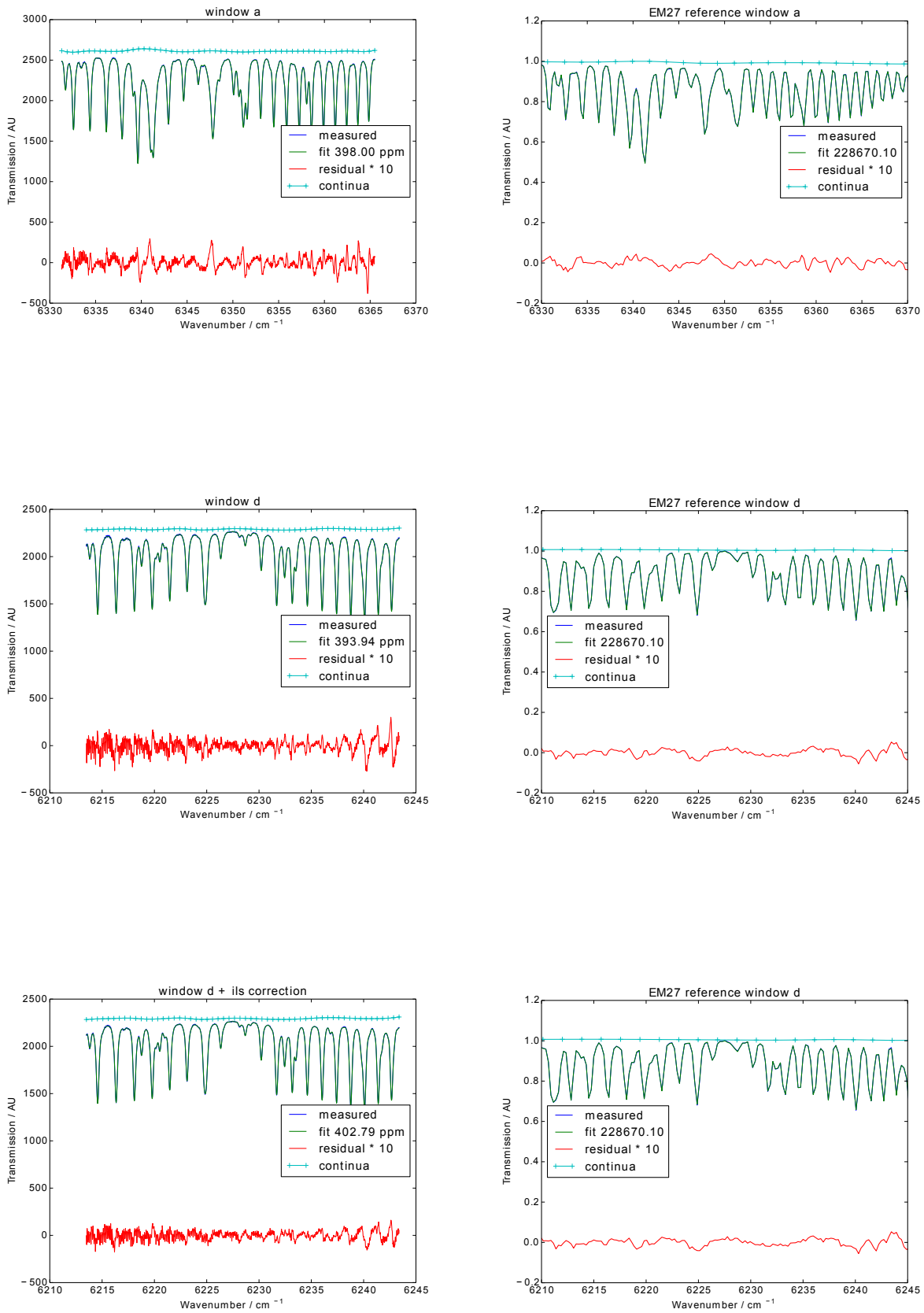


Figure 5.4: Spectral fit for GRC window d (left) including the ILS modification and the coincident window of the EM27/SUN for comparison purposes.

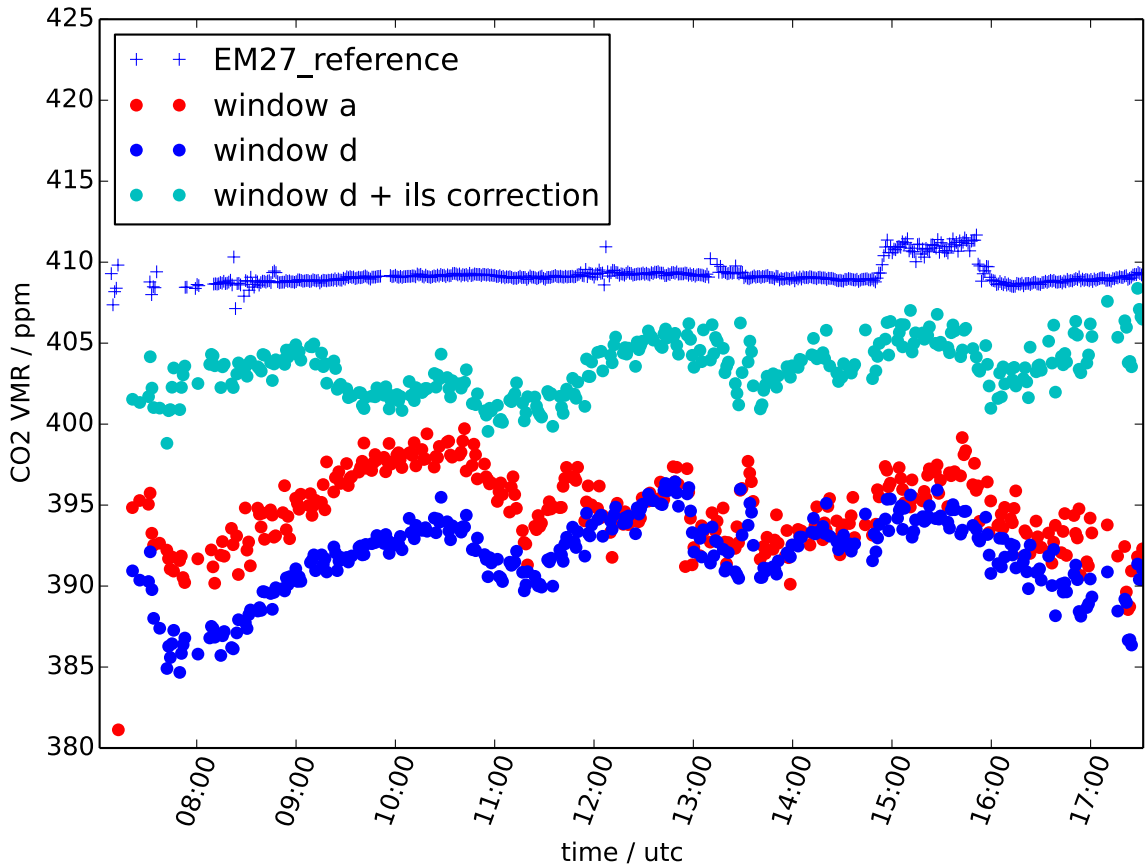


Figure 5.5: Trace gas retrieval result of the GRC (dots) for different runs. As comparison the coinciding EM27/SUN reference measurement. Two different spectral windows (a,d) are evaluated. The result could be improved towards less scatter with the variation in ILS, as tested in window d. (see Figure 5.2)

at TCCON-sites, are affected by these signals and disturb a characterization. Possible systematic dependencies might be the enhanced assimilation of CO_2 with increasing solar intensity, which in turn is a function of the SZA. Wunch et al. (2011) suggested a correction scheme that is linked to the CO_2 abundance at $\text{SZA}=45^\circ$. Two terms drive the correction: A dependency on the SZA itself and an estimate on diurnal systematic variations.

An empirical correction of the SZA dependency for XCO_2 and XCH_4 could be characterized in the course of this work for the EM27/SUN instrument. Clean oceanic air, far away from localized sources and sinks of CO_2 and CH_4 allow characterizing this effect. Remaining long-term variations from distant sources and sinks are accounted for with a separate reference to forenoon and afternoon measurements. Residual effects are assumed to be of statistical nature and average away. In the following the convention is introduced that $\theta < 0$ correspond to forenoon-measurements. The following function appeared to fit the data-set best.

$$c_{\text{SZA, gas}}(\theta) = a \cdot |\theta|^3 + b \cdot |\theta| + c \quad (5.9)$$

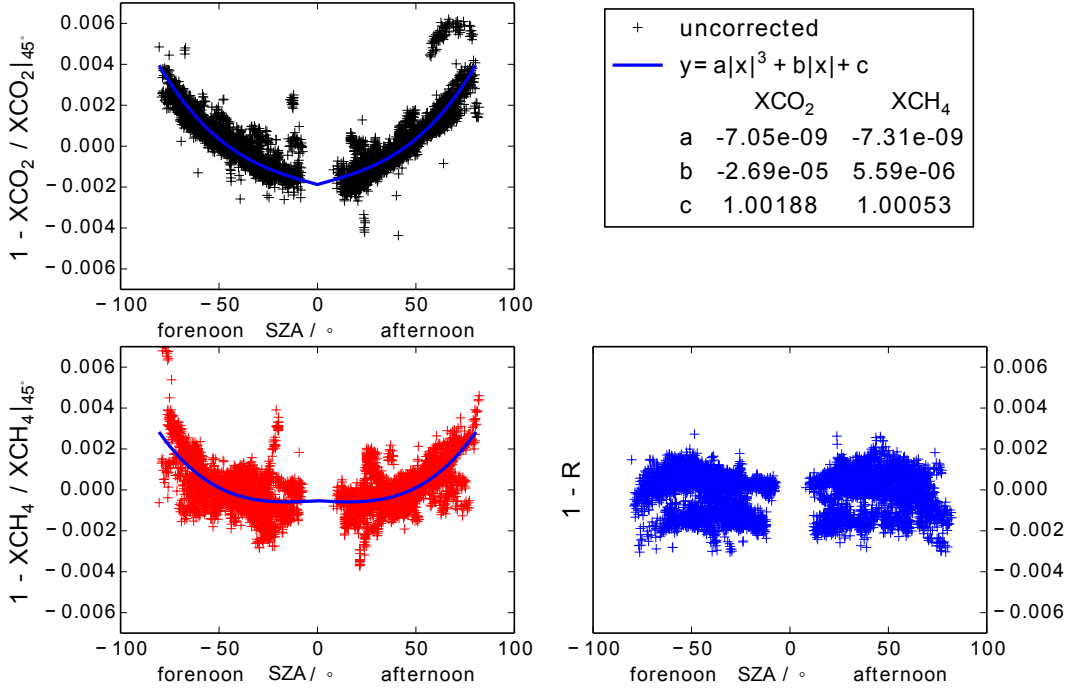


Figure 5.6: Campaign record for on-board measurements of XCO₂ (top left) and XCH₄ (lower left). This data-set is referenced to SZA=45° forenoon and afternoon separately to account for long-term variations over the day. The oxygen retrieval (lower right) appears not to be affected by the SZA dependency.

Here a , b , c are free fitting parameters. Thereby, the correction was by definition chosen to vanish at $\theta = 45^\circ$ as suggested by Wunch et al. (2011). This referencing was performed for forenoon and afternoon separately. The correction to the data-set is then applied using

$$X_{\text{SZA, gas}} = \frac{X_{\text{gas}}(\theta)}{c_{\text{SZA, gas}}(\theta)}. \quad (5.10)$$

Figure 5.6 shows the referenced data-set as well as the retrieved parameters for the correction function. XCO₂ and XCH₄ show a systematic deviation that is symmetric in SZA=0 (noon). The characteristic shape differs slightly for both gases so individual parameters are retrieved. However, oxygen, depicted in the lower left, does not show a significant SZA dependency. Note that here the reference to SZA=45 could be replaced by the reference to the measured ground pressure R (see Equation 3.18).

In summary, the spurious dependency on solar zenith angle could be characterized using the clean oceanic air, free from the effects of localized sources of CO₂ and CH₄. Systematically introduced variations due to the advection driven changes in the trace gas concentrations are assumed to cancel out each other. However, this characteristic might depend on the assumed ILS as well as on the used a-priori profile as Figure 5.7 shows.

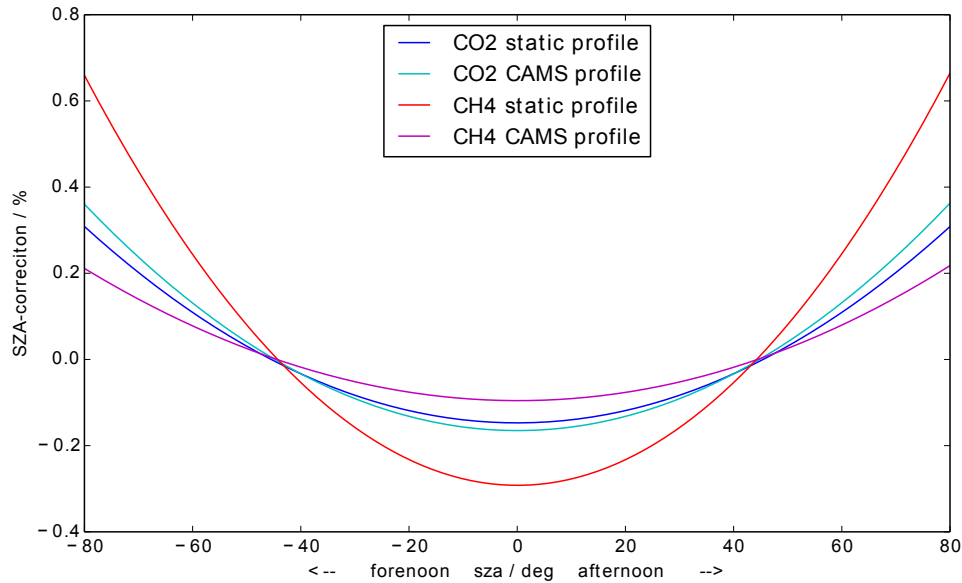


Figure 5.7: Different SZA characteristic retrieved from the RV *Polarstern* data set for CO₂ and CH₄ using a static profile a-priori or a model based a-priori. The impact on the characteristic in dependence on a-priori is especially important for the spatially variable trace gas as it is the case for CH₄.

5.4.3 Detection of ships exhaust plume

The ship's funnel was located at a few ten meters distance to the spectrometer setup and rose to approximately 12 m above deck. If the line-of-sight passed through the exhaust plume, enhancements in the observed XCO₂ are to be expected. In order to detect such observations, the enhancement pattern in the XCO₂ time series can be calculated from the line-of-sight (*los*), the prevailing wind conditions and the ship's exhaust. The ship's funnel was located at a few ten meters distance to the spectrometer setup and rose to approximately 12 m above deck. If the line-of-sight passed through the exhaust plume, enhancements in the observed XCO₂ are to be expected. In order to detect such observations, the enhancement pattern in the XCO₂ time series can be calculated from the line-of-sight (*los*), the prevailing wind conditions and the ship's exhaust.

The exhaust source flux S_s can be estimated using a simple plume model that calculates the XCO₂ enhancement E_{los} . The model takes the relative wind speed and direction between the ship-based spectrometer and the plume into account. Here a Gaussian diffusion model is used as suggested by Bovensmann et al. (2010). Defining the x coordinate as downwind direction and the y coordinate as the crosswind direction, the enhancement E_{los} along the line-of-sight can be calculated via

$$E_{los} = \int^{los} \frac{S_s}{v_{rel}} \frac{1}{\sqrt{2\pi} \cdot \sigma_y(x)} \cdot \exp\left(-\frac{1}{2} \frac{y^2}{\sigma_y(x)^2}\right) dx dy \quad (5.11)$$

where v_{rel} is the relative wind velocity between ship and plume, and the parameter $\sigma_y(x) = 0.104 \cdot x^{0.894}$ dilutes the plume in crosswind direction (y). This assumes a class C

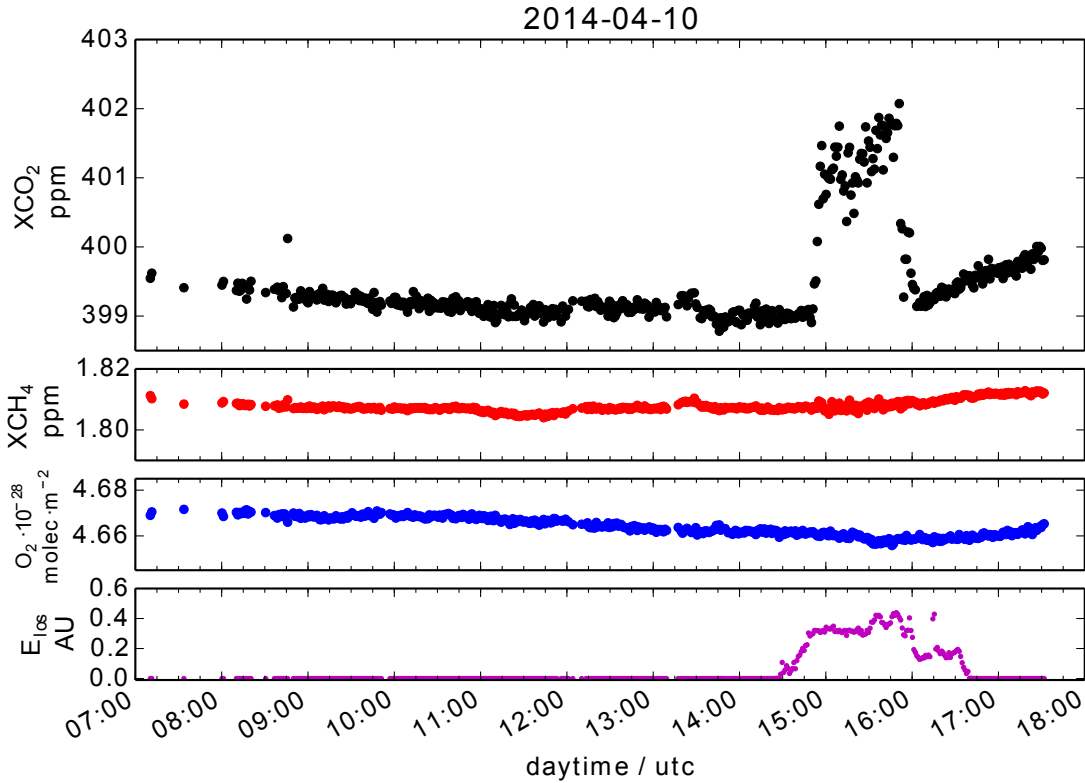


Figure 5.8: Top panel shows the time series of XCO_2 during Apr,10 2014 on board the RV *Polarstern*. The line-of-sight passed the ships exhaust plume from approximately 14:50 to 16:00 UTC and shows enhanced XCO_2 values (top panel) in the order of 2 ppm. The XCH_4 and O_2 retrieval do not show an enhancement. Affected measurements can be identified by using a simple plume model that dilutes the ships exhaust downwind. The line-of-sight integrates along this diluted plume (lower panel).

for the atmospheric stability (Bovensmann et al., 2010). At first, the exhaust flux $S_s := 1$ is given in arbitrary units. This simplifies the integration that can be performed numerically and is sufficient to use the result to flag contaminated soundings. Relative wind velocities v_{rel} and directions were taken from the records of the on board meteorological station. The line-of-sight from instrument position up to 30 m altitude above the smoke stack is projected into the downwind (x) and crosswind (y) direction and then, E_{los} is calculated by integrating numerically Equation 5.11.

Figure 5.8 shows a day where according to the lab book the line-of-sight passed the exhaust plume as confirmed by the record of relative wind velocities and directions. Measured O_2 columns and XCH_4 are not affected by the ship's exhaust, XCO_2 , however, is enhanced by up to 2 ppm. The model yields an enhancement E_{los} that is similar in temporal pattern to the observed XCO_2 enhancement that confirmed the overall applicability of the approach.

In order to remove the exhaust plume contaminated measurements from the scientific data set, a filter-threshold is set such that whenever E_{los} is larger than 0.001 the spectrum is flagged contaminated. 11.1% of the spectra were discarded by this filter. Additionally, 2.8%

Parameter	value	unit
κ	3.17	–
η	80	%
M_{diesel}	463	g s ⁻¹
v_{rel}	8	m s ⁻¹

Table 5.2: Used parameters for the plume enhancement calculation

of the spectra were rejected due to contamination by the exhaust plume after inspection by eye.

The measurement can be used to estimate the source strength using Equation 5.11. Here the source is located at $x = y = 0$ with x as the downwind component and y the crosswind component. At the location x, y the vertical column enhancement E_v in units of molec m⁻²

$$E_v(x, y, S_s) = \frac{S_s}{v_{rel}} \frac{1}{\sqrt{2\pi} \cdot \sigma_y(x)} \cdot \exp\left(-\frac{1}{2} \frac{(y)^2}{\sigma_y(x)^2}\right) \quad (5.12)$$

$$\text{with } \sigma_y(x) = 0.1040x^{0.894} \quad (5.13)$$

The source flux S in units of molec s⁻¹ is given by

$$S = \frac{\kappa \eta N_a M_{diesel}}{M_{CO_2}} \quad (5.14)$$

with κ the stoichiometric factor for the oxidation from diesel fuel to carbon dioxide, η the combustion efficiency of the engine, N_a the Avogadro constant and M_{CO_2} the molar mass of CO₂. The slant column enhancement E_{slant} can be calculated using the solar zenith angle SZA .

$$E_{slant} = E_{vert}(x, y, S) \frac{1}{\cos(SZA)} \quad (5.15)$$

Instead of a single source two smoke stacks are assumed at location $x_k = \pm 0.5$ m, $y_k = \pm 1.5$ m as it is the case for the RV *Polarstern*. The total enhancement can be calculated using

$$E_{tot}(x, y, S) = \sum_{k=1,2} E_{slant}(x - x_k, y - y_k, S_k) \quad (5.16)$$

The vessel has four engines, which release the exhaust through the two smoke stacks. These engines can run with various loads. Here the load distribution is chosen to 40% to the first and 60% to the second funnel.

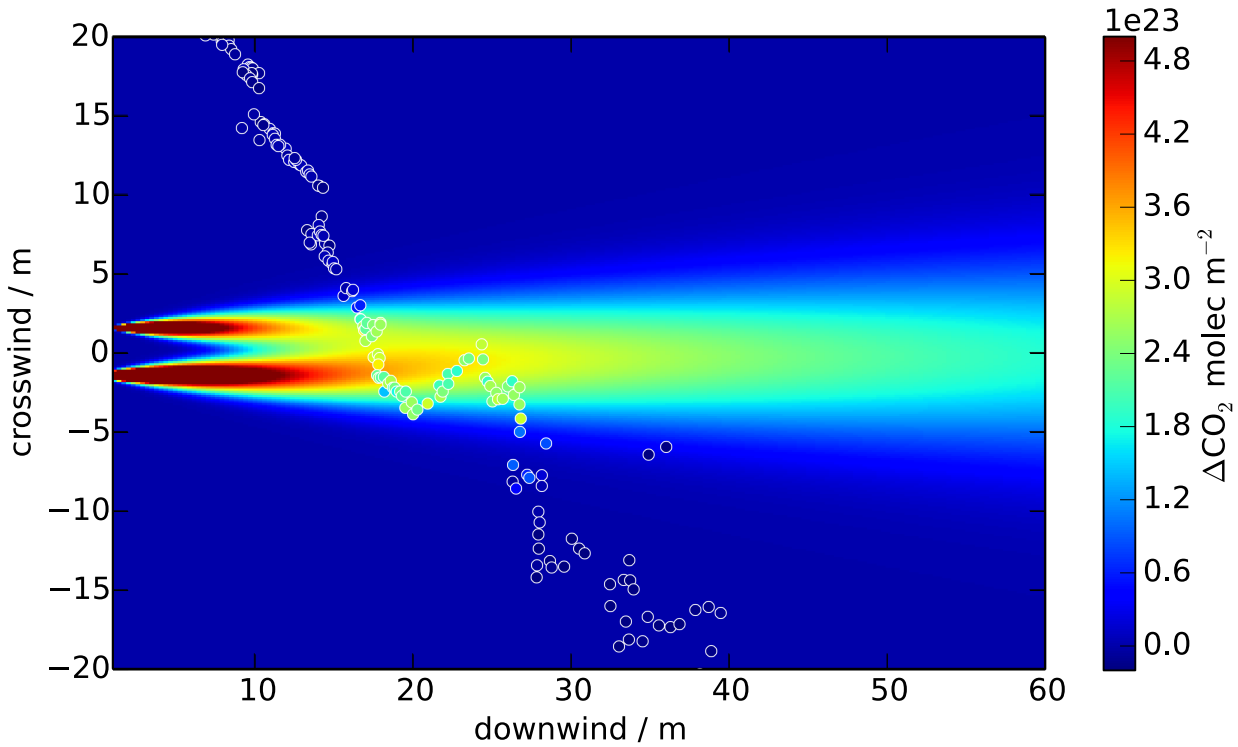


Figure 5.9: Top view of the RV *Polarstern*. The downwind direction (abscissa) and the crosswind direction (ordinate) in the inertial system of the ships funnel. The enhanced CO_2 value is calculated using Equation 5.16. The positions of the dots represent the point where the line-of-sight passed the exhaust plume approximately 10m above the funnels exit. The color code of the dot is the same as the underlying ships exhaust.

Table 5.2 shows the estimated parameters. For κ Diesel fuel is assumed to be $\text{C}_{12}\text{H}_{23}$. The Diesel flux corresponds to a fuel consumption of 40 t per day. Figure 5.9 shows the top-view on the plume with downwind direction x (abscissa) and crosswind direction y (ordinate). In color code the vertical enhancement. The dots represent a single measurement of CO_2 at the point, where the line-of-sight passed the plume in approximately 10 m above the ships exhaust plume with the same color code. Clearly an enhanced value of CO_2 aligns with the down-wind model.

The record of CO_2 over the day is shown in Figure 5.10. In red is the calculated plume enhancement shown calculated using Equation 5.16 with the parameters in Table 5.2. A 4-degree polynomial fit to all non-plume measurements give the background concentration where the enhancement is added. Note, that here instead of a global wind velocity v_{rel} the prevalent wind condition measured by the on board meteorological site is used. This model shows very good agreement to the measurement with the given assumptions. However, the fuel consumption is not exactly known, as well as the combustion efficiency. Despite these uncertainties the general approach of retrieving the source strength of a localized source can be demonstrated successfully.

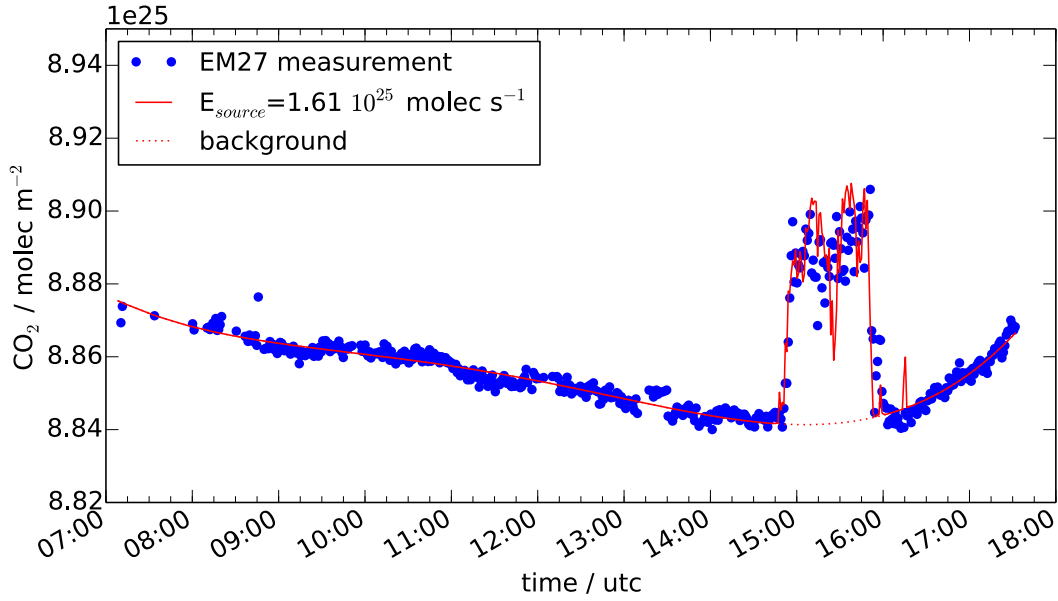


Figure 5.10: RV *Polarstern* record from Apr 10th 2014. At approximately 14:50 utc the line-of-sight passes the ships exhaust plume that result in enhanced CO_2 values. With the plume model (Equation 5.16) the source strength of CO_2 can be estimated to 40t diesel per day - a typical value.

5.4.4 Calibration to WMO reference

In order to compare the campaign data set with other products such as satellite soundings or model data, calibration to a reference is performed. Side by side measurements at the TCCON site Karlsruhe, Germany allow to constrain the campaign record to the calibrated to WMO standard according to TCCON requirements. TCCON XCO_2 and XCH_4 were retrieved with the GGG2014 software package (Wunch et al., 2011). The campaign instrument was operated side-by-side the Karlsruhe TCCON instrument during 4 consecutive days in May 2014 after the ship campaign. Retrievals from the EM27/SUN measurements followed the approach outlined in chapter 5 including the quality filters described in section 3.4 and the aforementioned correction terms. Hourly means $\langle X \rangle_h$ of the XCO_2 and XCH_4 were calculated and used to determine the calibration factor γ_{gas} according to

$$\gamma_{gas} = \left\langle \frac{\langle X_{EM27} \rangle_h}{\langle X_{wmo} \rangle_h} \right\rangle \quad (5.17)$$

where brackets indicate averaging over the entire data set. Finally, the entire EM27/SUN data set is scaled to the WMO calibrated TCCON reference with the global scaling factor γ_{gas} :

$$X_{gas,wmo} = \frac{X_{gas}}{\gamma_{gas}} \quad (5.18)$$

Figure 5.11 shows the post campaign reference measurements for both XCO_2 (top figure) and XCH_4 (bottom figure). The obtained calibration factors $\gamma_{\text{XCO}_2} = (0.99568 \pm 0.00049)$

and $\gamma_{\text{XCH}_4} = (0.98162 \pm 0.00073)$ where the error estimate refers to the standard deviation among the calibration data set. Note that the calibration factor for O_2 in the order of $\approx 2.8\%$ (≈ 0.972) was still present in the un-referenced data and is included into the calibration factor γ_{gas} . Note further, that this calibration is obtained with a reprocessed TCCON-Karlsruhe data set. This improvement was found to be necessary because the station Karlsruhe differs in the optical setup from other TCCON stations (Kiel et al., 2016). The difference can be scaled by using $\gamma_{\text{XCO}_2, \text{old}}/\gamma_{\text{XCO}_2, \text{new}} = 1.00219487$ and XCH_4 by 1.00103463.

Advances with respect to future campaigns can be made recording reference measurements before the campaign as well. This stabilizes the overall calibration and gives a handle on instrumental drift as suggested by Frey et al. (2015). However there are no indications that drift occurred along the campaign record.

In conclusion the clean oceanic air could be used to infer the spurious dependency on solar zenith angle. The applied correction might be applicable to other EM27/SUN instruments with the caveat, that there is a dependency on the used profile a-priori.

The enhancement of XCO_2 of measurements that passed the ships exhaust plume could be detected with a simple plume model. As a sanity check the source strength of the ship could be estimated to approximately 40t diesel per day. Motivated by this high accuracy, a measurement campaign at the volcano Mt. Etna, Sicily was performed Aug/Oct 2015. Here the EM27/SUN was mounted on a car and moved such, that the line-of-sight passed the plume in a cross section. Since volcanic gases contain both XCO_2 and SO_2 the total column of SO_2 had been measured as a reference with a UV-VIS spectrometer using the identical light path as the EM27/SUN instrument. The SO_2 concentrations outside the plume are negligible compared to in-plume concentrations. This allows to use the SO_2 total column as a tracer for in-plume conditions in order to derive the high atmospheric background of XCO_2 . The ratio of $\text{XCO}_2 / \text{XSO}_2$ can be used as a measure for the volcanic magma conditions (e.g. Aiuppa et al., 2007, 2010). The measurement campaign is published by (Butz et al., 2016, in preparation). The final calibration to the WMO referenced TCCON site does not show systematic deviations and allows to compare the data set with other data such as satellite or model data as described in the upcoming chapter.

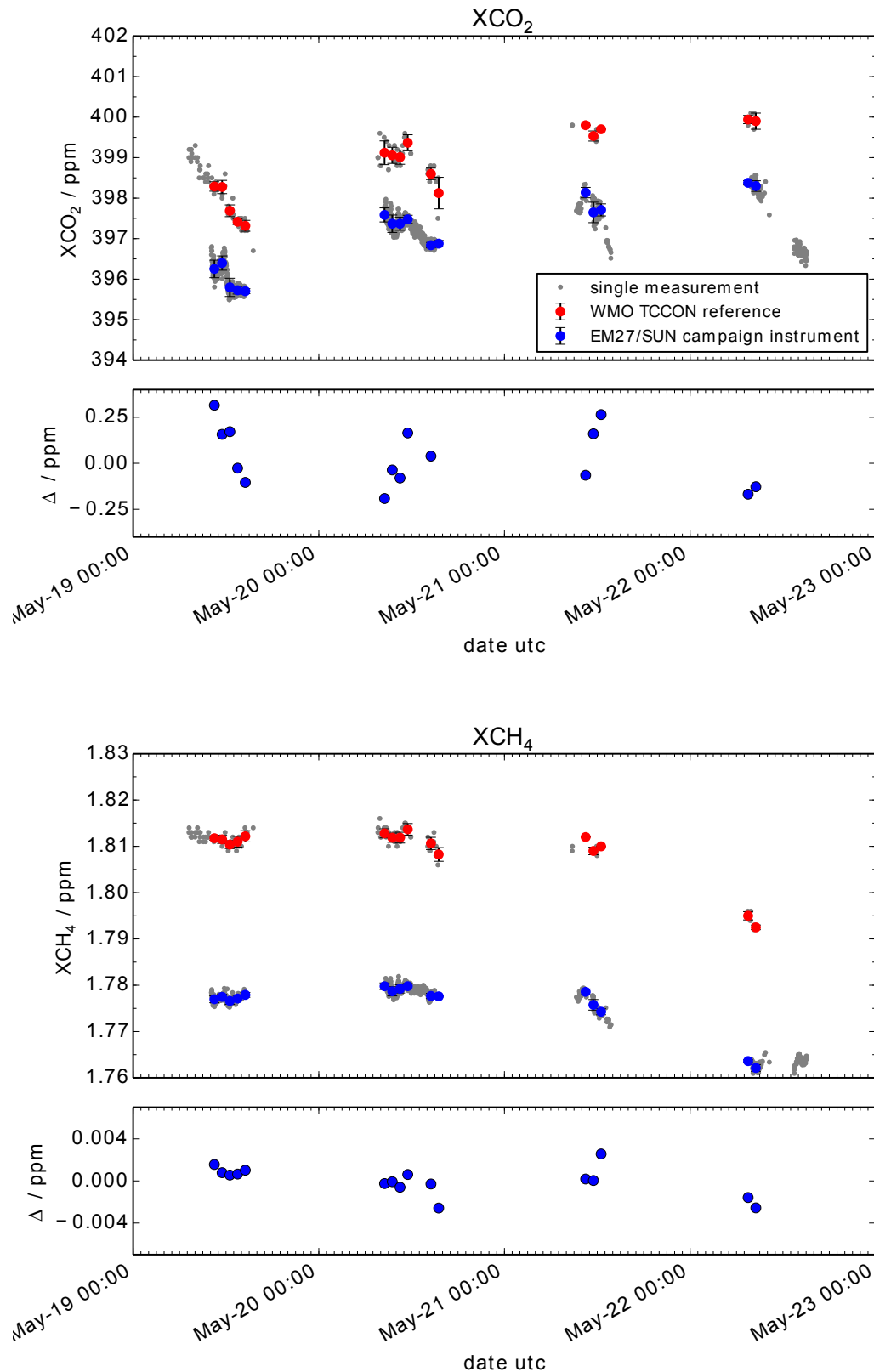


Figure 5.11: Side by side measurements with the EM27/SUN campaign instrument (blue) and the TCCON (red) site Karlsruhe, Germany. The calibration factor for XCO_2 (top figure) and XCH_4 (bottom figure) to the WMO-reference is obtained using hourly averages of each instrument. The calibration residual is shown in the lower panels of the figures and shows no systematic effect.

6 Interhemispheric transect of carbon dioxide and methane

The following chapter presents the first deployment of two miniature IR-Spectrometers on board a research vessel as mobile platform. Purpose of this campaign is, to demonstrate a general applicability of ground based direct sunlight spectroscopy from a moving platform. Besides that it delivers a consistent data set of the target species XCO_2 and XCH_4 along the interhemispheric transect with a quality beyond satellite accuracy. Parts of this chapter are from the related publication (Klappenbach et al., 2015).

6.1 Campaign description

The German research vessel “RV *Polarstern*”¹ started out at port Cape Town, South Africa (30°S, 18°E) on March 5th 2014 and arrived port Bremerhaven, Germany (54°N, 19°E) on April 14th 2014. Figure 6.1 shows the campaign outline together with the valid EM27/SUN measurements and coinciding GOSAT soundings.

Two IR-spectrometers measured on board in direct sunlight spectroscopy: The Bruker™ EM27/SUN as an IR-FTS (see chapter 3) and the self-developed grating spectrometer (GRC) (see chapter 4). The discussion focuses on the data retrieved from the EM27/SUN.

In total 5738 XCO_2 and XCH_4 total column average molar fractions could be obtained. All corrections as described in section 3.3, section 3.4 and section 5.4 are applied to the dataset. Side by side measurements at the TCCON² site Karlsruhe, Germany enabled the calibration to WMO standards in order to compare it to other data sets such as satellite soundings or model output.

For GOSAT (Greenhouse Gas Observing Satellite) three different retrieval methods are discussed: The RemoTeC-Full-Physics (FP) and RemoTeC-Proxy (Butz et al., 2011; Guerlet et al., 2013b; Schepers et al., 2012) retrieval as well as the Atmospheric CO₂ Observations from Space (ACOS) approach (O’Dell et al., 2012; Crisp et al., 2012). Even though the in-orbit operations of GOSAT have been adapted to maximize the number of ocean-glint soundings during the campaign period, the number of coincident and quality-assured retrievals amounts to a few tens of samples, that largely varied among the retrieval approaches (see subsection 1.2.2). Most importantly here, ACOS delivers many more data than RemoTeC-FP for ocean-glint soundings since RemoTeC-FP resorts to a conservative

¹Operated by the Alfred Wegener Institute (AWI), Helmholtz Centre for Polar and Marine Research

²Total Carbon Column Observatory Network

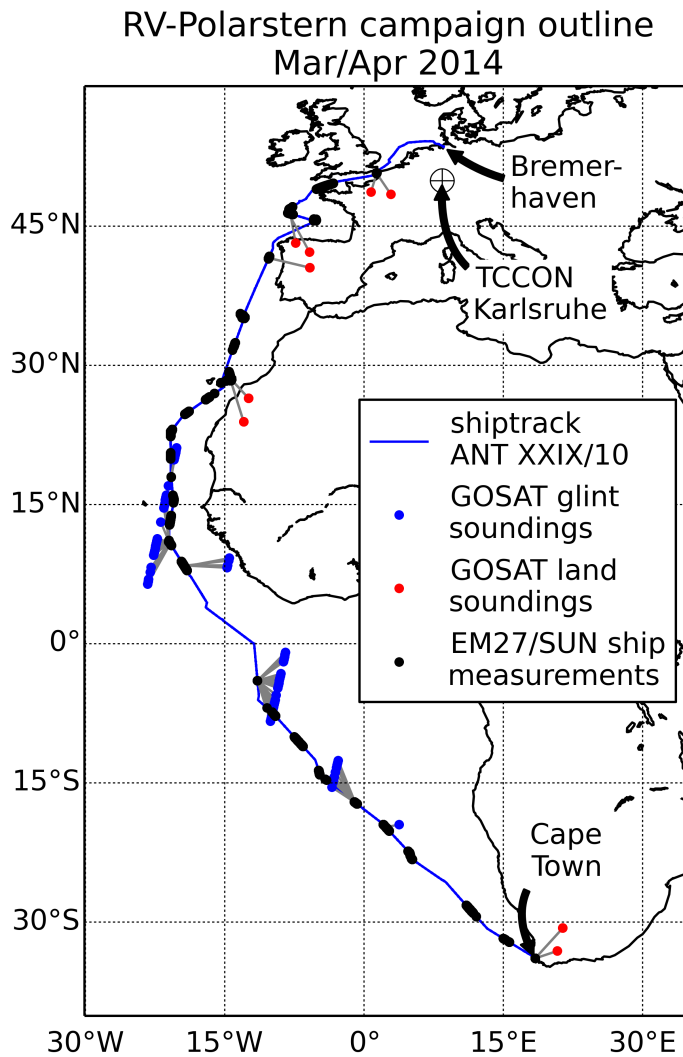


Figure 6.1: Ship track of the RV *Polarstern* during the cruise from Cape Town Mar 5th and port Bremerhaven Apr 14th 2014. GOSAT soundings that found to be coincident within a 5° radius and 4hour temporal radius are interconnected with gray lines.

cloud and aerosol filtering scheme using the “upper edge” method (Butz et al., 2013). ACOS does not deliver XCH_4 .

Satellite soundings were correlated to RV *Polarstern* records with a 4 h temporal and with a 5° latitudinal/longitudinal coincidence radius. Figure 6.1 depicts this coincidence criterion connecting RV *Polarstern*-measurements (black) with satellite soundings (blue = ocean glint; red = land-nadir). It is to be expected, that this coincidence criterion introduces a large uncertainty, since real variations in total column averages may occur (see subsection 1.2.2).

The model data by CAMS (Copernicus Atmosphere Monitoring Service) provides global operational analysis and forecast of CO_2 and CH_4 in near real time. The model output is a forecast without any data assimilation of the target species with a horizontal resolution of around 80 km and 60 vertical levels from surface to 0.1 hPa. The atmospheric CO_2

and CH₄ mixing ratio fields modeled by CAMS rely on the ECMWF IFS model³. The IFS has a simple carbon module (Boussetta et al., 2013) to model the CO₂ uptake and release from vegetation. The CO₂ biogenic fluxes from vegetation are adjusted to correct for large-scale biases by using a climatology of optimized CO₂ fluxes (Agusti-Panareda et al., 2015, ECMWF Tech Memo 2015). The CH₄ fluxes and other CO₂ fluxes are prescribed by inventories and seasonally varying climatologies, including the chemical sinks for CH₄ in the troposphere and stratosphere. A more detailed description of the CO₂ and CH₄ forecast configuration can be found in Agustí-Panareda et al. (2014) for CO₂ and in Massart et al. (2014) for XCH₄. The plotted data stems from the model simulation where the meteorology is re-initialized daily using ECMWF meteorological analyses but CO₂ and CH₄ are free running, i.e. no assimilation of CO₂ and CH₄ observations is performed. The model data is temporally and spatially interpolated from model grid to the RV *Polarstern* measurements in order to avoid discontinuities. The profile a-priori used in the retrieval of the RV *Polarstern*-dataset was taken from the same CAMS model data. Thus effects of the averaging kernel are assumed to be negligible (Klappenbach et al., 2015; Rodgers and Connor, 2003) which allows a direct model-measurement comparison.

6.2 XCO₂ and XCH₄ - inter hemispheric transect

Figure 6.2 and Figure 6.4 show the EM27/SUN XCO₂ and XCH₄ records measured above the Atlantic in March/April 2014 from aboard RV *Polarstern*. XCO₂ represents the North–South (N–S) gradient of up to 6.8 ppm between $\sim 45^\circ$ N and $\sim 30^\circ$ S at the end of the Northern Hemisphere dormant season. This is largely expected from previous assessments (e.g. Denning et al., 1995). Beside the N–S gradient, diurnal and day-to-day variations on the order of 1 ppm are found most likely originating from transport of far-away source/sink signals. Note that the exhaust of RV *Polarstern* itself were excluded from the data (see subsection 5.4.3).

Satellite data from GOSAT as well as globally modeled CO₂ and CH₄ by CAMS is shown as well.

Figure 6.3 and Figure 6.5 show the differences of the various greenhouse gas products to the campaign record. Here averages of all EM27/SUN soundings within the coincidence criteria were subtracted from the individual satellite soundings.

Both GOSAT XCO₂ retrievals, RemoTeC-FP and ACOS, generally match the EM27/SUN observations within 2 ppm. Due to sparse data coverage, RemoTeC-FP does not allow for assessing the N–S gradient. The ACOS retrievals tentatively show a weaker N–S gradient due to XCO₂ land-nadir soundings North of 23° being somewhat lower than the ship records. Scatter of the satellite data, however, hinders robust conclusions.

The XCO₂ modeled by CAMS shows an overall excellent agreement to our ship-borne records. In the northern extra tropics an offset of 1 to 2 ppm is consistent with an independent

³<https://software.ecmwf.int/wiki/display/IFS/Official+IFS+Documentation>

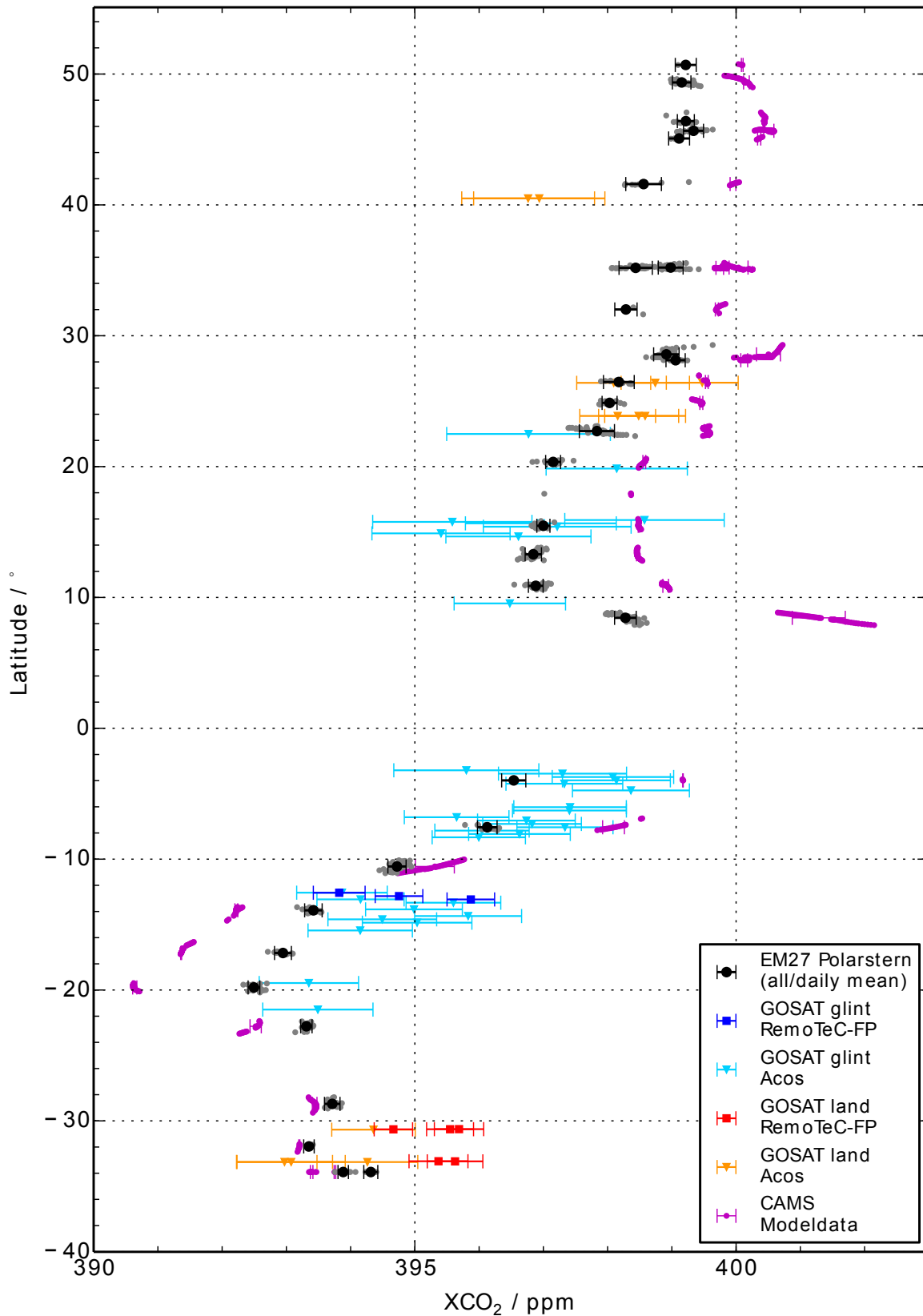


Figure 6.2: Atmospheric carbon dioxide concentrations (XCO_2) retrieved from ship based measurements in infra-red direct sunlight spectroscopy from onboard the research vessel RV *Polarstern*. This latitudinal transect shows the retrieval result (gray dots) as well as daily averages (black). Satellite evaluations from GOSAT data are shown for two retrieval approaches (Acos and RemoTeC-FP) separated by ocean glint geometry (bluish) and land-nadir soundings (reddish). In addition non-assimilated CAMS model-data is shown (magenta).

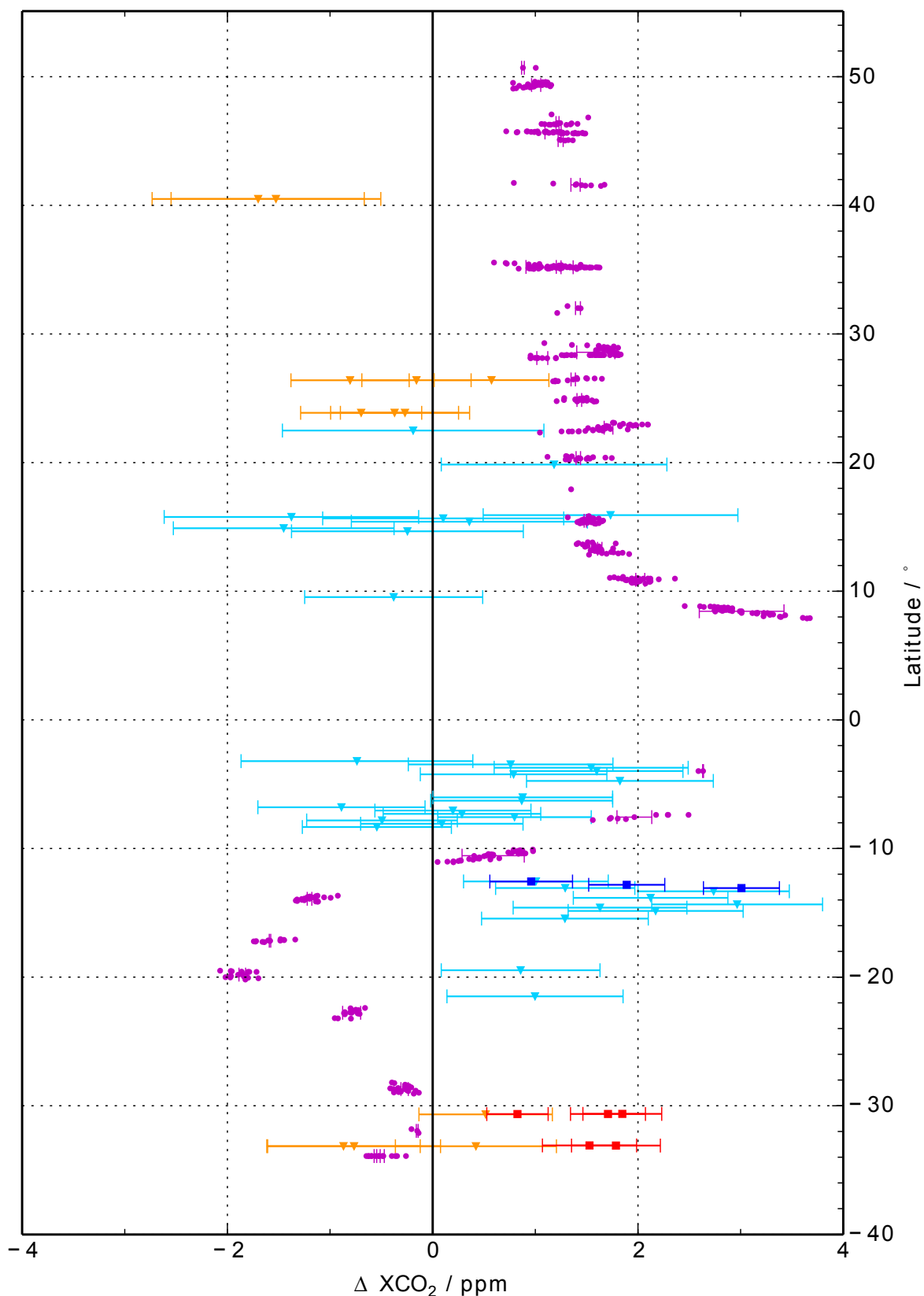


Figure 6.3: Differences $X-X_{EM27}$ are shown for the different data-sets. Satellite data are compared to the average of coinciding ship based measurements. The differences do not show a systematic deviation for the satellite products. Most of the differences might be introduced by the coincidence criterion and do not appear to show a clear trend. Modeled data however, show a discrepancy of approximately 1 ppm in the interhemispheric gradient as well as a general offset. In addition the deviation increases towards the tropical convergence zone at the equatorial region.

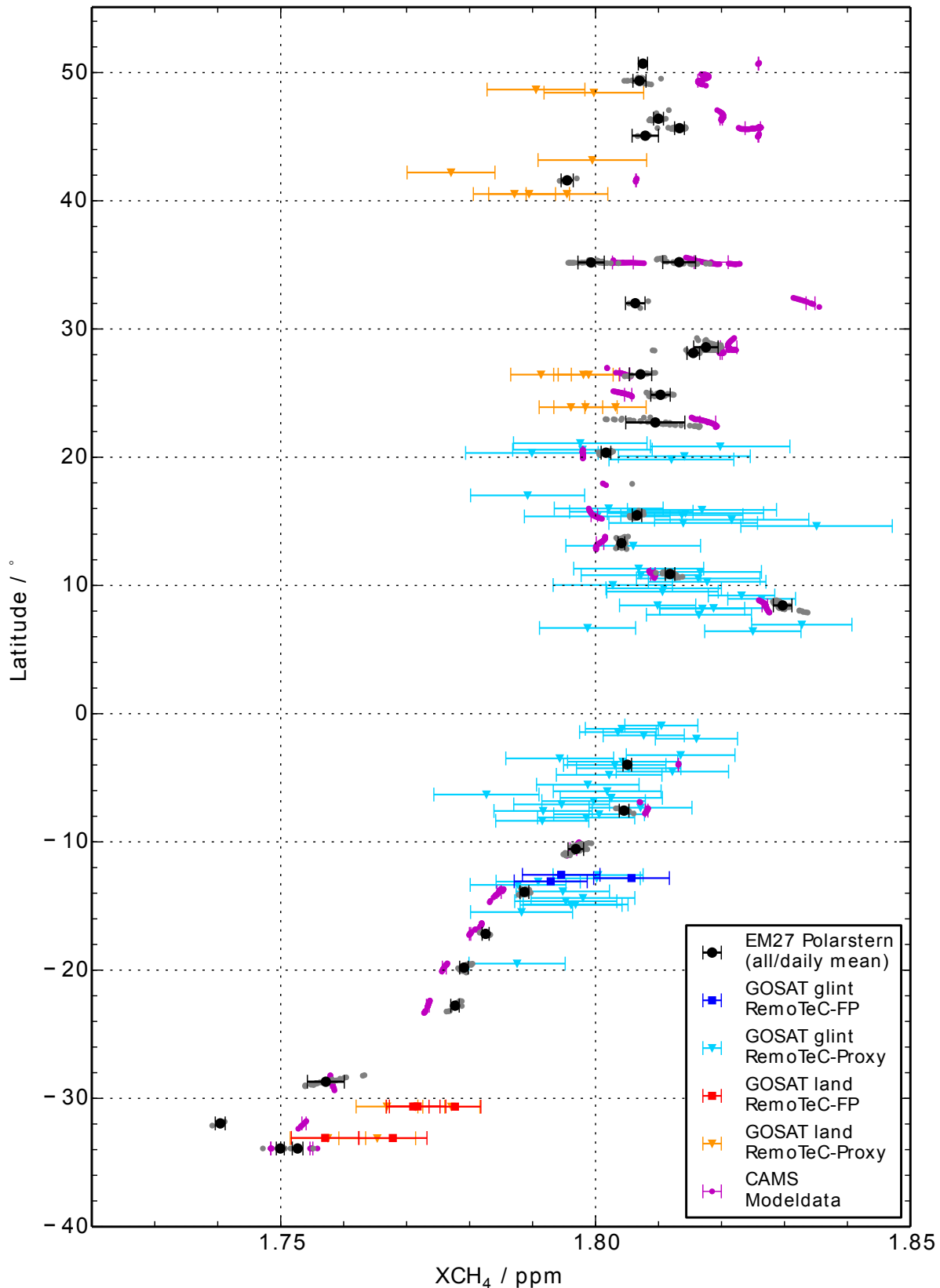


Figure 6.4: Atmospheric methane concentrations (XCH_4) retrieved from ship based measurements in infra-red direct sunlight spectroscopy from onboard the research vessel *RV Polarstern*. This latitudinal transect shows the retrieval result (gray dots) as well as daily averages (black). Satellite evaluations from GOSAT data are shown for two “RemoTeC” retrieval approaches (FP and Proxy) separated by ocean glint geometry (bluish) and land-nadir soundings (reddish). In addition non-assimilated model-data is shown (magenta).

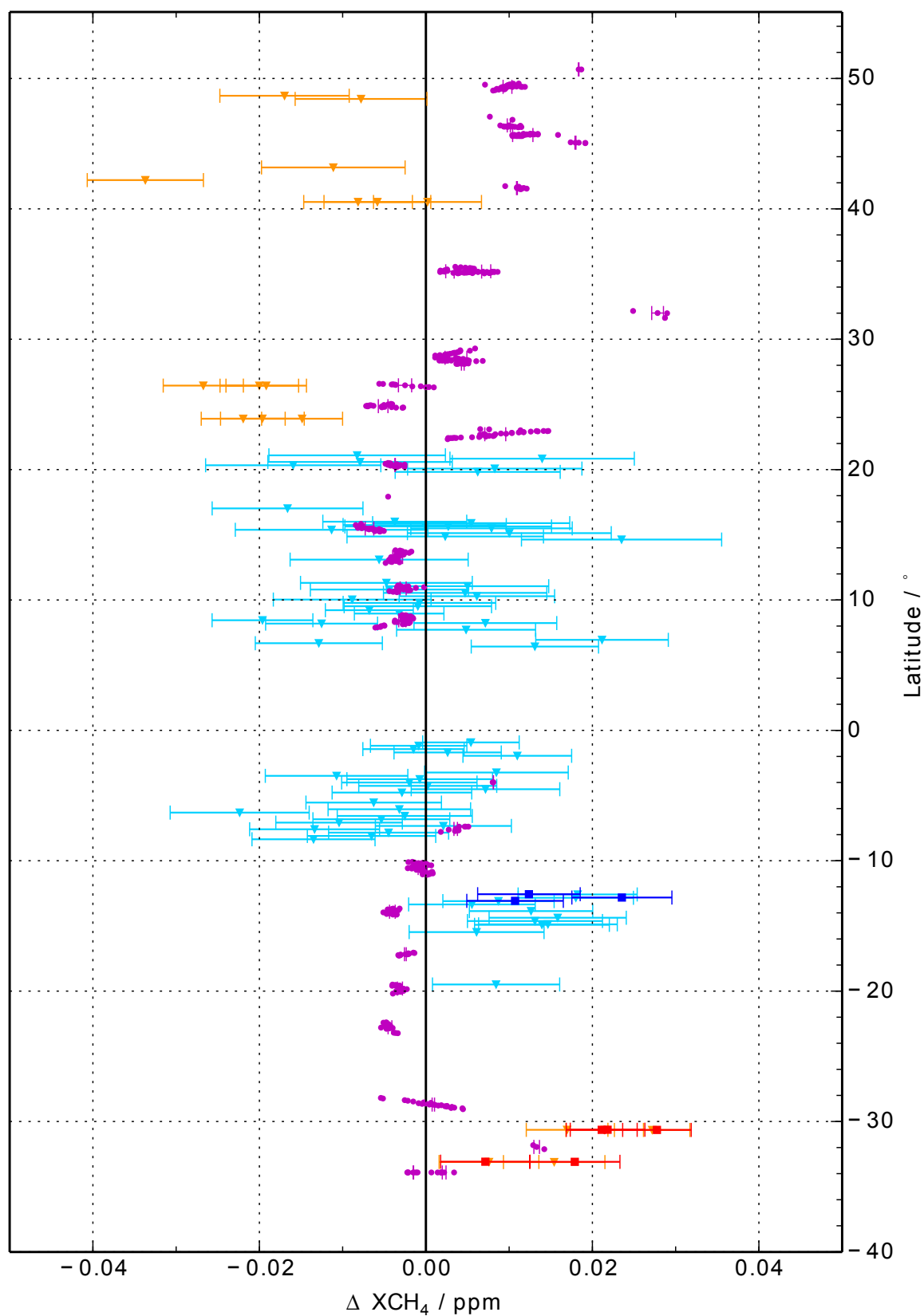


Figure 6.5: Differences $X-X_{EM27}$ are shown for the different data-sets. Satellite data are compared to the average of coinciding ship based measurements. Satellite data indicate no significant systematic deviation. Largest deviations occur at land-nadir soundings (reddish colors) and might be differences introduced due to spatial distances.

evaluation (Agustí-Panareda et al., 2016, submitted) using TCCON data at several sites in the Northern Hemisphere extra tropics. This model bias is linked to errors in the modeled CO_2 fluxes which will be addressed by the CO_2 flux adjustment scheme under development in the CAMS forecasting system. Despite this model bias, the small variations introduced by transport processes can be resolved by both model and measurements. Differences are larger in the tropics where XCO_2 is overestimated by the model. It is clear that the model is not able to represent accurately the CO_2 emissions from West Africa characterized by widespread biomass burning. Due to persistent cloud cover the ship records lack data in the inner tropics that hinders further investigation of this source related error. Smaller discrepancies of less than 1 ppm are found in the Southern Hemisphere background air. The smoothing effects introduced by the averaging kernel matrix are directly taken into account due to the use of the model a-priories for the spectral retrieval. These effects are larger in the northern extra tropics and tropics, but are found to be negligible in the southern extra tropics. For XCH_4 model-measurement deviations are below 0.02 ppm for most of the cases. The discrepancies are also larger in the northern hemisphere where XCH_4 fluxes are strongest, but the relative differences are much higher than for XCO_2 .

For XCH_4 , Figure 6.4 (right), the EM27/SUN soundings find a N–S gradient of roughly 0.06 ppm between $\sim 45^\circ \text{N}$ and $\sim 30^\circ \text{S}$. Diurnal and day-to-day variability on the order of 0.01 to 0.02 ppm can be observed around 30°S 35°N . Tentatively, latitudinal variability in XCH_4 and XCO_2 follows similar patterns. For example, one might speculate whether XCO_2 and XCH_4 increasing towards the Northern tropics ($\sim 10^\circ \text{N}$) are related to emissions of both gases from biomass burning. Though, the inner tropics lack data to confirm that hypothesis.

The GOSAT RemoTeC-FP and RemoTeC-Proxy XCH_4 retrievals, both agree with the ship-borne records to mostly within 0.02 ppm. As for XCO_2 , the yield from RemoTeC-FP is too low to infer robust conclusions but overall RemoTeC-FP delivers XCH_4 offset in the order of 0.01 to 0.02 ppm compared to RemoTeC-Proxy retrievals. The latter fit the validation data particularly well for the tropical ocean-glint soundings. The land-nadir soundings North of 23°N show greater differences of 0.03 to 0.04 ppm i.e. both, RemoTeC-Proxy XCH_4 and ACOS XCO_2 , reveal larger differences for the Northern mid-latitude land-nadir observations than for the low-latitude ocean-glint soundings. Given that both algorithms and both species are affected, the most likely explanation is that our coincidence criterion is too loose to assume homogeneous concentration fields in the mid-latitudes.

Overall, the deployment of the EM27/SUN spectrometer on RV *Polarstern* demonstrated that the inferred latitudinal transects of XCO_2 and XCH_4 were of adequate quality to validate soundings from satellites such as GOSAT and to evaluate modeled concentration fields such as provided by the CAMS model. The observations collected during our ~ 5 week campaign are too sparse to allow for a statistically robust ensemble of coincidences with GOSAT but demonstrated the potential for providing satellite validation over the oceans where other validation opportunities are sparse. Already a few ship cruises, similar to the

one discussed here, conducted per year would make a great asset to for XCO₂ and XCH₄ remote sensing from satellites in particular for satellites such as OCO-2 providing much denser data coverage than GOSAT. Despite the snapshot-like nature of our observations, the comparison of the ship records to the CAMS model provided hints at model errors in the CO₂ and CH₄ surface fluxes and model deficiencies in the representation of the chemical sink for XCH₄ in tropical regions. Simultaneously comparing measured and modeled XCO₂ and XCH₄ delivers additional confidence in the conclusions since transport related errors are correlated among the two species, thus helping in the model flux/transport error source attribution.

6.3 Hemispheric source strength - use of a simple box model

An interhemispheric gradient of CH₄ measured with high accuracy can be used to derive the relative source strength of CH₄ for each hemisphere. The source strength S_H of one hemisphere H can be represented by a simple box model similar to the suggestion by Elkins et al. (1993) where the atmosphere is divided into the two hemispheres:

$$S_H = \frac{dX}{dt} + \kappa_{loss}X + \kappa_{exch.}(X_H - X_{\hat{H}}) \quad (6.1)$$

Here X denotes the trace gas concentration in the specific hemisphere H . The source strength S is given by the change in concentration in time modified by removal processes (κ_{loss}) and inter hemispheric gradient driven exchange ($\kappa_{exch.}$) from the other hemisphere \hat{H} . $\kappa = \frac{1}{\tau}$ with the average lifetime τ .

Under the assumption that the exchange found its equilibrium state $\frac{dX}{dt} = 0$. The inter hemispheric exchange coefficient can be estimated from long lived SF₆ (Sulfur hexafluoride) to $\kappa_{exch.} = \frac{1}{1.3 \pm 0.1} \text{ yr}^{-1}$ (Geller et al., 1997). In particular this means an atmospheric molecule needs statistically 1.3 years to pass the inner tropical convergence zone to the other hemisphere.

The relative source R_H contribution from each hemisphere thus can be estimated using the measured inter hemispheric gradient:

$$R_H = \frac{S_H}{S_H + S_{\hat{H}}} \quad (6.2)$$

The lifetime of CH₄ is $\tau = 9.1 \pm 0.9 \text{ yr}$ (Prather et al., 2012). Here, the lifetime defined as the total atmospheric burden divided by all loss processes.

From the measurement (see Figure 6.4) the inter-hemispheric gradient can be estimated to $[\text{CH}_4]_{\text{NH}} = (1.7545 \pm 0.0049)$ ppm and $[\text{CH}_4]_{\text{SH}} = (1.8099 \pm 0.0066)$ ppm which leads to a source contribution of (61.9 ± 2.4) % for the northern hemisphere.

The net removal of atmospheric CO_2 takes place by mainly two processes: Biogenic net uptake and oceanic invasion⁴. Due to individual response times of these processes a general lifetime of atmospheric CO_2 cannot be specified and thus does not allow such an assessment for CO_2 .

However, this simple box-model depicts the working principle of the top-down approach. With respect to more sophisticated models this data set can be used to infer model inaccuracies as depicted in the upcoming subsection, even if these models do not infer source or sink budgets.

6.4 Model improvements with the measured north-south transect.

The global CAMS forecast model for CO_2 and CH_4 is an advection based model that uses source and sink repositories in combination with an transport model (Agustí-Panareda et al., 2014; Massart et al., 2014). Here, the Integrated Forecasting System (IFS⁵) is used, which is a semi-Lagrangian non mass conserving transport scheme. The error increases with higher model-resolution. This is of particular importance for long-lived species such as CO_2 and CH_4 since these errors accumulate with model-time. The measured highly accurate and representative data set obtained within this work can be used to identify these effects and constrain correction approaches to it.

Figure 6.6 shows on the left hand side the RV-*Polarstern* track and daily average position. The two right panels show model improvements compared to the RV-*Polarstern* data set (black) for both CO_2 and CH_4 respectively. In general deviations increase with higher model resolution depicted by light colors as to be expected. Two different correction approaches are shown in blue and green. A simple “proportional” mass fixer (Agustí-Panareda et al., 2014; Massart et al., 2014) as well as the more complex Bermejo & Conde mass correction approach (Bermejo and Conde, 2002). Besides the general offset between measurement and model, both correction schemes alter inter-hemispheric gradient as well and correct it towards the measured transect. Satellite measurements can deliver such a transect, but they are too in-accurate to assess the inter-hemispheric gradient. Stationary sites, on the other hand, are accurate, but sparsely spread over the globe. In addition station-to-station variations due to different instruments and measurement conditions do not allow such an assessment which makes the RV-*Polarstern* data-set a valuable contribution for model improvements.

⁴Note, that here are additional, long-term $\mathcal{O}(10^4\text{yr})$ processes.

⁵For more information see <https://software.ecmwf.int/wiki/display/IFS/Official+IFS+Documentation>, last access Jul 14th 2016

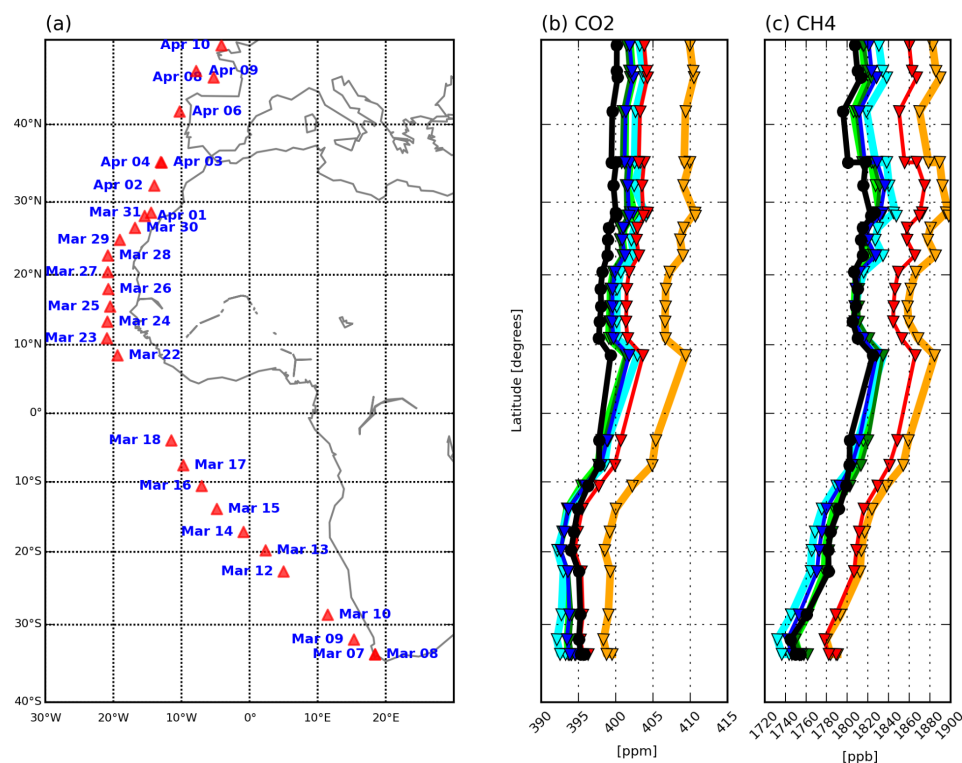


Figure 6.6: Right two panels depict the step-wise model improvements of the CAMS CO₂ and CH₄ forecast product using the RV-*Polarstern* data set (black). High resolution model runs are shown in light colors, low resolution in dark colors. The improvements address the non-mass-conserving transport model, which affects high resolution runs more than low resolutions. No correction is depicted by red/orange lines. Including two different corrections (green/blue) decreases model-measurement deviations. Note, that beside a global offset, the correction alters the inter-hemispheric gradient as well. Picture taken from (Agustí-Panareda et al., 2016, Submitted).

6.5 FTS versus Grating Spectrometer

Within this work two IR-Spectrometers with similar resolving power had been tested for the use of campaign based mobile measurements of atmospheric CO₂ and CH₄ in direct sunlight spectroscopy. The EM27/SUN as an Infra-Red-Fourier-Transform-Spectrometer and a self developed IR-Grating spectrometer (GRC). The EM27/SUN shows excellent performance even under mobile application on board a ship including moderate engine induced vibrations. Sampling-times in the order of 12s for a double sided interferogram appear suitable for stationary and ship-based measurements. However, shortcomings show off under more mobile applications such as car-based measurements with strong vibrations causing sampling related errors and stopped recording (personal communication André Butz). Despite the GRC has not been tested on car-based applications, it can be expected that a grating spectrometer should not suffer from such effects. In addition extremely short integration times compared to the FTS instrument allow to relax the solar tracking requirements as well as performing measurements under highly variable atmospheric conditions. For accurate

parameter	GRC	EM27/SUN	unit	annotation
focal length f	508.0	127.0	mm	
aperture diameter d	40.0	0.6	mm	
numerical aperture	20.0	200	–	
external field of view	0.346	0.270	°	full angle
design wavelength	900 – 1700	850 – 2000	nm	
design wavenumber	900 – 1700	5,000 – 12,000	cm ⁻¹	
resolving power	29,000	12,000	–	
integration time	0.25	12	s	
dimensions	85 x 37 x 26	35 x 27 x 40	cm	L x W x H
weight	≈ 18	≈ 25	kg	
power consumption	≈ 100 (150 peak)	≈ 100	W	plus laptop
precision in XCO ₂	0.4	0.03	%	relative to 400 ppm
precision in XCH ₄	–	0.04	%	relative to 1750 ppb

Table 6.1: Key parameters of the two NIR-spectrometers.

measurements the instruments stability has to be improved further as depicted in section 4.9 in order to compete with the EM27/SUN properly. Table 6.1 summarizes the instruments properties accordingly.

7 Conclusion and outlook

This work contributes to the scientific understanding of sources and sinks for atmospheric carbon dioxide (CO_2) and methane (CH_4) on a continental or local scale. As part of the “top down” approach, which infers the source/sink strengths from accurate and representative measurements, ground based remote sensing approaches are used to measure trace gas concentrations as a column average of the entire atmosphere overhead. This technique can be both accurate *and* representative. However, only a few tens of instruments operate worldwide on a regular basis which hinders stable source/sink evaluations. This work aims to perform mobile and accurate remote sensing measurements in order to increase the spatial density of measurements worldwide. Within this work two packing-case sized near-infra-red spectrometers were tested on a research vessel in direct sunlight spectroscopy, one of which was a self developed grating spectrometer. A solar tracking system, also developed within this work, couples the solar intensity reliably into the spectrometer’s entrance apertures, regardless the ship’s movements. The obtained campaign data was evaluated and published (Klappenbach et al., 2015).

The performance analysis of the developed solar tracking device revealed an accuracy of 0.05° for angular accelerations up to 6.3°s^{-2} and showed excellent performance for ship based applications with typical angular accelerations well below the inferred limit. Future developments can drive the fitness of the solar tracker towards car-based measurements and would enable so called “traverse” measurements, by passing a localized source of trace gases. In-plume and out-of-plume measurements during such a traverse allow to quantify background concentrations and to infer the source enhancement directly. Sources might be a city, volcano, ruminant based livestock or shale-gas facilities to name just a few. Especially the latter are subject to scientific debates since the sources are diffuse and challenging to characterize (e.g. Howarth et al., 2011; Schneising et al., 2014).

A major part of this work was the development of a NIR-grating spectrometer motivated by the physical robustness of such instruments. Besides conventional gratings, an “immersed grating” was tested. Despite the excellent dispersion that would have allowed decreasing the physical dimensions of the instrument by a factor of 2-3, the conventional grating setup was the finally implemented one. Key feature of this instrument was the used 2D detector array in order to enhance the spectral sampling. The evaluated precision of 0.4% for XCO_2 was limited by instrumental effects, mainly shortcomings of the detector. However, compared to the FTS-instrument, approximately 50 times shorter exposure times could guarantee measurements under very variable conditions. For future instruments the use of a strictly linear detector is strongly recommended, that must not be subject to additional

interference phenomena in the detectors substrate. Modifications are indicated within this work for the future use of an immersed grating, which might be a considerable choice for a small instrument with a high resolving power. Future applications might be a grating spectrometer without moving parts, which uses three detectors that resolve the absorption features of CO_2 , CH_4 and O_2 simultaneously, resulting into extremely short integration times to make a step towards car-based measurements.

The Infra-Red-Fourier-Transform-Spectrometer “EM27/SUN” by BrukerOptics could already prove high precision and long term stability in stationary ground based measurements. This work demonstrated, that the sensitive mechanics of this lab-instrument was not challenged by campaign based measurements on a ship and delivered measurements with precisions of better than 0.03 % for XCO_2 and 0.04 % for XCH_4 , respectively. The published data set from atmospheric XCO_2 and XCH_4 measurements along the ship route from Cape Town to Bremerhaven was found to be a valuable data set to identify model-deficiencies along the measured north-south transect.

From a global perspective the EM27/SUN Fourier Transform Spectrometer aligns perfectly in the successful series of ground based measurements of carbon dioxide and methane. Due to its high accuracy and robustness, even under campaign conditions, the instrument is a valuable tool to infer sources and sinks of CO_2 and CH_4 . After calibration, the instrument’s accuracy is high enough to validate satellite soundings as well as to infer local source strengths and can clearly be seen as an emerging tool for accurate ground- or ship- based measurements of CO_2 and CH_4 .

Future campaigns on research vessels might adapt the ship’s course to perform direct satellite match-ups. This would enable the validation of satellite soundings in ocean glint geometries without coincidence criterion induced errors. The light infra-structure requirements of the instrument are an optimal match for performing ship-based measurements on a regular basis such as conventional cargo ships that regularly commute between the hemispheres. Deployments on cruise-ships, however, that predominant cruise in tropical regions, could help to address model-deficiencies in the inner-tropical convergence zone. Automation of the instrumentation that allows to cover the instrument under harsh weather conditions without human intervention could save personal and might enable remote operation. Challenges here might be wear of the solar tracker as well as sea-salt introduced corrosion. A suitable glass-dome to cover the instrument could be subject of further investigations.

Future cooperation between modeling working groups as well as measurement based working groups should be intensified in order to close the loop from measurement to model. Here the model delivered a-priori profiles could enhance the measurement quality. Accurate measurements, on the other hand, can contribute to model-development and decrease the uncertainty of “top down” inferred sources and sinks of CO_2 and CH_4 .

Acknowledgment

Diese Arbeit entstand am Institut für Meteorologie und Klimaforschung des Karlsruher Institut für Technologie. Die Arbeitsgruppe wurde gefördert durch das Emmy-Noether Programm der Deutschen Forschungsgemeinschaft (DFG) im Rahmen von BU2599/1-1 (RemoTeC).

Ganz Herzlich möchte ich mich für die konstruktive fachliche Zusammenarbeit mit meinem Gruppenleiter **André Butz** bedanken der auch viel Geduld mit meinen schriftlichen Abhandlungen hatte und stets für das Wohl seiner Mitarbeiter gesorgt hat.

Fachlich stand mir weiterhin **Frank Hase** stets mit vielen interessanten Anregungen und Diskussionen zur Seite, der sich trotz vieler Aufgaben durchaus auch mal die Zeit genommen hat z.B. einfache Fehler im retrieval Setup gemeinsam ausfindig zu machen. Überdies hat er meinen Optik-Horizont immens erweitern können.

Herzlicher Dank an **Prof. Dr. Johannes Orphal** der das Referat übernommen hat. Ebenfalls danke ich **Priv.-Doz. Dr. Michael Höpfner**, in seiner Rolle als Korreferent.

Weiterer Dank gilt den Studenten **Leonie Flotow**, **Marco Bertleff** und **Yannik Augenstein**, die zum Gelingen dieser Arbeit beigetragen haben. Besonders hervorzuheben sei hier **Julian Kostinek** der mit viel Elektronik-Knowhow und Engagement wesentliche Beiträge geleistet hat.

In weiteren Elektronik-Fragen konnte mir **Jochen Groß** stets mit Rat und Tat zur Seite stehen und hat mir gern seine exzellent ausgerüstete Werkstatt mitsamt umfangreichem Elektronik Grundstock zur Verfügung gestellt.

I want to thank **Aaldert van Amerongen** and his colleague **Tonny Coppens** from SRON for loaning the immersed grating and entrusting the precious object into my hands. I am very glad that I had the opportunity to test this grating.

Für Feinmechanische Arbeiten konnte mich stets unsere Werkstatt unterstützen, namentlich vertreten durch **Alexander Streili** und **Benjamin Riexinger**. In der direkten und unbürokratischen Zusammenarbeit sehe ich einen entscheidenden Baustein für ein Institut, das Pionierarbeit in der Geräteentwicklung leistet.

Ebenso danke ich der **Crew der FS-Polarstern** für die allumfassende Unterstützung. Ob kleine mechanische Arbeiten oder Aushilfe bei elektronischen Problemen, stets fand sich jemand an Bord, der weiter helfen konnte. Auch bedanke ich mich für die liebevoll vorbereitete Äquatortaufe, die mir wohl noch lange in Erinnerung bleiben wird. Besonderer Dank auch dem Fahrleiter **Hartwig Deneke**. Ob ich dem **Smutje und seiner Crew** danke muss ich mir noch überlegen, schließlich habe ich fast 10 kg zugenommen.

Thanks as well to **Anna Agustí-Panareda** and her colleague **Miha Razinger** at the ECMWF-model compartment for providing profile a-priories and very interesting insights into atmospheric modeling.

Arne Babenhauserheide ist ein Bürokollege, der immer ein offenes Ohr für aktuelle Fragestellungen hat und sich gern an der Lösung von fachlichen oder technischen Fragestellungen beteiligt. Wer einen solchen Bürokollegen nicht zu schätzen weiß ist selbst dran schuld.

Mit **Matthias Frey** konnte man sich auf unterschiedlichsten Niveaus austauschen und wenn es nicht lustig war, dann war es interessant. Danke auch für das Lektorat auf interkontinentalen Flügen.

Meiner Bürokollegin **Susanne Dohe** möchte ich für die erquicklichen Stunden auf der Arbeit und bei Winterurlaube danken - klingt möglicherweise anrücklich, war es aber nicht. Im Zuge dessen geht ein Gruß an den Kantinenclub, der stets für kurzweilige Mittagspausen gesorgt hat.

Phillip Hahne und seiner Frau **Lucia** danke ich für einen spannenden Urlaub auf schwedischen Seen und einen kurzen road-trip in den USA. Leider hatten wir nur kurz das Vergnügen Bürokollegen zu sein.

Ich danke **Thomas Blumenstock** für das Lektorat. Darüber hinaus ihm und seiner Frau **Gabi** für den abwechslungsreichen Ausgleich auf dem Paddelsee in Spöck. Die Weste wird irgendwann nochmal ausgelöst!

Meiner Mutter möchte ich für die aufmunternden Worte danken, wenn es mal nicht so gut lief. Die Versorgung mit Büro-Nahrung hat überdies zum Gelingen beigetragen.

Zu guter Letzt möchte ich mich ganz herzlich bei meiner Freundin **Mareike Felix** bedanken. Sie hat mit mir nicht nur einen Partner ausgehalten, der ständig mit dem Kopf (meist auch mit dem Rest) bei der Arbeit war, sondern ohne sie hätte ich nicht am Filet-Stück der Doktorarbeit (Polarstern-Kampagne) teilnehmen können. Danke auch für die Korrekturen! ♡

8 Bibliography

- Adrian, G. P., Baumann, M., Blumenstock, T., Fischer, H., Friedle, A., Gerhardt, L., Maucher, G., Oelhaf, H., Scheuerpflug, W., Thomas, P., Trieschmann, O., and Wegner, A. (1994). First results of ground-based ftir measurements of atmospheric trace gases in north sweden and greenland during easoe. *Geophysical Research Letters*, 21(13):1343–1346.
- Agustí-Panareda, A., Diamantakis, M., Bayona, V., Klappenbach, F., and Butz, A. (2016). Improving the inter-hemispheric gradient of total column atmospheric CO_2 and CH_4 in simulations with the ecmwf semi-lagrangian atmospheric global model. *Geoscientific Model Development*, –(143):–.
- Agustí-Panareda, A., Massart, S., Chevallier, F., Boussetta, S., Balsamo, G., Beljaars, A., Ciais, P., Deutscher, N. M., Engelen, R., Jones, L., Kivi, R., Paris, J.-D., Peuch, V.-H., Sherlock, V., Vermeulen, A. T., Wennberg, P. O., and Wunch, D. (2014). Forecasting global atmospheric CO_2 . *Atmospheric Chemistry and Physics*, 14(21):11959–11983.
- Aiuppa, A., Cannata, A., Cannavò, F., Di Grazia, G., Ferrari, F., Giudice, G., Gurrieri, S., Liuzzo, M., Mattia, M., Montalto, P., Patanè, D., and Puglisi, G. (2010). Patterns in the recent 2007–2008 activity of mount etna volcano investigated by integrated geophysical and geochemical observations. *Geochemistry, Geophysics, Geosystems*, 11(9):n/a–n/a. Q09008.
- Aiuppa, A., Moretti, R., Federico, C., Giudice, G., Gurrieri, S., Liuzzo, M., Papale, P., Shinohara, H., and Valenza, M. (2007). Forecasting etna eruptions by real-time observation of volcanic gas composition. *Geology*, 35(12):1115–1118.
- Allen, M., Erickson, D., Kendall, W., Fu, J., Ott, L., and Pawson, S. (2012). The influence of internal model variability in geos-5 on interhemispheric CO_2 exchange. *Journal of Geophysical Research: Atmospheres*, 117(D10):n/a–n/a. D10107.
- Atkins, P. W. and De Paula, J., editors (2013). *Physikalische Chemie*, volume [Hauptbd.]:. Wiley-VCH, Weinheim, 5. aufl. edition. Wird auch zusammen mit dem Arbeitsbuch Physikalische Chemie von Trapp, Charles A ... als Set angeboten.
- Babenhauserheide, A., Basu, S., Houweling, S., Peters, W., and Butz, A. (2015). Comparing the carbontracker and tm5-4dvar data assimilation systems for CO_2 surface flux inversions. *Atmospheric Chemistry and Physics*, 15(17):9747–9763.

- Baker, D. F. (2001). *Sources and sinks of atmospheric CO₂ estimated from batch least-squares inversions of CO₂ concentration measurements*. PhD thesis, Princeton University.
- Bermejo, R. and Conde, J. (2002). A conservative quasi-monotone semi-lagrangian scheme. *Monthly Weather Review*, 130(2):423–430.
- Bertleff, M. (2014). Camera based sun tracking system for mobile platforms. Master’s thesis, Karlsruhe Institute of Technology (KIT).
- Blumstein, D., Tournier, B., Cayla, F. R., Phulpin, T., Fjortoft, R., Buil, C., and Ponce, G. (2007). In-flight performance of the infrared atmospheric sounding interferometer (iasi) on metop-a. *Proc. SPIE*, 6684:66840H–66840H–12.
- Boussetta, S., Balsamo, G., Beljaars, A., Agustí-Panareda, A., Calvet, J.-C., Jacobs, C., van den Hurk, B., Viterbo, P., Lafont, S., Dutra, E., Jarlan, L., Balzarolo, M., Papale, D., and van der Werf, G. (2013). Natural carbon dioxide exchanges in the ecmwf integrated forecasting system: Implementation and offline validation. *JGRA*, 118:1–24.
- Bovensmann, H., Buchwitz, M., Burrows, J. P., Reuter, M., Krings, T., Gerilowski, K., Schneising, O., Heymann, J., Tretner, A., and Erzinger, J. (2010). A remote sensing technique for global monitoring of power plant CO₂ emissions from space and related applications. *Atmospheric Measurement Techniques*, 3(4):781–811.
- Bovensmann, H., Burrows, J. P., Buchwitz, M., Frerick, J., Noël, S., Rozanov, V. V., Chance, K. V., and Goede, A. P. H. (1999). Sciamachy: Mission objectives and measurement modes. *Journal of the Atmospheric Sciences*, 56(2):127–150.
- Brenninkmeijer, C. A. M., Crutzen, P., Boumard, F., Dauer, T., Dix, B., Ebinghaus, R., Filippi, D., Fischer, H., Franke, H., Frieß, U., Heintzenberg, J., Helleis, F., Hermann, M., Kock, H. H., Koepfel, C., Lelieveld, J., Leuenberger, M., Martinsson, B. G., Miemczyk, S., Moret, H. P., Nguyen, H. N., Nyfeler, P., Oram, D., O’Sullivan, D., Penkett, S., Platt, U., Pucek, M., Ramonet, M., Randa, B., Reichelt, M., Rhee, T. S., Rohwer, J., Rosenfeld, K., Scharffe, D., Schlager, H., Schumann, U., Slemr, F., Sprung, D., Stock, P., Thaler, R., Valentino, F., van Velthoven, P., Waibel, A., Wandel, A., Waschitschek, K., Wiedensohler, A., Xueref-Remy, I., Zahn, A., Zech, U., and Ziereis, H. (2007). Civil aircraft for the regular investigation of the atmosphere based on an instrumented container: The new caribic system. *Atmospheric Chemistry and Physics*, 7(18):4953–4976.
- Brooks, D. R. and Mims, F. M. (2001). Development of an inexpensive handheld led-based sun photometer for the globe program. *Journal of Geophysical Research: Atmospheres*, 106(D5):4733–4740.
- Burrows, J., Hölzle, E., Goede, A., Visser, H., and Fricke, W. (1995). Sciamachy—scanning imaging absorption spectrometer for atmospheric cartography. *Acta Astronautica*, 35(7):445 – 451. Earth Observation.

- Butz, A., Dinger, A., Bobrowski, N., Kostinek, J., Fieber, L., Fischerkeller, M.-C., Giuffrida, G., Hase, F., Klappenbach, F., Kuhn, J., Luebke, L., Tripitz, L., and Tu, Q. (2016). Submitted: Remote sensing of volcanic CO_2 enhancements in the downwind plume of mt. etna. *Geophysical Research Letters*.
- Butz, A., Guerlet, S., Hasekamp, O., Schepers, D., Galli, A., Aben, I., Frankenberg, C., Hartmann, J.-M., Tran, H., Kuze, A., Keppel-Aleks, G., Toon, G., Wunch, D., Wennberg, P., Deutscher, N., Griffith, D., Macatangay, R., Messerschmidt, J., Notholt, J., and Warneke, T. (2011). Toward accurate CO_2 and CH_4 observations from gosat. *Geophysical Research Letters*, 38(14):n/a–n/a.
- Butz, A., Guerlet, S., Hasekamp, O. P., Kuze, A., and Suto, H. (2013). Using ocean-glint scattered sunlight as a diagnostic tool for satellite remote sensing of greenhouse gases. *Atmospheric Measurement Techniques*, 6(9):2509–2520.
- Butz, A., Hasekamp, O. P., Frankenberg, C., and Aben, I. (2009). Retrievals of atmospheric CO_2 from simulated space-borne measurements of backscattered near-infrared sunlight: accounting for aerosol effects. *Appl. Opt.*, 48(18):3322–3336.
- Butz, A., Hasekamp, O. P., Frankenberg, C., Vidot, J., and Aben, I. (2010). CH_4 retrievals from space-based solar backscatter measurements: Performance evaluation against simulated aerosol and cirrus loaded scenes. *Journal of Geophysical Research: Atmospheres*, 115(D24):n/a–n/a. D24302.
- Chandra, S., Fleming, E. L., Schoeberl, M. R., and Barnett, J. J. (1990). Monthly mean global climatology of temperature, wind, geopotential height and pressure for 0–120 km. *Advances in Space Research*, 10(6):3 – 12.
- Chase, D. B. (1984). Nonlinear detector response in ft-ir. *Appl. Spectrosc.*, 38(4):491–494.
- Crisp, D., Atlas, R., Breon, F.-M., Brown, L., Burrows, J., Ciais, P., Connor, B., Doney, S., Fung, I., Jacob, D., et al. (2004). The orbiting carbon observatory (oco) mission. *Advances in Space Research*, 34(4):700 – 709. Trace Constituents in the Troposphere and Lower Stratosphere.
- Crisp, D., Fisher, B. M., O’Dell, C., Frankenberg, C., Basilio, R., Bösch, H., Brown, L. R., Castano, R., Connor, B., Deutscher, N. M., Eldering, A., Griffith, D., Gunson, M., Kuze, A., Mandrake, L., McDuffie, J., Messerschmidt, J., Miller, C. E., Morino, I., Natraj, V., Notholt, J., O’Brien, D. M., Oyafuso, F., Polonsky, I., Robinson, J., Salawitch, R., Sherlock, V., Smyth, M., Suto, H., Taylor, T. E., Thompson, D. R., Wennberg, P. O., Wunch, D., and Yung, Y. L. (2012). The acos CO_2 retrieval algorithm – part ii: Global x_{CO_2} data characterization. *Atmospheric Measurement Techniques*, 5(4):687–707.
- Crosson, E. (2008). A cavity ring-down analyzer for measuring atmospheric levels of methane, carbon dioxide, and water vapor. *Applied Physics B*, 92(3):403–408.

- Demtröder, W. (2010). *Experimentalphysik*, volume 3: Atome, Moleküle und Festkörper : mit ... 48 Tabellen, zahlreichen durchgerechneten Beispielen und 151 Übungsaufgaben mit ausführlichen Lösungen of *Springer-Lehrbuch*. Springer, Berlin, 4., überarb. Aufl. edition. Richtige Bandbenennung von Bd. 3 teilweise nur auf dem Umschlag Kern-, Teilchen- und Astrophysik.
- Demtröder, W. (2013). *Experimentalphysik 2 : Elektrizität und Optik*. Springer-LehrbuchSpringerLink : Bücher. Springer, Berlin, Heidelberg, 6., überarb. u. akt. Aufl. 2013 edition.
- Denman, K. L., Menon, S., Brasseur, G., Chidthaisong, A., Ciais, P., Cox, P. M., Dickinson, R. E., Hauglustaine, D., Heinze, C., Holland, E., et al. (2007). *Couplings Between Changes in the Climate System and Biogeochemistry*, pages 499–588. Cambridge University Press.
- Denning, A. S., Fung, I. Y., and Randall, D. (1995). Latitudinal gradient of atmospheric CO₂ due to seasonal exchange with land biota. *Nature*, 376(6537):240–243.
- Dentener, F., Stevenson, D., Cofala, J., Mechler, R., Amann, M., Bergamaschi, P., Raes, F., and Derwent, R. (2005). The impact of air pollutant and methane emission controls on tropospheric ozone and radiative forcing: Ctm calculations for the period 1990-2030. *Atmospheric Chemistry and Physics*, 5(7):1731–1755.
- Deutscher, N. M., Griffith, D. W. T., Bryant, G. W., Wennberg, P. O., Toon, G. C., Washenfelder, R. A., Keppel-Aleks, G., Wunch, D., Yavin, Y., Allen, N. T., Blavier, J.-F., Jiménez, R., Daube, B. C., Bright, A. V., Matross, D. M., Wofsy, S. C., and Park, S. (2010). Total column CO₂ measurements at Darwin, Australia; site description and calibration against in situ aircraft profiles. *Atmospheric Measurement Techniques*, 3(4):947–958.
- Dlugokencky, E., Crotwell, A., Lang, P., and Mund, J. (2016). Atmospheric methane dry air mole fractions from quasi-continuous measurements at Barrow, Alaska and Mauna Loa, Hawaii, 1986-2015, version: 2016-01-22.
- Dohe, S., Sherlock, V., Hase, F., Gisi, M., Robinson, J., Sepúlveda, E., Schneider, M., and Blumenstock, T. (2013). A method to correct sampling ghosts in historic near-infrared Fourier transform spectrometer (FTS) measurements. *Atmospheric Measurement Techniques*, 6(8):1981–1992.
- Ebizuka, N., Iye, M., Sasaki, T., and Wakaki, M. (1998). Development of high-dispersion gratings and immersion gratings for spectrographs of the Subaru telescope.
- Ebizuka, N., Iye, M., Sugioka, K., and Ebisuzaki, T. (2002). Grism. US Patent 6,469,846.
- Elkins, J. W., Thompson, T. M., Swanson, T. H., Butler, J. H., Hall, B. D., Cummings, S. O., Fishers, D. A., and Raffen, A. G. (1993). Decrease in the growth rates of atmospheric chlorofluorocarbons 11 and 12. *Nature*, 364(6440):780–783.

- Feist, D., Gerbig, C., Geibel, M., Chen, H., Kolle, O., Hertel, M., Baum, S., Messerschmidt, J., Notholt, J., Palm, M., et al. (2010). The imecc aircraft campaign: validation of total column co₂, ch₄ and co measurements over europe. In *EGU General Assembly Conference Abstracts*, volume 12, page 13179.
- Feist, D. G., Arnold, S. G., Hase, F., and Ponge, D. (2015). Rugged optical mirrors for fourier-transform spectrometers operated in harsh environments. *Atmospheric Measurement Techniques Discussions*, 8:10711–10734.
- Fischer, H., Birk, M., Blom, C., Carli, B., Carlotti, M., von Clarmann, T., Delbouille, L., Dudhia, A., Ehhalt, D., Endemann, M., Flaud, J. M., Gessner, R., Kleinert, A., Koopman, R., Langen, J., López-Puertas, M., Mosner, P., Nett, H., Oelhaf, H., Perron, G., Remedios, J., Ridolfi, M., Stiller, G., and Zander, R. (2008). Mipas: an instrument for atmospheric and climate research. *Atmospheric Chemistry and Physics*, 8(8):2151–2188.
- Flowers, B. A., Powers, H. H., Dubey, M. K., and McDowell, N. G. (2012). Inter-comparison of two high-accuracy fast-response spectroscopic sensors of carbon dioxide: a case study. *Atmospheric Measurement Techniques*, 5(5):991–997.
- Frehlich, R. G. (1992). Estimation of the nonlinearity of a photodetector. *Appl. Opt.*, 31(28):5926–5929.
- Frey, M., Hase, F., Blumenstock, T., Groß, J., Kiel, M., Mengistu Tsidu, G., Schäfer, K., Sha, M. K., and Orphal, J. (2015). Use of portable ftir spectrometers for detecting greenhouse gas emissions of the megacity berlin – part 1: Instrumental line shape characterisation and calibration of a quintuple of spectrometers. *Atmospheric Measurement Techniques Discussions*, 8(3):2735–2766.
- Fuhr, J. R. and Wiese, W. L. (2005). Nist atomic transition probabilities. In Lide, D. R., editor, *CRC Handbook of Chemistry and Physics*. CRC Press, Boca Raton, FL, 86th edition.
- García, O. E., Schneider, M., Redondas, A., González, Y., Hase, F., Blumenstock, T., and Sepúlveda, E. (2012). Investigating the long-term evolution of subtropical ozone profiles applying ground-based ftir spectrometry. *Atmospheric Measurement Techniques*, 5(11):2917–2931.
- Geller, L. S., Elkins, J. W., Lobert, J. M., Clarke, A. D., Hurst, D. F., Butler, J. H., and Myers, R. C. (1997). Tropospheric sf₆: Observed latitudinal distribution and trends, derived emissions and interhemispheric exchange time. *Geophysical Research Letters*, 24(6):675–678.
- Gisi, M. (2012). *Setup of precise camera based solar tracker systems and greenhouse gas measurements using a modified portable spectrometer*. PhD thesis, Karlsruhe Institute of Technology (KIT).

- Gisi, M., Hase, F., Dohe, S., and Blumenstock, T. (2011). Camtracker: a new camera controlled high precision solar tracker system for ftir-spectrometers. *Atmospheric Measurement Techniques*, 4(1):47–54.
- Gisi, M., Hase, F., Dohe, S., Blumenstock, T., Simon, A., and Keens, A. (2012). Xco₂-measurements with a tabletop fts using solar absorption spectroscopy. *Atmospheric Measurement Techniques*, 5(11):2969–2980.
- Gloor, M., Gatti, L., Brienen, R., Feldpausch, T. R., Phillips, O. L., Miller, J., Ometto, J. P., Rocha, H., Baker, T., de Jong, B., Houghton, R. A., Malhi, Y., Aragão, L. E. O. C., Guyot, J.-L., Zhao, K., Jackson, R., Peylin, P., Sitch, S., Poulter, B., Lomas, M., Zaehle, S., Huntingford, C., Levy, P., and Lloyd, J. (2012). The carbon balance of south america: a review of the status, decadal trends and main determinants. *Biogeosciences*, 9(12):5407–5430.
- Guerlet, S., Basu, S., Butz, A., Krol, M., Hahne, P., Houweling, S., Hasekamp, O. P., and Aben, I. (2013a). Reduced carbon uptake during the 2010 northern hemisphere summer from gosat. *Geophysical Research Letters*, 40(10):2378–2383.
- Guerlet, S., Butz, A., Schepers, D., Basu, S., Hasekamp, O. P., Kuze, A., Yokota, T., Blavier, J.-F., Deutscher, N. M., Griffith, D. W., Hase, F., Kyro, E., Morino, I., Sherlock, V., Sussmann, R., Galli, A., and Aben, I. (2013b). Impact of aerosol and thin cirrus on retrieving and validating xco₂ from gosat shortwave infrared measurements. *Journal of Geophysical Research: Atmospheres*, 118(10):4887–4905.
- Hajian, A. R., Behr, B. B., Cenko, A. T., Olling, R. P., Mozurkewich, D., Armstrong, J. T., Pohl, B., Petrossian, S., Knuth, K. H., Hindsley, R. B., et al. (2007). Initial results from the usno dispersed fourier transform spectrograph. *The Astrophysical Journal*, 661(1):616.
- Hannigan, J. W. (2011). Ndacc irwg: Evolution of ground-based global trace gas infrared remote sensing. In *Imaging and Applied Optics*, page FMC1. Optical Society of America.
- Hansen, J., Ruedy, R., Sato, M., and Lo, K. (2010). Global surface temperature change. *Reviews of Geophysics*, 48(4):n/a–n/a. RG4004.
- Hase, F. (2000). *Inversion von Spurengasprofilen aus hochaufgelösten bodengebundenen FTIR-Messungen in Absorption*. PhD thesis, Universität Karlsruhe. Karlsruhe, Univ., Diss., 2000.
- Hase, F., Blumenstock, T., Fellows, C., Frey, M., Gisi, M., Groß, J., Kiel, M., Sha, M. K., G., M.-T., F., O., J., O., and Tolzmann, J., editors (2014). *COCCON: Collaborative Carbon Column Observing Network*.
- Hase, F., Blumenstock, T., and Paton-Walsh, C. (1999). Analysis of the instrumental line shape of high-resolution fourier transform ir spectrometers with gas cell measurements and new retrieval software. *Appl. Opt.*, 38(15):3417–3422.

- Hase, F., Frey, M., Blumenstock, T., Groß, J., Kiel, M., Kohlhepp, R., Mengistu Tsidu, G., Schäfer, K., Sha, M. K., and Orphal, J. (2015). Use of portable ftir spectrometers for detecting greenhouse gas emissions of the megacity berlin – part 2: Observed time series of xco₂ and xch₄. *Atmospheric Measurement Techniques Discussions*, 8(3):2767–2791.
- Hase, F., Hannigan, J., Coffey, M., Goldman, A., Höpfner, M., Jones, N., Rinsland, C., and Wood, S. (2004). Intercomparison of retrieval codes used for the analysis of high-resolution, ground-based {FTIR} measurements. *Journal of Quantitative Spectroscopy and Radiative Transfer*, 87(1):25 – 52.
- Haynes, W. M. H., editor (2015). *2015 - 2016*. CRC handbook of chemistry and physics ; 96. CRC Press, Boca Raton, Fla. [u.a.].
- Hecht, E. (2014). *Optik*. Studium. De Gruyter, München, 6., verb. Aufl. edition.
- Hodson, E. L., Poulter, B., Zimmermann, N. E., Prigent, C., and Kaplan, J. O. (2011). The el niño–southern oscillation and wetland methane interannual variability. *Geophysical Research Letters*, 38(8):n/a–n/a. L08810.
- Howarth, R. W., Santoro, R., and Ingraffea, A. (2011). Methane and the greenhouse-gas footprint of natural gas from shale formations. *Climatic Change*, 106(4):679–690.
- James, J. F. (2007). *Spectrograph design fundamentals*. Cambridge University Press, Cambridge [u.a.], 1. publ. edition. Includes bibliographical references and index.
- Karion, A., Sweeney, C., Tans, P., and Newberger, T. (2010). Aircore: An innovative atmospheric sampling system. *Journal of Atmospheric and Oceanic Technology*, 27(11):1839–1853.
- Kiel, M., Wunch, D., Wennberg, P. O., Toon, G. C., Hase, F., and Blumenstock, T. (2016). Improved retrieval of gas abundances from near-infrared solar ftir spectra measured at the karlsruhe tcon station. *Atmospheric Measurement Techniques*, 9(2):669–682.
- Kischkat, J., Peters, S., Gruska, B., Semtsiv, M., Chashnikova, M., Klinkmüller, M., Fedosenko, O., Machulik, S., Aleksandrova, A., Monastyrskiy, G., Flores, Y., and Masselink, W. T. (2012). Mid-infrared optical properties of thin films of aluminum oxide, titanium dioxide, silicon dioxide, aluminum nitride, and silicon nitride. *Appl. Opt.*, 51(28):6789–6798.
- Klappenbach, F., Bertleff, M., Kostinek, J., Hase, F., Blumenstock, T., Agusti-Panareda, A., Razinger, M., and Butz, A. (2015). Accurate mobile remote sensing of xco₂ and xch₄ latitudinal transects from aboard a research vessel. *Atmospheric Measurement Techniques*, 8(12):5023–5038.
- Kobayashi, N., Inoue, G., Kawasaki, M., Yoshioka, H., Minomura, M., Murata, I., Nagahama, T., Matsumi, Y., Tanaka, T., Morino, I., and Ibuki, T. (2010). Remotely operable compact

instruments for measuring atmospheric CO_2 and CH_4 column densities at surface monitoring sites. *Atmospheric Measurement Techniques*, 3(4):1103–1112.

Kostinek, J. (2013). Bestimmung der Linearität von Photodetektoren. Master's thesis, Karlsruhe Institute of Technology (KIT).

Kramer, I. (2007). Zeitreihen troposphärischer Spurengase abgeleitet aus bodengebundenen FTIR-Messungen. Technical report, Forschungszentrum Karlsruhe, Karlsruhe. Zugl.: Karlsruhe, Univ., Diss., 2006.

Lamouroux, J., Tran, H., Laraia, A., Gamache, R., Rothman, L., Gordon, I., and Hartmann, J.-M. (2010). Updated database plus software for line-mixing in CO_2 infrared spectra and their test using laboratory spectra in the 1.5–2.3 μm region. In *XVIth Symposium on High Resolution Molecular Spectroscopy (HighRes-2009) XVIth Symposium on High Resolution Molecular Spectroscopy, 2009*, volume 111, pages 2321 – 2331, Lake Baikal.

Law, R. M., Matear, R. J., and Francey, R. J. (2008). Comment on “saturation of the southern ocean CO_2 sink due to recent climate change”. *Science*, 319(5863):570a–570a.

Le Quéré, C., Andres, R. J., Boden, T., Conway, T., Houghton, R. A., House, J. I., Marland, G., Peters, G. P., van der Werf, G. R., Ahlström, A., Andrew, R. M., Bopp, L., Canadell, J. G., Ciais, P., Doney, S. C., Enright, C., Friedlingstein, P., Huntingford, C., Jain, A. K., Jourdain, C., Kato, E., Keeling, R. F., Klein Goldewijk, K., Levis, S., Levy, P., Lomas, M., Poulter, B., Raupach, M. R., Schwinger, J., Sitch, S., Stocker, B. D., Viovy, N., Zaehle, S., and Zeng, N. (2013). The global carbon budget 1959–2011. *Earth System Science Data*, 5(1):165–185.

Li, H. H. (1980). Refractive index of silicon and germanium and its wavelength and temperature derivatives. *Journal of Physical and Chemical Reference Data*, 9(3):561–658.

Lunze, J. (2013). *Regelungstechnik*, volume 1: Systemtheoretische Grundlagen, Analyse und Entwurf einschleifiger Regelungen : mit ... 76 Beispielen, 165 Übungsaufgaben sowie einer Einführung in das Programmsystem MATLAB of *Springer-Lehrbuch*. Springer Vieweg, Berlin, 9., überarb. Aufl. edition. Mit 415 Abb., 76 Beispielen, 165 Übungsaufgaben sowie einer Einführung in das Programmsystem MATLAB.

Machida, T., Matsueda, H., Sawa, Y., Nakagawa, Y., Hirotsu, K., Kondo, N., Goto, K., Nakazawa, T., Ishikawa, K., and Ogawa, T. (2008). Worldwide measurements of atmospheric CO_2 and other trace gas species using commercial airlines. *Journal of Atmospheric and Oceanic Technology*, 25(10):1744–1754.

Masarie, K. A., Langenfelds, R. L., Allison, C. E., Conway, T. J., Dlugokencky, E. J., Francey, R. J., Novelli, P. C., Steele, L. P., Tans, P. P., Vaughn, B., and White, J. W. C. (2001). NOAA/CSIRO flask air intercomparison experiment: A strategy for directly assessing

- consistency among atmospheric measurements made by independent laboratories. *Journal of Geophysical Research: Atmospheres*, 106(D17):20445–20464.
- Masarie, K. A., Peters, W., Jacobson, A. R., and Tans, P. P. (2014). Obspack: a framework for the preparation, delivery, and attribution of atmospheric greenhouse gas measurements. *Earth System Science Data*, 6(2):375–384.
- Masarie, K. A., Pétron, G., Andrews, A., Bruhwiler, L., Conway, T. J., Jacobson, A. R., Miller, J. B., Tans, P. P., Worthy, D. E., and Peters, W. (2011). Impact of co₂ measurement bias on carbontracker surface flux estimates. *Journal of Geophysical Research: Atmospheres*, 116(D17):n/a–n/a. D17305.
- Massart, S., Agusti-Panareda, A., Aben, I., Butz, A., Chevallier, F., Crevoisier, C., Engelen, R., Frankenberg, C., and Hasekamp, O. (2014). Assimilation of atmospheric methane products into the macc-ii system: from sciamachy to tanso and iasi. *Atmospheric Chemistry and Physics*, 14(12):6139–6158.
- McGuire, A., Christensen, T., Hayes, D., Heroult, A., Euskirchen, E., Kimball, J., Koven, C., Lafleur, P., Miller, P., Oechel, W., et al. (2012). An assessment of the carbon balance of arctic tundra: comparisons among observations, process models, and atmospheric inversions. *Biogeosciences*, 9(8):3185–3204.
- Messerschmidt, J., Macatangay, R., Notholt, J., Petri, C., Warneke, T., and Weinzierl, C. (2011). Side by side measurements of co₂ by ground-based fourier transform spectrometry (fts). *Tellus B*, 62(5).
- Morino, I., Uchino, O., Inoue, M., Yoshida, Y., Yokota, T., Wennberg, P. O., Toon, G. C., Wunch, D., Roehl, C. M., Notholt, J., Warneke, T., Messerschmidt, J., Griffith, D. W. T., Deutscher, N. M., Sherlock, V., Connor, B., Robinson, J., Sussmann, R., and Rettinger, M. (2011). Preliminary validation of column-averaged volume mixing ratios of carbon dioxide and methane retrieved from gosat short-wavelength infrared spectra. *Atmospheric Measurement Techniques*, 4(6):1061–1076.
- Notholt, J., Beninga, I., and Schrems, O. (1995). Shipborne ft-ir measurements of atmospheric trace gases on a south (33°s) to north (53°n) atlantic traverse. *Appl. Spectrosc.*, 49(10):1525–1527.
- O’Dell, C. W., Connor, B., Bösch, H., O’Brien, D., Frankenberg, C., Castano, R., Christi, M., Eldering, D., Fisher, B., Gunson, M., McDuffie, J., Miller, C. E., Natraj, V., Oyafuso, F., Polonsky, I., Smyth, M., Taylor, T., Toon, G. C., Wennberg, P. O., and Wunch, D. (2012). The acos co₂ retrieval algorithm – part 1: Description and validation against synthetic observations. *Atmospheric Measurement Techniques*, 5(1):99–121.

- Oppenheim, A. V., Schafer, R. W., and Buck, J. R. (2004). *Zeitdiskrete Signalverarbeitung*. Pearson-Studiumet - Elektrotechnik : Signalverarbeitung. Pearson Studium, München [u.a.], 2., überarb. Aufl., [neuübers.] edition. Aus dem Engl. übers.
- Oshchepkov, S., Bril, A., Yokota, T., Morino, I., Yoshida, Y., Matsunaga, T., Belikov, D., Wunch, D., Wennberg, P., Toon, G., O'Dell, C., Butz, A., Guerlet, S., Cogan, A., Boesch, H., Eguchi, N., Deutscher, N., Griffith, D., Macatangay, R., Notholt, J., Sussmann, R., Rettinger, M., Sherlock, V., Robinson, J., Kyrö, E., Heikkinen, P., Feist, D. G., Nagahama, T., Kadygrov, N., Maksyutov, S., Uchino, O., and Watanabe, H. (2012). Effects of atmospheric light scattering on spectroscopic observations of greenhouse gases from space: Validation of ppdf-based co2 retrievals from gosat. *Journal of Geophysical Research: Atmospheres*, 117(D12):n/a–n/a. D12305.
- Oshchepkov, S., Bril, A., Yokota, T., Wennberg, P. O., Deutscher, N. M., Wunch, D., Toon, G. C., Yoshida, Y., O'Dell, C. W., Crisp, D., Miller, C. E., Frankenberg, C., Butz, A., Aben, I., Guerlet, S., Hasekamp, O., Boesch, H., Cogan, A., Parker, R., Griffith, D., Macatangay, R., Notholt, J., Sussmann, R., Rettinger, M., Sherlock, V., Robinson, J., Kyrö, E., Heikkinen, P., Feist, D. G., Morino, I., Kadygrov, N., Belikov, D., Maksyutov, S., Matsunaga, T., Uchino, O., and Watanabe, H. (2013). Effects of atmospheric light scattering on spectroscopic observations of greenhouse gases from space. part 2: Algorithm intercomparison in the gosat data processing for co2 retrievals over tcon sites. *Journal of Geophysical Research: Atmospheres*, 118(3):1493–1512.
- Palchetti, L., Bianchini, G., Cortesi, U., Pascale, E., and Lee, C. (2002). Assessment of detector nonlinearity in fourier transform spectroscopy. *Applied spectroscopy*, 56(2):271–274.
- Parker, R., Boesch, H., Cogan, A., Fraser, A., Feng, L., Palmer, P. I., Messerschmidt, J., Deutscher, N., Griffith, D. W. T., Notholt, J., Wennberg, P. O., and Wunch, D. (2011). Methane observations from the greenhouse gases observing satellite: Comparison to ground-based tcon data and model calculations. *Geophysical Research Letters*, 38(15):n/a–n/a. L15807.
- Peters, W., Jacobson, A. R., Sweeney, C., Andrews, A. E., Conway, T. J., Masarie, K., Miller, J. B., Bruhwiler, L. M. P., Pétron, G., Hirsch, A. I., Worthy, D. E. J., van der Werf, G. R., Randerson, J. T., Wennberg, P. O., Krol, M. C., and Tans, P. P. (2007). An atmospheric perspective on north american carbon dioxide exchange: Carbontracker. *Proceedings of the National Academy of Sciences*, 104(48):18925–18930.
- Pettit, G. D. and Turner, W. J. (1965). Refractive index of inp. *Journal of Applied Physics*, 36(6):2081–2081.

- Petty, M. C. (2007). *Molecular electronics : from principles to practice*. Wiley series in materials for electronic and optoelectronic applications. Wiley, Chichester. Includes bibliographical references and index.
- Peylin, P., Law, R. M., Gurney, K. R., Chevallier, F., Jacobson, A. R., Maki, T., Niwa, Y., Patra, P. K., Peters, W., Rayner, P. J., Rödenbeck, C., van der Laan-Luijkx, I. T., and Zhang, X. (2013). Global atmospheric carbon budget: results from an ensemble of atmospheric CO₂ inversions. *Biogeosciences*, 10(10):6699–6720.
- Phulpin, T., Blumstein, D., Prel, F., Tournier, B., Prunet, P., and Schlüssel, P. (2007). Applications of iasi on metop-a: first results and illustration of potential use for meteorology, climate monitoring, and atmospheric chemistry. *Proc. SPIE*, 6684:66840F–66840F–12.
- Prather, M. J., Holmes, C. D., and Hsu, J. (2012). Reactive greenhouse gas scenarios: Systematic exploration of uncertainties and the role of atmospheric chemistry. *Geophysical Research Letters*, 39(9):n/a–n/a. L09803.
- Redman, S. L., Nave, G., and Sansonetti, C. J. (2014). The spectrum of thorium from 250nm to 5500nm: Ritz wavelengths and optimized energy levels. *The Astrophysical Journal Supplement Series*, 211(1):4.
- Richardson, R. L., Yang, H., and Griffiths, P. R. (1998). Evaluation of a correction for photometric errors in ft-ir spectrometry introduced by a nonlinear detector response. *Appl. Spectrosc.*, 52(4):565–571.
- Rodgers, C. D. and Connor, B. J. (2003). Intercomparison of remote sounding instruments. *Journal of Geophysical Research: Atmospheres*, 108(D3):n/a–n/a. 4116.
- Rothman, L., Gordon, I., Barbe, A., Benner, D., Bernath, P., Birk, M., Boudon, V., Brown, L., Campargue, A., Champion, J.-P., Chance, K., Coudert, L., Dana, V., Devi, V., Fally, S., Flaud, J.-M., Gamache, R., Goldman, A., Jacquemart, D., Kleiner, I., Lacome, N., Lafferty, W., Mandin, J.-Y., Massie, S., Mikhailenko, S., Miller, C., Moazzen-Ahmadi, N., Naumenko, O., Nikitin, A., Orphal, J., Perevalov, V., Perrin, A., Predoi-Cross, A., Rinsland, C., Rotger, M., Šimečková, M., Smith, M., Sung, K., Tashkun, S., Tennyson, J., Toth, R., Vandaele, A., and Auwera, J. V. (2009). The hitran 2008 molecular spectroscopic database. *Journal of Quantitative Spectroscopy and Radiative Transfer*, 110(9–10):533 – 572. HITRAN.
- Sanders, C. L. (1962). A photocell linearity tester. *Appl. Opt.*, 1(3):207–211.
- Schepers, D., Guerlet, S., Butz, A., Landgraf, J., Frankenberg, C., Hasekamp, O., Blavier, J.-F., Deutscher, N. M., Griffith, D. W. T., Hase, F., Kyro, E., Morino, I., Sherlock, V., Sussmann, R., and Aben, I. (2012). Methane retrievals from greenhouse gases observing satellite (gosat) shortwave infrared measurements: Performance comparison of

proxy and physics retrieval algorithms. *Journal of Geophysical Research: Atmospheres*, 117(D10):n/a–n/a.

Schimel, D. S., House, J. I., Hibbard, K. A., Bousquet, P., Ciais, P., Peylin, P., Braswell, B. H., Apps, M. J., Baker, D., Bondeau, A., Canadell, J., Churkina, G., Cramer, W., Denning, A. S., Field, C. B., Friedlingstein, P., Goodale, C., Heimann, M., Houghton, R. A., Melillo, J. M., Moore, B., Murdiyarso, D., Noble, I., Pacala, S. W., Prentice, I. C., Raupach, M. R., Rayner, P. J., Scholes, R. J., Steffen, W. L., and Wirth, C. (2001). Recent patterns and mechanisms of carbon exchange by terrestrial ecosystems. *Nature*, 414(6860):169–172.

Schneider, M., Hase, F., Blumenstock, T., Redondas, A., and Cuevas, E. (2008). Quality assessment of CO_2 profiles measured by a state-of-the-art ground-based ftir observing system. *Atmospheric Chemistry and Physics*, 8(18):5579–5588.

Schneising, O., Buchwitz, M., Burrows, J. P., Bovensmann, H., Reuter, M., Notholt, J., Macatangay, R., and Warneke, T. (2008). Three years of greenhouse gas column-averaged dry air mole fractions retrieved from satellite – part 1: Carbon dioxide. *Atmospheric Chemistry and Physics*, 8(14):3827–3853.

Schneising, O., Burrows, J. P., Dickerson, R. R., Buchwitz, M., Reuter, M., and Bovensmann, H. (2014). Remote sensing of fugitive methane emissions from oil and gas production in north american tight geologic formations. *Earth's Future*, 2(10):548–558. 2014EF000265.

Schuck, T. J., Brenninkmeijer, C. A. M., Slemr, F., Xueref-Remy, I., and Zahn, A. (2009). Greenhouse gas analysis of air samples collected onboard the caribic passenger aircraft. *Atmospheric Measurement Techniques*, 2(2):449–464.

Schulze, E. D. (1986). Carbon dioxide and water vapor exchange in response to drought in the atmosphere and in the soil. *Annual Review of Plant Physiology*, 37(1):247–274.

Schulze, E.-D. (2006). Biological control of the terrestrial carbon sink. *Biogeosciences*, 3(2):147–166.

Sepúlveda, E., Schneider, M., Hase, F., García, O. E., Gomez-Pelaez, A., Dohe, S., Blumenstock, T., and Guerra, J. C. (2012). Long-term validation of tropospheric column-averaged CH_4 mole fractions obtained by mid-infrared ground-based ftir spectrometry. *Atmospheric Measurement Techniques*, 5(6):1425–1441.

Sha, M. K. (2013). *Characterization and Optimization of the new Imaging Fourier Transform Spectrometer GLORIA*. PhD thesis, Karlsruher Institut für Technologie (KIT) - KIT-Bibliothek. Karlsruhe, KIT, Diss., 2013.

Stephan, C., Alpers, M., Millet, B., Ehret, G., Flamant, P., and Deniel, C. (2011). Merlin: a space-based methane monitor. *Proc. SPIE*, 8159:815908–815908–15.

- Stocker, T. F., Dahe, Q., and Plattner, G.-K. (2013). Climate change 2013: The physical science basis. *Contribution of Working Group I Contribution to the Fifth Assessment Report of the Intergovernmental Panel on Climate Change*.
- Takahashi, T., Sutherland, S. C., Wanninkhof, R., Sweeney, C., Feely, R. A., Chipman, D. W., Hales, B., Friederich, G., Chavez, F., Sabine, C., Watson, A., Bakker, D. C., Schuster, U., Metzl, N., Yoshikawa-Inoue, H., Ishii, M., Midorikawa, T., Nojiri, Y., Körtzinger, A., Steinhoff, T., Hoppema, M., Olafsson, J., Arnarson, T. S., Tilbrook, B., Johannessen, T., Olsen, A., Bellerby, R., Wong, C., Delille, B., Bates, N., and de Baar, H. J. (2009). Climatological mean and decadal change in surface ocean pCO₂, and net sea-air {CO₂} flux over the global oceans. *Deep Sea Research Part II: Topical Studies in Oceanography*, 56(8–10):554 – 577. Surface Ocean {CO₂} Variability and Vulnerabilities.
- TCCON-Wiki (2015). Tccon-wiki. *Online: <https://tccon-wiki.caltech.edu/>*.
- Turnbull, J., Guenther, D., Karion, A., Sweeney, C., Anderson, E., Andrews, A., Kofler, J., Miles, N., Newberger, T., Richardson, S., and Tans, P. (2012). An integrated flask sample collection system for greenhouse gas measurements. *Atmospheric Measurement Techniques*, 5(9):2321–2327.
- van Amerongen, A. H., Visser, H., Vink, R. J. P., Coppens, T., and Hoogeveen, R. W. M. (2010). Development of immersed diffraction grating for the tropomi-swir spectrometer. *Proc. SPIE*, 7826:78261D–78261D–8.
- van der Laan, S., Neubert, R. E. M., and Meijer, H. A. J. (2009). A single gas chromatograph for accurate atmospheric mixing ratio measurements of CO₂, CH₄, N₂O, SF₆ and CO. *Atmospheric Measurement Techniques*, 2(2):549–559.
- Volz, F. E. (1974). Economical multispectral sun photometer for measurements of aerosol extinction from 0.44 μm to 1.6 μm and precipitable water. *Appl. Opt.*, 13(8):1732–1733.
- Vondrák, J. and Richter, B. (2004). International earth rotation and reference systems service (iers) web: www.iers.org. *Journal of Geodesy*, 77(10-11):585–678.
- Washenfelder, R. A., Toon, G. C., Blavier, J.-F., Yang, Z., Allen, N. T., Wennberg, P. O., Vay, S. A., Matross, D. M., and Daube, B. C. (2006). Carbon dioxide column abundances at the wisconsin tall tower site. *Journal of Geophysical Research: Atmospheres*, 111(D22):n/a–n/a. D22305.
- Widenhorn, R., Blouke, M. M., Weber, A., Rest, A., and Bodegom, E. (2002). Temperature dependence of dark current in a ccd. In *Electronic Imaging 2002*, pages 193–201. International Society for Optics and Photonics.
- WMO-GAW (2011). Wmo-gaw: Report of the 15th wmo/iaea meeting of experts on carbon dioxide, other greenhouse gases, and related tracers measurement techniques.

- Wofsy, S. C. (2011). Hiaper pole-to-pole observations (hippo): fine-grained, global-scale measurements of climatically important atmospheric gases and aerosols. *Philosophical Transactions of the Royal Society of London A: Mathematical, Physical and Engineering Sciences*, 369(1943):2073–2086.
- Wunch, D., Toon, G., Blavier, J., Waschenfelder, R., Notholt, J., Connor, B., Griffith, D., and Sherlock, V. (2011). The total carbon column observing network. *Phil. Trans. R. Soc., A* (2011) 369:2087–2112.
- Wunch, D., Toon, G. C., Wennberg, P. O., Wofsy, S. C., Stephens, B. B., Fischer, M. L., Uchino, O., Abshire, J. B., Bernath, P., Biraud, S. C., Blavier, J.-F. L., Boone, C., Bowman, K. P., Browell, E. V., Campos, T., Connor, B. J., Daube, B. C., Deutscher, N. M., Diao, M., Elkins, J. W., Gerbig, C., Gottlieb, E., Griffith, D. W. T., Hurst, D. F., Jiménez, R., Keppel-Aleks, G., Kort, E. A., Macatangay, R., Machida, T., Matsueda, H., Moore, F., Morino, I., Park, S., Robinson, J., Roehl, C. M., Sawa, Y., Sherlock, V., Sweeney, C., Tanaka, T., and Zondlo, M. A. (2010). Calibration of the total carbon column observing network using aircraft profile data. *Atmospheric Measurement Techniques*, 3(5):1351–1362.
- Yokota, T., Oguma, H., Morino, I., and Inoue, G. (2004). A nadir looking "swir" sensor to monitor co₂ column density for japanese "gosat" project. In *Twenty-Fourth International Symposium on Space Technology and Science*, pages 887–889.
- Zhao, C. L. and Tans, P. P. (2006). Estimating uncertainty of the wmo mole fraction scale for carbon dioxide in air. *Journal of Geophysical Research: Atmospheres*, 111(D8):n/a–n/a. D08S09.
- Zwinkels, J. C. and Gignac, D. S. (1991). Automated high precision variable aperture for spectrophotometer linearity testing. *Appl. Opt.*, 30(13):1678–1687.

Diese Seite ist den meist ehrenamtlichen Entwicklern gewidmet, die freie Software wie L^AT_EX, Gimp, Inkscape, Python und viele andere entwickeln, verbessern und kostenfrei zur Verfügung stellen.

